Tailoring femtosecond laser filamentation in the atmosphere

Silin Fu

INSTITUT POLYTECHNIQUE DE PARIS

ENSTA

IP PARIS

NNT : 2024IPPAE017

Thèse de doctorat

Tailoring femtosecond laser filamentation in the atmosphere

Thèse de doctorat de l'Institut Polytechnique de Paris
Préparée à l'École nationale supérieure de techniques avancées

École doctorale n°626, École doctorale de l'Institut Polytechnique de Paris (ED IP Paris)
Spécialité de doctorat : Optique, laser et plasma

Thèse présentée et soutenue à Palaiseau, le 25/09/2024, par

SILIN FU

Composition du Jury :

Jérôme Faure Directeur de recherche, LOA, CNRS, France	Président
Tiejun Wang Professeur, SIOM, Chinese Academy of Science, China	Rapporteur
Francois Courvoisier Directeur de recherche, FEMTO-ST, CNRS, France	Rapporteur
Pengji Ding Professeur, Lanzhou University, China	Examinateur
Aurélien Houard Chercheur, LOA, École polytechnique, France	Directeur de thèse
André Mysyrowicz Professeur émérite, LOA, France	Invité

Acknowledgments:

I can still vividly recall the nervousness I felt three and a half years ago at Beijing Capital International Airport. It was during the height of the pandemic, with the Delta variant raging and flights between China and France becoming extremely scarce. It felt as though once I left China, there would be no turning back. Now, three and a half years later, having gained invaluable friendships, countless wonderful memories, and a doctoral degree, I am truly grateful to my brave self from back then.

During my three and a half years of doctoral studies, I would first like to express my heartfelt gratitude to my supervisor, Dr. **Aurélien Houard**. Over this period, you dedicated an incredible amount of time to my doctoral thesis. Although we occasionally had disagreements, I feel very lucky to have chosen you as my supervisor. You supported me in purchasing expensive optical components to try out our ideas; when I encountered difficulties in my experiments, you came to the lab to help me resolve them. Your office seemed always open to me, allowing me to drop in anytime to discuss or share interesting and puzzling results. You guided me step by step in writing papers, conducting experiments, and analyzing data. I still remember the time when you were attending a conference in Japan, yet stayed up late to video call me and help me fix the laser system. I am deeply grateful for your professionalism, kindness, and patience.

I would also like to extend my gratitude to Prof. **André Mysyrowicz**. Thank you for always treating me with care and patience, promptly revising my manuscripts, sharing interesting stories over lunch, and offering invaluable advice. Most importantly, you constantly encouraged me. Even when I achieved only modest results, you would express great excitement and tell me that I had done a good job. Please know that such encouragement means a lot to a PhD student navigating the challenging journey of academia.

I would like to thank our lovely team, FILM. First, I am grateful to **Leonid Arantchouk** for his help in using his amazing high-voltage equipment, which allowed me to test the possibilities of guiding discharges. I also thank **Magali Lozano** for always making sure the laser was ready before I arrived at the lab and for staying late, sometimes until 7 p.m., to accompany me during high-voltage experiments. I want to thank **Fatima Alahyane** for the great programs she wrote, which made my experiments much easier, and for her constant enthusiasm, kindness, and willingness to help whenever I needed it. My gratitude also goes to former FILM team members, **Wonseok Lee** and **Benoit Mahieu**.

During my PhD, my three collaborators also made significant contributions to my work. Prof. **Arnaud Couairon** tirelessly helped me simulate countless cases of filament propagation and the corresponding hydrodynamic effects. Prof. **Vladimir Tikhonchuk** provided theoretical explanations for the THz part of my thesis. Lastly, Prof. **Yi Liu** supported me even before I joined LOA, inviting me to his lab in Shanghai to gain experimental experience. Both he and Arnaud, as members of my mini-defense committee, gave me valuable suggestions after my presentation.

I also want to thank all **the friendly colleagues at LOA**, especially the always-helpful **secretaries** who made my lab life easier with their warm support.

Far from home, my friends played an essential role in helping me complete my PhD.

First, I would like to thank my friends and colleagues **Baptiste Groussin**, **Nicolas Cantonnet-Paloque**, and **Juliette Billing**. Baptiste is the most amazing and smartest master's student I have ever met. Even though his internship only lasted six months, we conducted many interesting and crazy experiments together. His energy and motivation were endless, and I will never forget the joyful conversations we shared over lunch, coffee, or drinks in Palaiseau's bars. I wish him a wonderful PhD

life in the UPX group, and I am sure he will succeed! Nicolas, thank you for bringing so much laughter to the final stage of my PhD journey and for the adorable birthday gift (the best ham in the world!). I truly appreciate your sincerity and cheerful personality. But I will keep those hilarious videos of you from the nightclubs in Tianjin and Beijing as compensation for breaking my iris on your very first day in the lab. As for Juliette, I will always treasure the wonderful times we shared in the cafeteria, the lab, and the restaurants in Palaiseau.

To my 'lunch buddies' from IMSIA—**Xinyuan Zhai**, **Chengguan Zhang**, **Shuaichen Guo**, and **Xiaofei Ju**—thank you for making lunch breaks so enjoyable. A special thank you to Chengguan for driving us to lunch, saving me a lot of time, and to Xinyuan and his girlfriend, **Qiqi Tao**, for inviting me to their home to relax with their cats and celebrate Chinese New Year. I am truly grateful for the joyful moments we shared, exploring various restaurants and bars in Paris (thanks, Xinyuan, for not forcing me to eat at your favorite Pho 14).

To my “PhD friends”, **Yang Ye**, **Shenming Wang**, **Lihao Guan**, **Heng Zhang**, **Zheyi Yang**, **Xiang Zhang**, and **Yihan Xiong**, thank you for exploring nearly every Chinese restaurant in Paris with me. Special thanks to Xiang Zhang for being a part of my PhD life for a year and a half and for staying late in the lab with me until 9 p.m.

As an essential part of my PhD journey, the friends in my "family group" brought me countless moments of companionship and relaxation. They include **Yutao Tang**, **Bicong Wu**, **Baotao Li**, **Chenyun Ye**, **Huan Wu**, **Mengjie Zhang**, **Wei Zhang**, **Luyun Chen**, and many others. First and foremost, I must express my gratitude to Huan Wu. If it weren't for meeting her, I would never have encountered so many interesting people. I will always cherish the memories of our times in Paris—the laughter we shared in bars, clubs, restaurants, parks, and forests, as well as the footprints we left on the beaches of Brittany, and the tumbles we shared on the snowy slopes of Val Thorens.

In addition, I am thankful to my good friend **Zhehao Chen** in Finland for our travels across much of Europe, creating countless fond memories. I also want to thank my friend **Xu Liu** from CEA, who not only taught me fitness and swimming but was also a source of comfort during my anxious moments, often inviting me to enjoy delicious home-cooked meals. Thanks to my friends **Haoran Xu** and **Zhengjun Shi** from Lanzhou University for their companionship in the final months of my PhD, making those last months joyful. I would also like to thank my friends **Junlong Zhang** and **Shenzhuo Wang**, whom I met through hosting events. I am truly grateful for the time we spent together, whether visiting exhibitions, attending the concert to support Junlong’s girlfriend, or simply enjoying each other’s company during our wonderful moments.

There are many more friends whose names I cannot list here due to space constraints, but know that my life in Paris was made vibrant and colorful because of your presence.

Lastly, I would like to express my gratitude to **my family** for their financial support, which allowed me to fully focus on and enjoy my PhD life without any financial stress.

Résumé

La filamentation laser femtoseconde est un phénomène unique résultant de la propagation d'impulsions laser ultracourtes et de forte puissance dans un milieu nonlinéaire. Son mécanisme fondamental repose sur un équilibre complexe entre l'effet Kerr et la défocalisation causée par la création de plasma. La formation de filaments permet à une impulsion laser de maintenir une intensité élevée et un faisceau de petite taille sur de grandes distances, bien au-delà de la longueur de Rayleigh. Grâce à cette propriété, la filamentation est devenue un sujet de recherche clé en physique des lasers intenses et trouve des applications prometteuses dans des domaines variés tels que les sciences atmosphériques et la photonique.

Mécanismes physiques de la filamentation

Lorsqu'une impulsion laser ultracourte (typiquement de durée femtoseconde) se propage dans un milieu, et si sa puissance dépasse le seuil d'auto-focalisation (de l'ordre de quelques gigawatts dans l'air), l'effet Kerr non linéaire modifie l'indice de réfraction du milieu, ce qui provoque une auto-focalisation du faisceau. L'indice de réfraction est donné par la relation $n = n_0 + n_2 I$, où n_0 est l'indice linéaire, n_2 l'indice nonlinéaire, et I l'intensité du laser. À des intensités élevées, l'augmentation de $n_2 I$ amplifie la focalisation du faisceau.

Cependant, lorsque l'intensité du faisceau atteint un certain seuil, elle devient suffisante pour ioniser le milieu à travers des processus d'ionisation multiphotonique et collisionnelle, générant alors un plasma dans lequel 0,1% des molécules d'air est ionisé. Ce plasma induit un effet de défocalisation qui contrecarre l'auto-focalisation Kerr. La compétition dynamique entre ces deux effets aboutit à la formation d'un filament plasma stable, avec un diamètre typique de 100 µm et une intensité laser limitée à $10^{13} - 10^{14}$ W/cm^2. Ces caractéristiques permettent une propagation stable du faisceau filamenté dans les milieux transparents sur des distances de plusieurs centaines de mètres, voire des kilomètres.

Applications des filaments

En raison de leurs propriétés uniques, les filaments laser trouvent des applications dans de nombreux domaines.

- Laser-Induced Breakdown Spectroscopy (LIBS) : Les filaments laser permettent de générer une intensité laser élevée sur de longues distances, ce qui est idéal pour la spectroscopie induite par claquage optique à distance.
- Compression d'impulsions laser femtoseconde : Les filaments induisent un élargissement spectral et une auto-compression des impulsions en raison de l'effet Kerr, facilitant la génération d'impulsions ultracourtes de quelques cycles optiques.
- Rayonnements secondaires : Les canaux de plasma générés par filamentation produisent des rayonnements secondaires tels que l'effet de lasage UV des molécules d'azote de l'air (air lasing) ou l'émission d'impulsions térahertz (THz) large bande. Ces dernières sont particulièrement adaptées à la détection et à la télémétrie à distance.
- Guidage de la foudre et des décharges électriques : Les filaments créent des canaux d'air ionisé à faible densité, abaissant les seuils de claquage électrique et permettant de guider des décharges électriques ou même la foudre.
- Création de guides d'ondes dans l'atmosphère : Les variations de densité d'air provoquées par les

filaments peuvent former des structures similaires à des fibres optiques dans l'atmosphère, idéales pour transporter des signaux optiques ou LIBS.
- Réduction de la traînée d'engins supersoniques : Les canaux d'air chaud générés par les filaments peuvent réduire la trainée de véhicules supersoniques lorsqu'on sont générés en amont de l'onde de choc, améliorant leur efficacité énergétique.

Structure de la thèse

Cette thèse explore la modulation spatiale ou temporelle de faisceau de filaments laser femtoseconde générés dans l'air et leur optimisation pour des applications atmosphériques.

- Première partie : Introduction
  Nous introduisons les principes et modèles théoriques de la formation des filaments ainsi que les méthodes utilisées pour caractériser les filaments dans cette étude. Nous passons également en revue les techniques actuelles permettant de contrôler les filaments.

- Deuxième partie : Étude des filaments produits par des faisceaux de Laguerre-Gauss
  Nous étudions en détail la génération de filaments à l'aide de faisceaux Laguerre-Gauss. Cette section inclut des mesures de la puissance critique d'auto-focalisation et de l'énergie déposée dans les filaments dans différentes conditions. Nous établissons des expressions analytiques pour la puissance critique en fonction de la durée d'impulsion et analysons l'impact de l'ouverture numérique du faisceau, un facteur souvent négligé dans les études précédentes.

- Troisième partie : Organisation transverse des filaments et génération de guides d'ondes dans l'air
  Nous démontrons comment des faisceaux Laguerre-Gauss, notamment les faisceaux vortex, permettent de structurer les faisceaux de filaments pour former des guides d'ondes aériens. À faible cadence laser, nous montrons pour la première fois en laboratoire qu'un faisceau vortex peut générer un guide d'ondes. En combinant des faisceaux vortex avec une lame de phase multifocale, nous étendons significativement la longueur de ces guides d'ondes. Enfin, à l'aide d'effets cumulatifs à une cadence laser de 1 kHz, nous créons un guide d'ondes permanent atteignant une longueur de plusieurs dizaines de mètres.

- Quatrième partie : Organisation longitudinale des filaments
  En utilisant des faisceaux laser avec des modes de Laguerre-Gauss, nous augmentons considérablement la longueur des filaments et la distance des décharges guidées par rapport aux faisceaux gaussiens classiques. De plus, l'introduction de lames de phase multifocale permet de générer des superfilaments étendus, doublant la longueur des décharges guidées par laser.

- Cinquième partie : Filaments contrôlés spatio-temporellement
  Nous exploitons la technique du « flying focus » pour générer des filaments dont la vitesse et la direction de propagation du front d'ionisation sont réglables. Lorsque la vitesse du front d'ionisation dépasse celle de la lumière, ces filaments produisent un rayonnement térahertz de type Cherenkov, augmentant ainsi l'intensité du rayonnement THz d'un ordre de grandeur.

Conclusion

Cette thèse met en lumière le potentiel des filaments laser femtoseconde pour des applications atmosphériques avancées, tout en introduisant des stratégies innovantes pour leur contrôle spatio-temporel. Ces résultats ouvrent la voie à de nouvelles applications dans les domaines de l'optique, de la photonique et des sciences de l'atmosphère.

Contents

Preface

When a femtosecond laser pulse propagates in a nonlinear medium with a power exceeding the self-focusing threshold, a long plasma filament is formed. This allows the femtosecond pulse to propagate distances far greater than the Rayleigh length while maintaining a small beam waist and a high intensity in any transparent media, including air. By optimizing the laser parameters, filamentation has been achieved up to kilometric distances. These filaments have many applications, especially in the atmosphere. They can guide lightning, create waveguide structures in the air for optical signals, reduce the drag in supersonic flight, guide terahertz and microwave radiation, and serve as sources of air lasing and terahertz radiation for remote sensing.

This thesis deals with the spatio-temporal tailoring of femtosecond laser filaments in air, and their optimization for atmospheric applications.

In the first part, we detail the principles and theoretical models of filament generation and the methods used to characterize filaments in this work.

In the second part, we present a detailed study on the generation of filaments with Laguerre-Gaussian beams, including measurements of the critical power for self-focusing and of the deposited energy in filaments under different conditions.

The third part discusses the organization of filaments along the transverse section of the beam, using vortex and other Laguerre-Gaussian beams for the realization of optical air waveguides. We first demonstrate that vortex beams are a simple method to create air waveguides. Then, by combining vortex beams with multifocal phase plates, we significantly extend the length of these air waveguides. Finally, utilizing the cumulative effect produced by the filaments at a kHz repetition rate, we generate a permanent air waveguide up to several tens of meters long.

In the fourth part, we discuss the organization and extension of filaments along the propagation axis of the beam. Using Laguerre-Gaussian beams, we significantly extend the filament length and successfully increase the guided discharge distance compared to a classical gaussian beam. Additionally, by using multifocal phase plates to generates three foci along the laser axis, we produce extended superfilaments, doubling the length of laser guided discharges.

In the fifth part, we discuss the generation of spatio-temporally controlled light filaments, using a flying focus technique. We demonstrate the formation of an ionization front with adjustable speed and direction. The later can generate a pure Cherenkov terahertz radiation when the ionization front velocity is superluminal, thus increasing the terahertz radiation produced by monochromatic light filaments in air by an order of magnitude.

Chapter 1

Plasma Filaments Generated by Ultrafast Lasers in Air

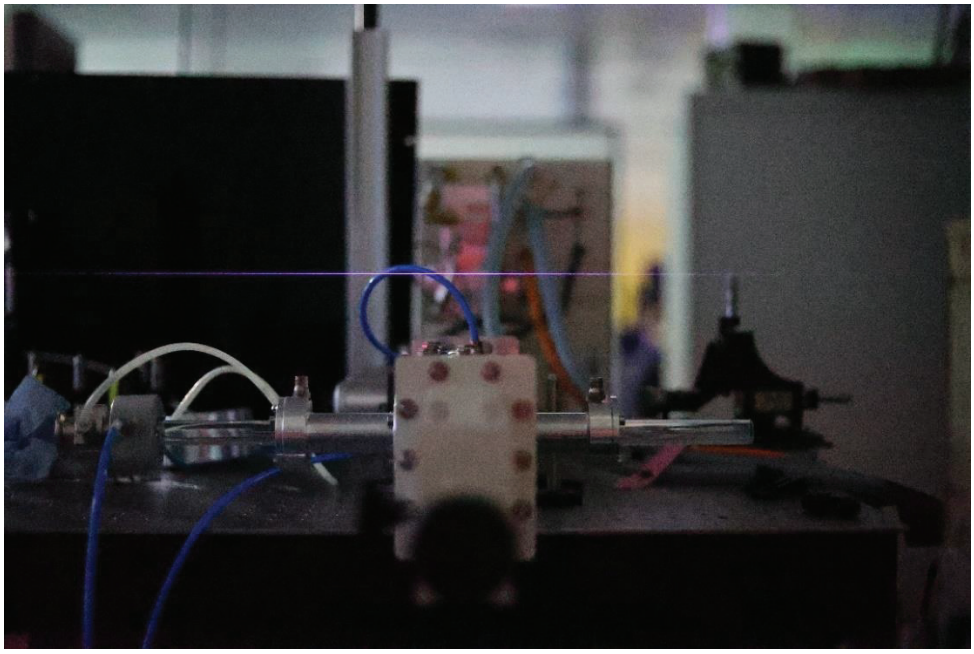

Figure 1.1. Image of a filament generated in laboratory: plasma luminescence is recorded using a commercial camera.

In this chapter, I will start by presenting a brief history of laser development. I will then explain the various linear and nonlinear effects involved in the laser filamentation process, and describe the theory of nonlinear pulse propagation used to simulate the generation of filaments. I will also provide the general characteristics of filaments, including their initiation and termination, the plasma density and the different timescales related to the evolution of filaments. Finally, I will introduce various atmospheric applications of filamentation to help the readers to understand the content of the subsequent chapters.

1.1 Introduction to filament generation

1.1.1 The development of laser technology

Since Albert Einstein proposed the concept of Light Amplification by Stimulated Emission of Radiation (LASER) in 1917 [1], laser technology has undergone a century of development. During this period, the evolution of laser technology has primarily focused on two directions: higher power density and shorter pulse duration.

- **Increasing power density**

In 1960, Theodore Maiman achieved the first laser emission in a ruby crystal, marking the birth of laser technology [2]. In 1962, Arthur Schawlow and Charles Townes proposed the Q-switching technique, which introduces a modulating element within the laser cavity to temporarily lower the quality factor (Q factor) of the cavity, allowing more energy to accumulate. When the Q factor is restored, the accumulated energy is released in a short burst, generating a high peak-power laser pulse [3]. Q-switching technology has found widespread applications in material processing, laser ranging, and medical treatments [4].

In the 1970s, laser technology further advanced with the development of dye lasers and excimer lasers. These lasers offered higher power densities and shorter pulse durations, expanding the range of laser applications. For instance, excimer lasers are widely used in ophthalmic surgery for precise corneal ablation.

Entering the 21st century, high-power lasers became a research hotspot in defense and energy sectors. Around 2000, the National Ignition Facility (NIF) in the United States was constructed, becoming the world's largest laser installation. Its goal is to achieve controlled nuclear fusion through laser-induced fusion. NIF uses 192 laser beams to heat a target material to extremely high temperatures and pressures, initiating nuclear fusion reactions [5].

Simultaneously, the emergence of fiber lasers and disk lasers broadened the industrial applications of high-power lasers. Fiber lasers, known for their high beam quality and conversion efficiency, are extensively used in laser cutting, welding, and micromachining [6]. Disk lasers, with their compact structure and high-power output, have gradually become mainstream technology in high-power lasers [7].

- **Shortening pulse duration**

In terms of pulse duration, advancements in laser technology have been equally remarkable. From the initial millisecond pulse durations, scientists have progressively achieved microsecond, nanosecond, picosecond, and femtosecond pulses, even reaching attosecond pulses.

In 1964, Hargrove *et al.* first achieved actively mode-locked lasers by synchronizing the phases of multiple longitudinal modes within a laser cavity, generating a series of short pulses [8]. This technology laid the foundation for the development of picosecond and femtosecond lasers. Subsequently, passive mode-locking technology was also developed, using a saturable absorber within the laser cavity to allow self-formation of pulses. Passive mode-locking became the primary method for realizing ultrashort pulse lasers due to its simplicity and stability [9].

In 1985, Gérard Mourou and Donna Strickland proposed the Chirped Pulse Amplification (CPA) technique. CPA involves chirping the initial pulse to stretch its duration, thereby reducing the peak power and avoiding nonlinear effects and damage in the amplifiers. The stretched pulse is then amplified and subsequently compressed back to its original short duration through dispersion compensation, achieving high-energy, ultrashort laser pulses [10]. CPA significantly advanced femtosecond laser technology and was awarded the Nobel Prize in Physics in 2018.

By the late 1990s, femtosecond laser technology had matured, enabling scientists to generate laser pulses with durations of only tens of femtoseconds. This allowed them to study dynamic processes in molecules and atoms on extremely short time scales, ushering in a new era of ultrafast science. For example, femtosecond lasers have been used to investigate the dynamics of chemical reactions, revealing mechanisms of chemical bond formation and breakage [11].

In 2001, scientists generated attosecond laser pulses for the first time, marking the birth of attosecond science. Attosecond lasers have vast application prospects in physics, chemistry, and biology, such as studying the dynamics of electrons and revealing the microscopic mechanisms of chemical reactions [12].

In 2023, Pierre Agostini, Ferenc Krausz, and Anne L'Huillier were awarded the Nobel Prize in Physics for their pioneering work in the field of attosecond laser pulses. Their research allows us to observe electron movements on unprecedented time scales, providing new perspectives for understanding the behavior of matter at the fundamental level.

1.1.2 Filamentation of ultrashort femtosecond lasers in air

As the output power of lasers increased, researchers began to focus on the interactions between light and matter, which include many nonlinear effects. Phenomena such as laser frequency conversion, stimulated scattering, and self-action behaviors (e.g., self-focusing, self-phase modulation, and self-steepening) were successively demonstrated [13].

In an air environment, ultrashort femtosecond laser pulses are influenced by various linear and nonlinear effects during propagation, leading to the phenomenon of filamentation [14].

Filamentation, or plasma filament, appears when a femtosecond laser pulse propagates through a transparent medium with a peak power exceeding the self-focusing threshold. This phenomenon is called laser filamentation [13]. The filamentation effect allows the laser pulse to maintain a relatively small beam waist while propagating over distances far greater than the Rayleigh length. Moreover, the filament sustains a relatively high laser intensity and plasma density within it.

In 1995, A. Braun *et al.* were the first to observe the phenomenon of femtosecond laser filamentation in air. They used laser pulses of 50 mJ and 200 fs to create plasma filaments with diameters of 80 μm and lengths up to 20 meters in air [14]. Subsequently, by optimizing the conditions for filamentation, research found that femtosecond lasers could form plasma

filaments several hundred meters long in the atmosphere and control filamentation at distances of several kilometers [15, 16].

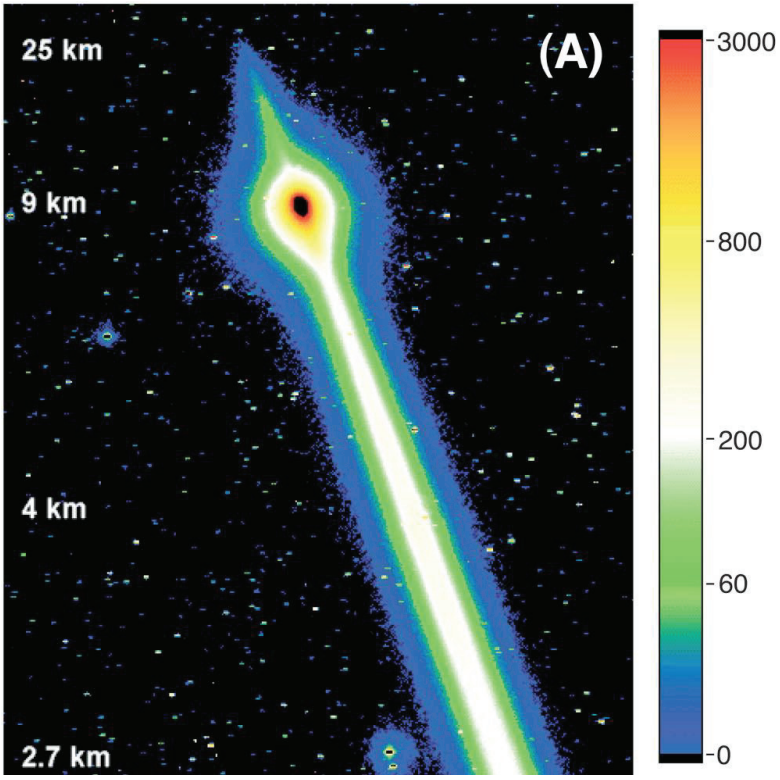

Figure 1.1.1. White light emission generated by filamentation diffracted by the clouds at long distance. From [15].

1.2 Principle of filament generation

In general, the physical process of filament generation can be simply described as a dynamic competition between diffraction and two nonlinear physical effects: Kerr self-focusing and plasma-induced defocusing.

1.2.1 Kerr self-focusing effect

Kerr self-focusing is a nonlinear optical phenomenon that occurs when the intensity of a laser beam is high enough to modify the refractive index of the medium in which it is propagating. This effect is named after John Kerr, who discovered that certain materials exhibit a refractive index that varies with the light intensity. The change in the refractive index is given by:

$$n = n_0 + n_2 I, \tag{1.2.1}$$

where n_0 is the linear refractive index, n_2 is the nonlinear refractive index coefficient, and I is the intensity of the light. In this context, the increase in the refractive index acts as a focusing lens, since the laser intensity is maximum on the center of the beam.

The starting point for the analysis of Kerr self-focusing is the nonlinear Schrödinger equation (NLSE), which describes the evolution of the electric field envelope E in a nonlinear medium:

$$i\frac{\partial E}{\partial z} + \frac{1}{2k}\nabla_{\perp}^2 E + \frac{\omega n_2}{c}|E|^2 E = 0, \tag{1.2.2}$$

where $k = \frac{2\pi n_0}{\lambda}$ is the wave number, $\nabla_{\perp}^2$ is the transverse Laplacian, ω is the angular frequency, c is the speed of light, n_2 is the nonlinear refractive index coefficient.

For a beam with a uniform intensity distribution, the nonlinear phase shift $\Delta\phi_{NL}$ over a propagation distance L is given by:

$$\Delta\phi_{NL} = \frac{\omega n_2 L I}{c}, \tag{1.2.3}$$

where $I = \frac{P}{A}$ and $A = \pi w^2$ is the cross-sectional area of the beam. Here, P represents the power of the laser beam.

The diffraction phase shift $\Delta\phi_{diff}$ over a distance L is approximately:

$$\Delta\phi_{diff} = \frac{L}{z_R}, \tag{1.2.4}$$

where z_R is the Rayleigh range:

$$z_R = \frac{\pi w^2}{\lambda}, \tag{1.2.5}$$

where w is beam waist.

When the nonlinear phase shift dominates, the beam experiences self-focusing due to the Kerr effect. The refractive index increases with intensity, causing the beam to focus more tightly. When diffraction dominates, the beam spreads out, opposing to the focusing effect.

To find the critical condition for self-focusing, one can set the nonlinear phase shift equal to the diffraction phase shift:

$$\frac{\omega n_2 L \frac{P}{\pi w^2}}{c} \approx \frac{L}{z_R}. \tag{1.2.6}$$

Substituting z_R:

$$\frac{\omega n_2 \frac{P}{\pi w^2}}{c} \approx \frac{\lambda}{\pi w^2}. \tag{1.2.7}$$

Solving for the critical power P_{cr}:

$$P_{cr} = \frac{c\lambda}{\omega n_2}. \tag{1.2.8}$$

Given $\omega = \frac{2\pi c}{\lambda}$:

$$P_{cr} = \frac{c\lambda}{2\pi c n_2/\lambda} = \frac{\lambda^2}{2\pi n_2}. \tag{1.2.9}$$

To generalize the expression for different beam profiles and configurations, we introduce the factor α:

$$P_{cr} = \alpha \frac{\lambda^2}{2\pi n_0 n_2}, \tag{1.2.10}$$

where α is an empirical factor that accounts for specific experimental conditions.

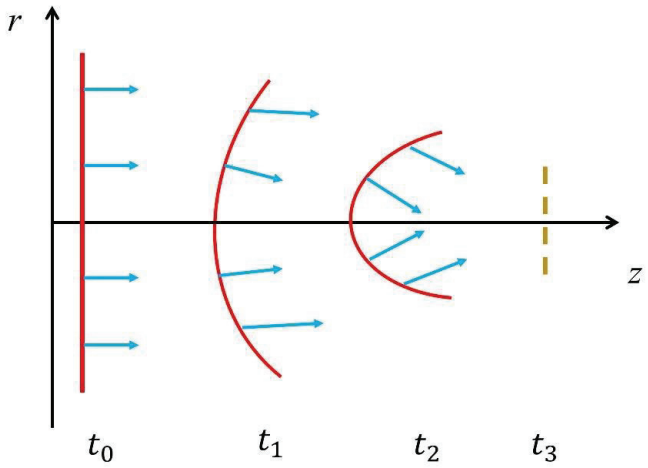

Figure 1.2.1. Evolution of the curvature of the laser wavefront under the influence of the Kerr effect.

When the laser power exceeds the critical power P_{cr}, the laser beam will overcome diffraction and continuously focus during propagation. In practical cases, the factor α should be adjusted to take into account the beam spatial profile. For Gaussian beams, the critical power P_{cr} is given by [13]:

$$P_{cr} = \frac{3.77\lambda_0^2}{8\pi n_2 n_0}. \tag{1.2.11}$$

At atmospheric pressure, the nonlinear Kerr refractive index n_2 in air is 3×10^{-19} cm^2/W for a laser at 800 nm [13]. Assuming the linear refractive index $n_0 = 1$ and the central wavelength $\lambda_0 = 800\ \mathrm{nm}$, the critical power for self-focusing is P_{cr} = 3.2 GW.

1.2.2 Plasma defocusing effect

When the laser power exceeds the critical power P_{cr}, the laser beam will overcome diffraction and self-focus as it propagates. During this process, the beam size decreases, and the power density increases significantly. This increased power density can become sufficient to ionize oxygen and nitrogen in air via multiphoton or tunneling ionization, forming a plasma. The formation of plasma leads to a reduction in the refractive index. According to electrodynamics, the refractive index n_p in a plasma can be expressed as:

$$n_p = \sqrt{n_0^2 - \frac{N_e e^2}{\epsilon_0 m_e \omega_0^2}}, \tag{1.2.11}$$

where N_e is the electron density in the plasma, e is the electron charge, ϵ_0 is the vacuum permittivity, m_e is the electron mass, and ω_0 is the central angular frequency of the femtosecond laser. The critical plasma density N_{crit} is defined as:

$$N_{crit} = \frac{\varepsilon_0 m_e \omega_0^2}{e^2}. \tag{1.2.12}$$

Typically, the plasma density in femtosecond laser-induced gas plasmas ranges from 10^{16} to 10^{17} cm^{-3}. Under these conditions, equation (1.2.11) can be approximated as:

$$n_p \approx n_0 - \frac{N_e}{2 n_0 N_{crit}}. \tag{1.2.13}$$

Thus, the refractive index of the gas medium can be expressed as:

$$n = n_0 + n_2 I - \frac{N_e}{2 n_0 N_{crit}}. \tag{1.2.14}$$

When the plasma forms, $n_2 I > \frac{N_e}{2 n_0 N_{crit}}$, the laser beam continues to focus, and the power density continues to increase, further ionizing the gas molecules. This results in an increase in the electron density of the plasma, which offsets the increase in the nonlinear refractive index due to the Kerr effect. Eventually, a balance is reached where:

$$n_2 I = \frac{N_e}{2 n_0 N_{crit}}. \tag{1.2.15}$$

This equilibrium does not exist in practice, because of the strong spatio-temporal effects that modify the pulse shape but it allows to estimate the intensity inside a filament [13].

1.3 Theoretical description of filamentation

In my thesis, we have simulated the formation of laser filaments with various input modes to compare with our measurements. This task has been carried out by our collaborator, Professor Arnaud Couairon from the Centre de Physique Théorique at École Polytechnique, with whom our group has been collaborating for nearly two decades. Here, I will briefly introduce the simulation methods we used. For detailed related theories, please refer to [18-20].

1.3.1 Nonlinear Schrödinger equation (NLSE)

To model the physics of filamentation of ultrashort laser pulses in transparent media, a basic model in the form of a nonlinear Schrödinger equation (NLSE) is used to describe the pulse propagation, taking into account various nonlinear effects. This model describes the propagation of the laser pulse through its electric field

$$\tilde{E}(x,y,z,t) = \frac{1}{2}E(x,y,z,t)\exp[i(kz-\omega_0 t)]\,\widehat{e_x} + c.c., \tag{1.3.1}$$

where z is the propagation direction, k and ω_0 are the wavenumber and the carrier angular frequency, respectively. The extended nonlinear Schrödinger equation (NLSE) can be expressed as [13]:

$$\mathcal{U}\frac{\partial\tilde{E}}{\partial z} = \frac{i}{2k}\left[\nabla_\perp^2 + \frac{n^2\omega^2}{c^2} - k^2\mathcal{U}^2\right]\tilde{E} + \mathcal{F}\{N(|E|^2,\rho)\}, \tag{1.3.2}$$

where $\tilde{E}(x,y,z,\omega)$ represents the Fourier transform of $E(x,y,z,t)$, $\nabla_\perp^2$ denotes the transverse Laplacian, $\mathcal{F}$ denotes the Fourier transform from the time to the frequency domain, and $\mathcal{U}$ is given by

$$\mathcal{U}(\omega) = 1 + \frac{\omega-\omega_0}{kv_g}, \tag{1.3.3}$$

where v_g is the group velocity.

The function N includes self-focusing, plasma defocusing, and photoionization effects and is given by

$$N(|E|^2,\rho) = T^2N_{\text{Kerr}}(|E|^2) + N_{\text{plasma}}(\rho) + TN_{\text{MPA}}(|E|^2), \tag{1.3.4}$$

where T accounts for space-time focusing and self-steepening of the pulse

$$T \equiv 1 + \frac{i}{\omega_0}\frac{\partial}{\partial t}. \tag{1.3.5}$$

The Kerr effect term $N_{\text{Kerr}}(|E|^2)$ results from the intensity-dependent refractive index and includes both instantaneous and retarded contributions

$$N_{\text{Kerr}}(|E|^2) = ik_0n_2\left[(1-f_R)|E(x,y,z,t)|^2 + f_R\int_{-\infty}^{t}R(t-t')|E(x,y,z,t')|^2dt'\right], \tag{1.3.6}$$

where n_2 is the nonlinear index of refraction, f_R is the fraction of the delayed contribution, and R represents the molecular response of the gas.

The plasma and multi-photon absorption (MPA) terms in the equation read, respectively

$$N_{\text{plasma}}(\rho) = -\frac{k_0}{2n_0\rho_c}\frac{\omega_0\tau_c\left(1+\omega^2\tau_c^2\right)}{1+i\omega\tau_c}\rho. \tag{1.3.7}$$

and

$$N_{\text{MPA}}(|E|^2) = -\frac{W(|E|^2)U_i}{2|E|^2}(\rho_{\text{at}} - \rho), \tag{1.3.8}$$

where τ_c is the electron collision time, ρ is the electron density in the plasma, ρ_c is the critical plasma density, U_i is the ionization potential, ρ_{at} is the density of neutral atoms, and W is the photoionization rate (including both multi-photon ionization (MPI) and tunnel ionization contributions).

The nonlinear Schrödinger equation, extended to include higher-order effects and non-instantaneous nonlinearities, provides a robust tool for modeling the intricate dynamics of laser filamentation. This theoretical framework allows for the exploration and optimization of filamentation-based applications in various scientific and technological fields.

1.4 Properties and applications of filaments in atmospheric environments

Filaments generated in the atmosphere have attracted significant attention from researchers over the past 30 years. These weakly ionized plasma filaments exhibit many unique properties, leading to various interesting applications.

1.4.1 Characteristics of filamentation in air

Before exploring the applications of filaments, we first focus on the properties of filaments generated in the atmosphere.

- **Initiation and termination of filamentation**

The distance from the point where femtosecond laser propagation begins to the point where self-focusing generates plasma can be calculated using the following equation [21, 22]:

$$z_f = \frac{0.367kw_0^2}{\sqrt{\left[\left(\frac{P}{P_{cr}}\right)^{1/2} - 0.852\right]^2 - 0.0219}}, \tag{1.4.1}$$

where k is the wavenumber, w_0 is the beam waist and P is the power of the femtosecond laser beam.

If we use a lens to generate the filaments, then the self-focusing distance z_f' is expressed as:

$$\frac{1}{z_f'} = \frac{1}{z_f} + \frac{1}{f}, \tag{1.4.2}$$

where f is the focal length of the lens.

By incorporating the focusing lens, the new position where the plasma forms (also called nonlinear focus) is adjusted close to the focal point of the lens.

As the laser pulse propagates, its intensity progressively diminishes due to effects like Rayleigh scattering, nonlinear absorption, or the spectral redistribution away from the initial wavelength. This energy depletion causes the filamentation process to cease when the pulse peak power falls below the critical power P_{cr}, indicating that Kerr self-focusing is no longer sufficient to counterbalance diffraction. Additionally, filamentation can stop even while the pulse power remains above the critical power, if the spatial phase curvature becomes excessively large due to plasma generation and defocusing [23].

- **Plasma density and lifetime**

The electron density and lifetime of the plasma in a filament are crucial parameters, directly impacting the propagation characteristics and the potential application of filaments in the atmosphere. The plasma density within a filament typically ranges from 10^{22} to $10^{23}\mathrm{m}^{-3}$. In 1995, Braun *et al.* first observed the formation of filaments by femtosecond lasers in air,

measuring a plasma density of approximately $10^{22}\mathrm{m}^{-3}$ [14]. Subsequent studies have shown that with increased laser pulse intensity and appropriate focusing, superfilaments can be generated, where the plasma density can be one to two orders of magnitude higher than that of regular filaments [19].

Measuring the lifetime of the plasma within a filament is challenging because the plasma recombination typically occurs on the nanosecond timescale. Tzortzakis *et al.* were the first to achieve direct measurement of the plasma lifetime using time-resolved diffractometry. They found that the initial electron density of the plasma was $10^{23}\ \mathrm{m}^{-3}$, with a decay process characterized by two phases: a rapid recombination phase followed by a slower electron attachment phase, with a characteristic lifetime of approximately 10 nanoseconds [24]. Electric conductivity measurements have confirmed this exponential decay behavior [4].

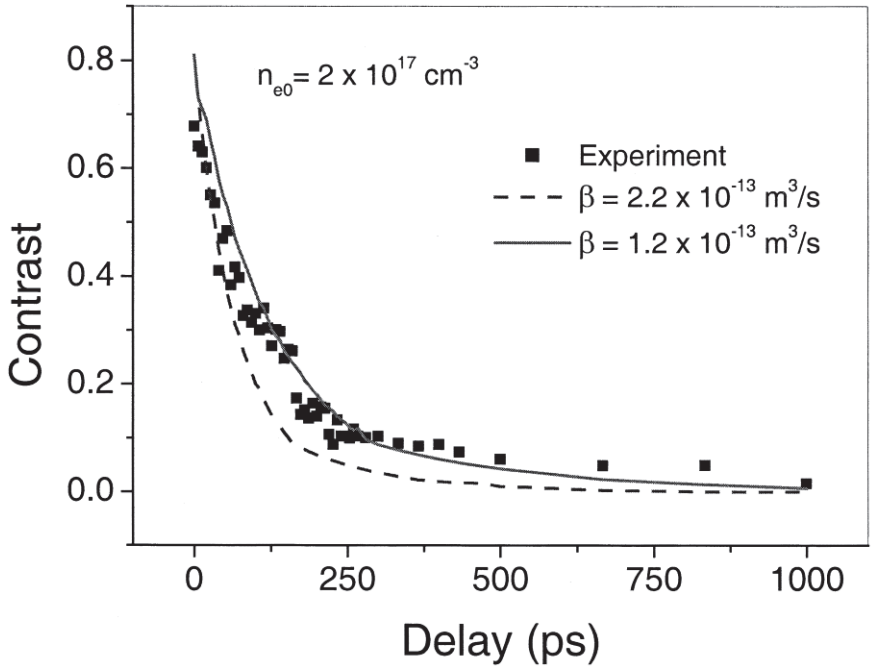

Figure 1.4.1 Measured time evolution of the filament plasma density. Black squares represent experimental data, while the lines show the results of simulations. From [24].

Further works using more precise interferometry techniques to characterize the plasma evolution have yielded similar results. For instance, Y.-H. Chen *et al.* demonstrated direct time- and space-resolved measurements of the electron density in plasma filaments induced by femtosecond laser pulses using an interferometer [26].

1.4.2 Applications of filaments in the atmosphere

My thesis focuses on optimizing the properties of femtosecond filaments in the atmosphere for several applications. In this subsection, we will briefly discuss some interesting atmospheric applications of filaments. I will introduce these applications from different timescales. As shown in Figure 1.4.2, I present the different effects of the filament on various timescales. On the femtosecond timescale, the interaction between light and matter produces a plasma. This plasma has a lifetime of a few nanoseconds. After the plasma disappears, the

release of energy from the plasma will cause heating of the gas and hydrodynamic effects on the microsecond to millisecond timescale.

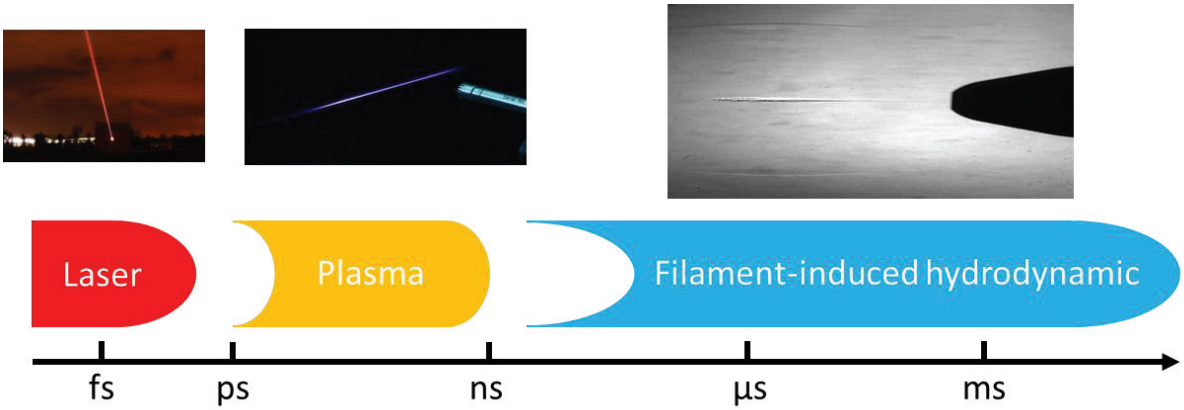

Figure 1.4.2. Comparison between the timescales of the different effects of the filament.

- **Laser**

Typically, we use femtosecond pulses to drive filamentation, and within the femtosecond time range, the interaction between the laser and the medium generates plasma filaments. During this interaction, it has been discovered that filaments can produce continuum generation that can be used for pulse compression. This is due to Kerr self-focusing, which causes spectral broadening of the pulse through self-phase modulation and self-steepening effects. Additionally, when ionization occurs, free electrons modify the refractive index. The electron density encountered by the tail of the pulse is significantly higher than that of the front, leading to blue-shifted frequencies at the tail of the pulse, similar to self-phase modulation [27]. Consequently, the initial spectrum of the pulse undergoes significant broadening after filamentation, ranging from near-ultraviolet to far-infrared. This spectral broadening effect, combined with the profound distortion experienced by the pulse during propagation, can be used for temporal compression if the frequency chirp is compensated. Using this technique, pulses have been compressed from 50 fs to a few fs through filamentation in argon [28]. This broad spectrum generated in the filament can also be used for multispectral LIDAR [45].

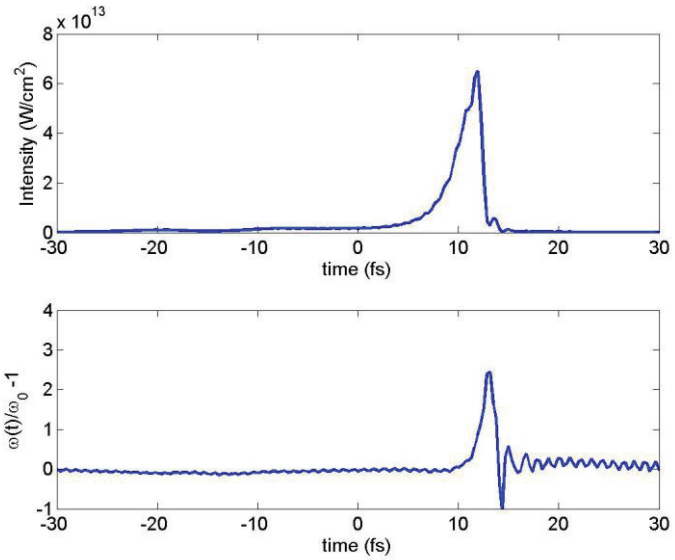

Figure 1.4.3. Pulse self-compressed using laser filamentation. Intensity distribution (top) and instantaneous frequency (bottom), cited from [28].

Filamentation also allow lasers to maintain very high intensities over long propagation distances, providing a new method for laser-induced breakdown spectroscopy (LIBS). The formation of femtosecond laser filaments ensures that the intensity within the filament remains at a relatively high and nearly constant level. This ensures a more uniform effect on the surface of the target during measurements. Additionally, due to the extended range of filamentation, this technique is suitable for long-distance detection. LIBS signals have even been detected at a distance of 1.9 km. Figure 1.4.4 presents an experimental schematic of LIBS induced by femtosecond filaments. As shown in Figure 1.4.4(b), LIBS signals were detected from a target located 50 meters away [29].

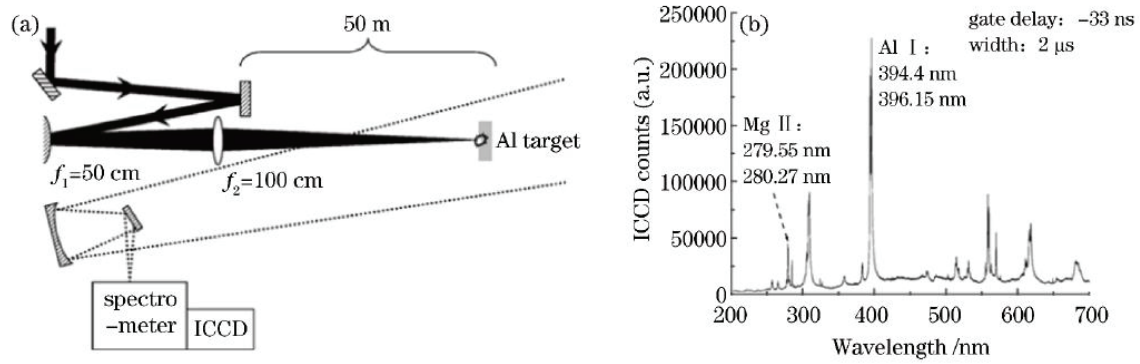

Figure 1.4.4. (a) Schematic diagram of the experimental setup used for filament induced LIBS (b) Spectrum measured at a distance of 50 meters.

- **Plasma**

After the laser field ionizes the air, the moving laser pulse leaves a plasma column in its wake. Free electrons are generated near the laser intensity peak and interact with the back of the pulse. They are pushed by the ponderomotive force causing a longitudinal oscillation of the plasma. The free electrons oscillate longitudinally in the plasma filament at the plasma

frequency $\omega_p = \left(\frac{4\pi e^2 N_e}{m_e}\right)^{1/2}$. The resulting electronic curent radiates a terahertz pulse since ω_p is close to 1 THz for a plasma density of 10^16 cm-3 [30]. The terahertz radiation produced by the filaments could be used for remote terahertz detection and imaging. This aspect will be discussed in detail in Chapter 5.

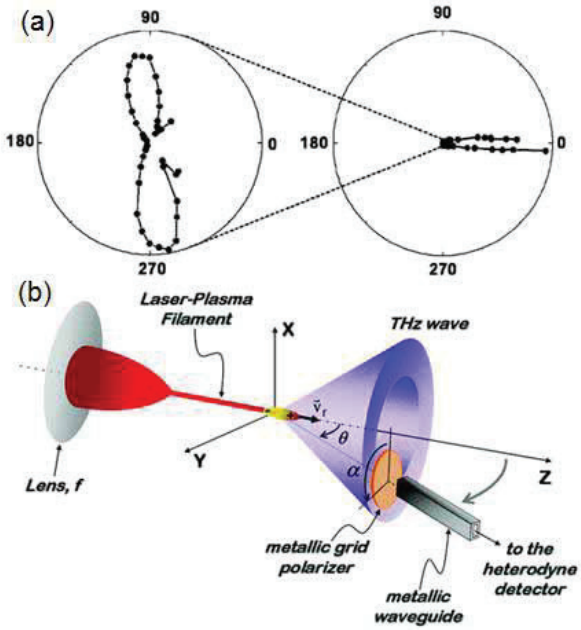

Figure 1.4.5. (a) Forward and radial terahertz radiation generated during the filamentation process. (b) Schematic diagram of the experimental setup for measuring terahertz radiation. Adapted from [31].

Another important secondary emission generated by plasma filaments is air lasing. In 2013, Yao *et al.* demonstrated that a probe pulse at 391 nm (or 428 nm) could be strongly amplified inside a plasma filament generated by a femtosecond laser pulse at 800 nm in pure nitrogen. This spectacular effect is known as the "lasing" effect of nitrogen molecular ions [32].

In addition to secondary emissions, plasma generated by filaments has been used for the guiding of microwave signals [33, 34] and to create plasma antennas [35], among other applications.

- **Filament-induced hydrodynamic**

After the plasma dissipates, the energy within the plasma is absorbed by the surrounding air in the form of heat, causing a significant increase in local temperature and air pressure. This generates an outward-propagating pressure wave, leaving a low-density air channel at the center (see Figure 1.4.2). These laser-induced hydrodynamic phenomena have many promising applications, such as remotely generating optical refractive index structures in the air to form air waveguides [36-38], which will be discussed in Chapter 3. Additionally, the low-density channel produced by filamentation plays a crucial role for the guiding of electric discharges with filaments, which will be the main focus of Chapter 4 of this thesis. This opens up broad prospects for the laser lightning rod concept [39] and many other applications.

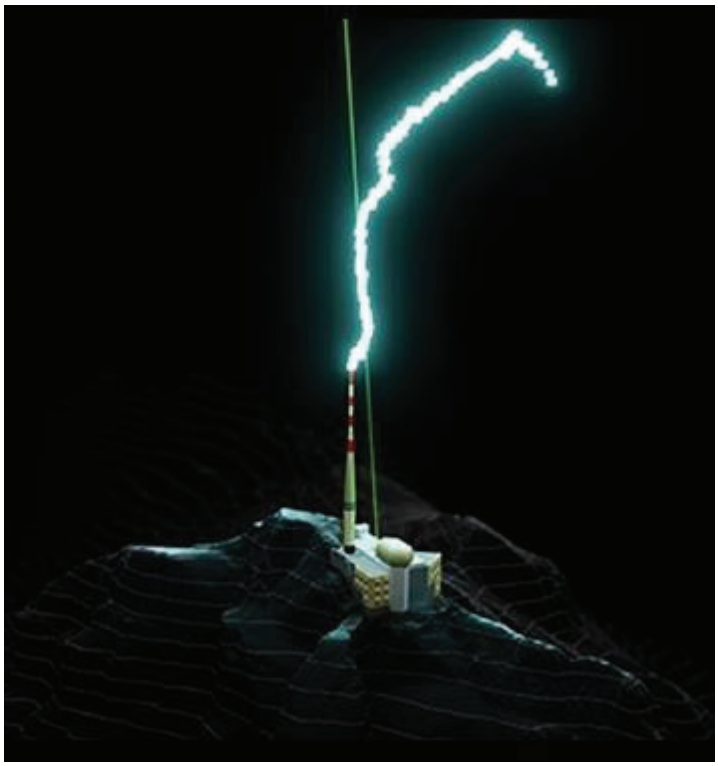

Figure 1.4.6. Illustration of a laser-guided lightning. From [39].

1.5 Methods to manipulate filamentation in air

Since the first experimental observation of femtosecond laser filamentation in air by A. Braun *et al.* in 1995 [14], numerous techniques have been developed to optimize filamentation for various applications. These techniques aim to control properties such as filament length, plasma density, plasma lifetime, and spatial distribution of the filaments.

Because my thesis work focuses primarily on the spatiotemporal manipulation of filamentation, this section will present some previously employed methods to control laser filamentation in air.

1.5.1 Adjusting incident laser parameters

Altering the incident laser parameters is the most common and straightforward method to control femtosecond laser filamentation. Generally, as the power of the incident laser beam increases, the length of the plasma filament increases correspondingly. In the case of superfilamentation, where the filament intensity can exceed the clamping intensity, increasing the input power can also increase the plasma density in the filament. However, with increasing laser power, various nonlinear effects also appear, such as the formation of multiple filaments. Due to the competition and fusion of these multiple filaments, the plasma density and length do not continue to increase indefinitely [19, 40].

In addition to power, the pulse duration significantly affects the nonlinear refractive index n_2, thereby influencing the critical power for self-focusing. This is due to the delayed Kerr effect that becomes significant for pulse duration longer than 100 fs. For instance, Liu *et al.* in 2005 measured the critical power for different incident pulse durations [41], as shown in Figure 1.5.1. It can be observed that with increasing pulse duration, the critical power decreases rapidly.

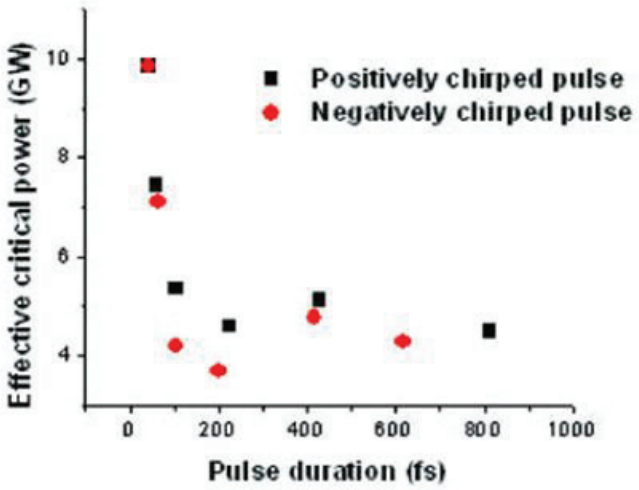

Figure 1.5.1. Critical power as a function of laser pulse duration measured by Liu *et al*., with black dots representing positively chirped pulses and red dots representing negatively chirped pulses (From [41]).

The wavelength of the incident pulse also affects the properties of the plasma. For example, shorter wavelengths result in a higher ionization rate, producing filaments with higher density but smaller diameter [42] as shown in Figure 1.5.2.

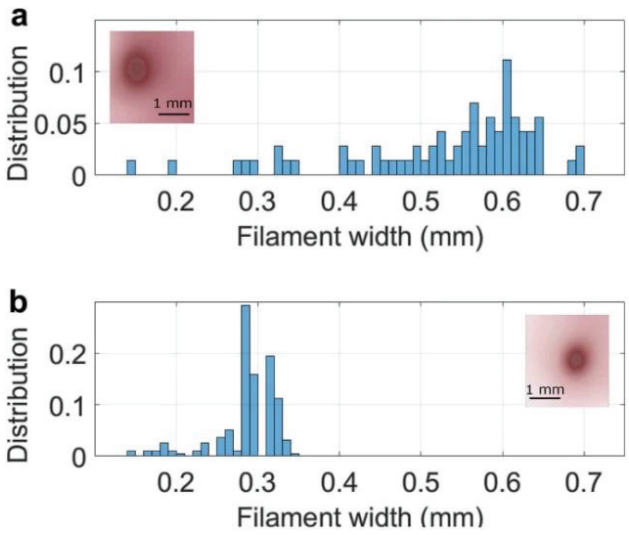

Figure 1.5.2. Diameter of filaments generated by beams of different wavelengths. (a) Filament produced by a laser at 1030 nm. (b) Filament produced after adding the second harmonic of the beam at 515 nm. The insets show direct imaging of the filaments using photosensitive paper, with the blackened, burned areas indicating the filaments. From [42].

Additionally, the repetition rate of the laser pulses can significantly alter the properties of the filaments. R. Löscher *et al.* observed that the length of the filaments increases with the laser repetition rate [43]. Yin *et al.* found that as the laser repetition rate increases, the plasma density produced by the filaments decreases [44], as shown in Figure 1.5.3.

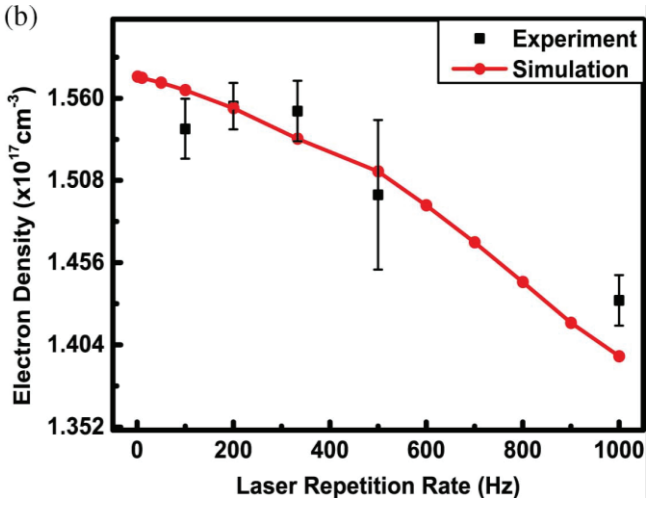

Figure 1.5.3. Plasma density at different laser repetition rates as measured by Yin *et al.* The red line represents the simulation results, and the black dots represent the experimental results. From [44].

What is even more intriguing is that by altering the mode of the incident laser beam, one can control the spatial distribution of light filaments. For instance, an Airy beam can create a plasma filament with a spatially curved profile [45]; employing a vortex beam (Laguerre-

Gaussian beams) can produce light filaments organized in a "doughnut" shape [46]; and utilizing a Bessel beam can generate a thin plasma column with a very uniform density distribution [47].

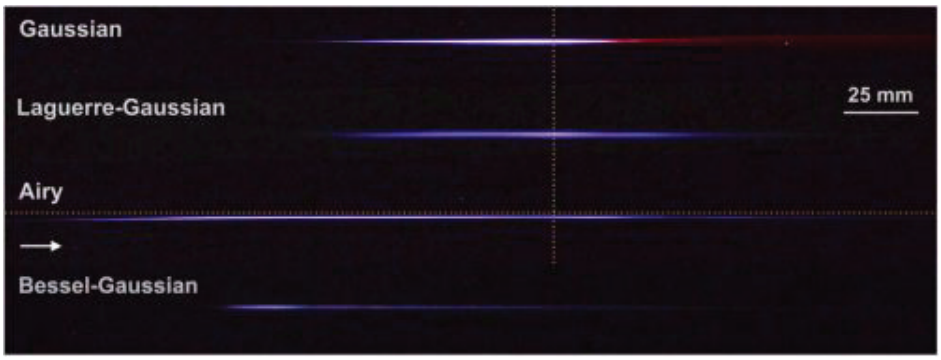

Figure 1.5.4. Various laser modes are used to generate light filaments in air. The filaments produced are recorded from above by a commercial camera, capturing the luminescence of the plasma. Taken from [48].

Due to spatial constraints in laboratory, people often use external focusing lenses to generate filaments. However, the plasma density of the filament strongly depends on the external focusing. For instance, F. Théberge *et al.* have shown that a smaller focal length f can produce a higher plasma density, with differences reaching up to four orders of magnitude, as shown in Figure 1.5.5. Additionally, the diameter of the filament also depends on the external focusing; as the external focusing length decreases, the diameter of the filament increases [49].

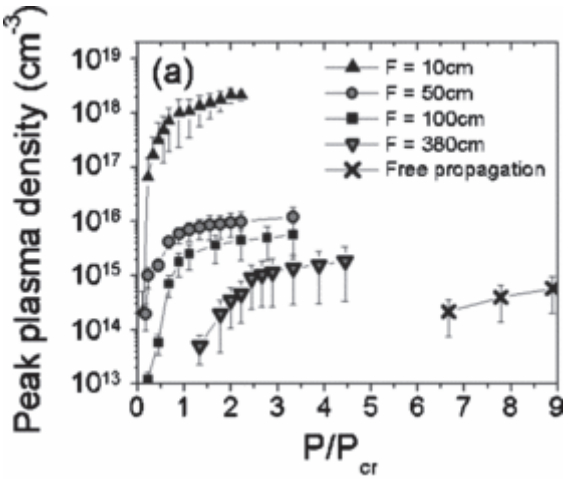

Figure 1.5.5. Measurement the peak plasma density of filaments as a function of the input peak power for different external focusing F ranging from F = 10 cm to free propagation [49].

In addition, other properties of the beam can also significantly change the characteristics of the filament, such as the polarization [50] and chirp [51] of the incident beam.

1.5.2 Background energy reservoir method

It has been observed that when a femtosecond laser pulse propagates as filaments in air, only about 10% of the total laser energy is concentrated in the ionizing core of the filament, while the remaining energy is distributed around this core, referred to as the "energy reservoir." To extend the length of the plasma filament, an external energy compensation method involves effectively transferring energy from the background energy reservoir to the central region of the filament [52], as illustrated in Figure 1.5.6.

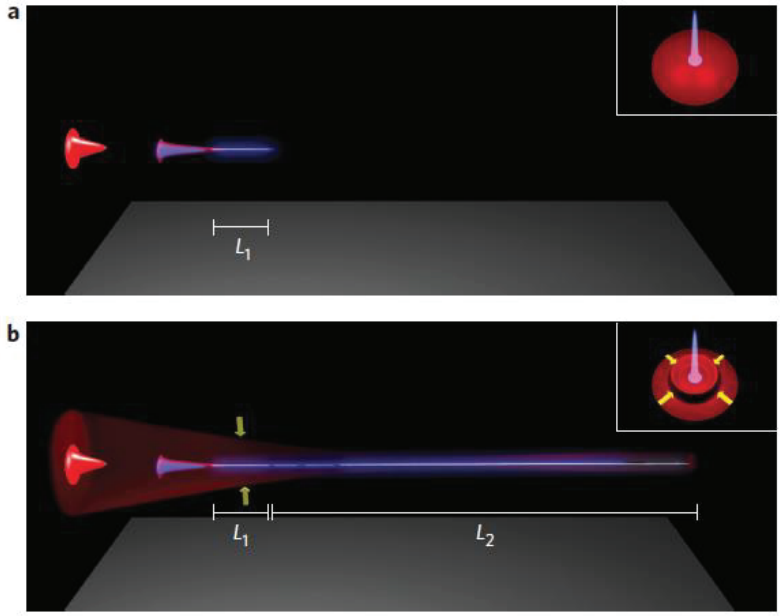

Figure 1.5.6. Schematic diagram of the background energy reservoir method for extending filaments. (a) A Gaussian beam focused by a lens forms a filament of length L_1; (b) Adding a convergent beam results in an extended filament. Taken from [52].

In general, the energy from the background energy reservoir does not spontaneously transfer to the central region of the filament; an additional axicon is required to achieve this effect. In 2014, Scheller *et al.* experimentally divided the initial incident laser into two beams: one beam was focused into a filament using a plano-convex lens, while the other beam, after passing through axicon lens, formed an annular beam that co-propagated collinearly with the first beam [52]. Their experimental results revealed that when the filament was accompanied by the assisting beam (the annular beam), the length of the plasma filament could be increased by at least an order of magnitude. They explained that the annular beam acts as an energy reservoir for the filament produced by the Gaussian beam, continuously supplying energy to the filament.

1.5.3 Multi-pulse technique

Regarding the lifetime of plasma, J. Papeer *et al.* demonstrated that co-propagating a long pulse laser beam (nanosecond beam) with the filament-forming short pulse beam can significantly extend the plasma lifetime [53]. Figure 1.5.7 shows the measurement and simulation results of plasma lifetimes when generating filaments with a short pulse alone, and

when simultaneously using a long pulse in conjunction with the short pulse. It is evident that the lifetime of these plasmas has been increased.

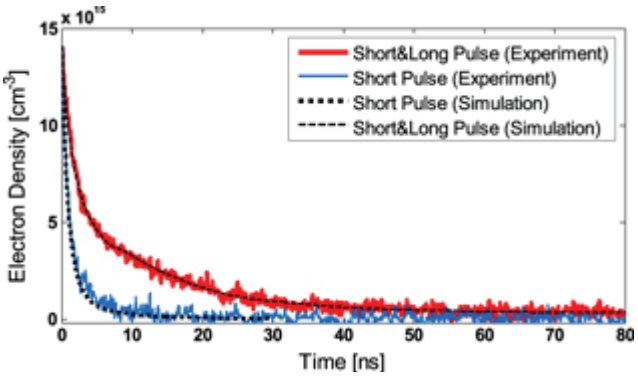

Figure 1.5.7. Measurement and simulation results of plasma lifetime in filaments extended by a long nanosecond pulse [53].

In addition to extending the lifetime of the plasma, multi-pulse techniques can also be used to focus separately different femtosecond pulses to generate a series of concatenated filaments, thereby extending the overall length of the filaments [54-57]. This will be discussed in detail in Chapter 3.

1.5.4 Other methods

In addition to the methods previously mentioned, several other techniques have been explored. These include generating diffractive gratings through filamented beam interference [58], creating plasma arrays using Dammann gratings [59], or extending the lifetime and length of plasma filaments using high-voltage electrical fields [60]. For example, in 2007, Zhu *et al.* measured the effect of a DC external electric field on a plasma filament. Compared to the case without an electric field, the length of the plasma filament was extended up to three times, and the lifetime of the plasma channel was significantly enhanced. The results are shown in Figure 1.5.8 [60].

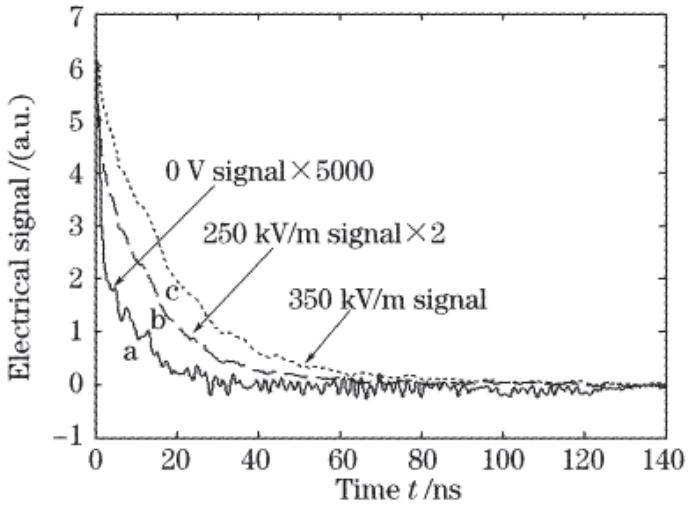

Figure 1.5.8. Plasma lifetime measured in the presence of different external electric fields [60].

References

1. A. Einstein. Zur Quantentheorie der Strahlung. Physikalische Zeitschrift. **18**, 121-128 (1917).
2. T. H. Maiman. Stimulated optical radiation in ruby. Nature **187**, 493-494 (1960).
3. A. Schawlow, C. H. Townes. Infrared and Optical Masers. Physical Review **112**, 1940-1949 (1958).
4. F. J. Mcclung, R. W. Hellwarth. Giant Optical Pulsations from Ruby. Applied Optics **33**, 103 105 (1962).
5. E. I. Moses. Ignition on the NIF: A path towards inertial fusion energy. Nuclear Fusion **49**, 104022 (2009).
6. D. J. Richardson, J. Nilsson, and W. A. Clarkson. High power fiber lasers: current status and future perspectives. J. Opt. Soc. Am. B **27**, B63-B92 (2010)
7. A. Giesen, H. Hügel, A. Voss, K. Wittig, U. Brauch and H. Opower. Scalable concept for diode-pumped high-power solid-state lasers. Applied Physics B **58**, 365-372 (1994).
8. L. E. Hargrove, R. L. Fork, M. A. Pollack. Locking of He-Ne laser modes induced by synchronous intracavity modulation. Applied Physics Letters **5**, 4-5 (1964).
9. U. Keller. Recent developments in compact ultrafast lasers. Nature **424**, 831-838 (1996).
10. D. Strickland, G. Mourou. Compression of amplified chirped optical pulses. Optics Communications **55**, 447-449 (1985).
11. A. H. Zewail. Femtochemistry: Atomic-scale dynamics of the chemical bond. J. Phys. Chem. A **104**, 5660–5694 (2000).
12. F. Krausz, M. Ivanov. Attosecond physics. Reviews of Modern Physics **81**, 163-234 (2009).
13. A. Couairon, A. Mysyrowicz. Femtosecond filamentation in transparent media. Phys.Rep. **441**, 47 (2007).
14. A. Braun, G. Korn, X. Liu, D. Du, J. Squier, G. Mourou. Self-channeling of high-peak-power femtosecond laser pulses in air. Optics Letters **20**, 73 (1995).
15. M. Rodriguez, R. Bourayou, G. Méjean, J. Kasparian, J. Yu, E. Salmon, A. Scholz, B. Stecklum, J. Eislöffel, U. Laux, A. P. Hatzes, R. Sauerbrey, L. Wöste, and J.-P. Wolf. Kilometer-range nonlinear propagation of femtosecond laser pulses. Phys. Rev. E **69**, 036607 (2004).
16. M. Durand, A. Houard, B. Prade, A. Mysyrowicz, A. Durécu, B. Moreau, D. Fleury, O. Vasseur, H. Borchert, K. Diener, R. Schmitt, F. Théberge, M. Chateauneuf, J.-F. Daigle and J. Dubois, Kilometer range filamentation. Opt. Express **21**, 26836 (2013).
17. M. D. Feit & J. A. Fleck. Effect of refraction on spot-size dependence of laser-induced breakdown. Appl. Phys. Lett. **24**, 169-172 (1974).
18. A. Couairon, E. Brambilla, T. Corti, D. Majus, O. de, J. Ramírez-Góngora and M. Kolesik. Practitioner's guide to laser pulse propagation models and simulation. Eur. Phys. J. Spec. Top. **199**, 5–76 (2011).
19. G. Point, Y. Brelet, A. Houard, V. Jukna, C. Milián, J. Carbonnel, Y. Liu, A. Couairon, and A. Mysyrowicz. Superfilamentation in Air. Phys. Rev. Lett. **112**, 223902 (2014).
20. I. Dicaire, V. Jukna, C. Praz, C. Milian, L. Summerer, A. Couairon. Spaceborne laser filamentation for atmospheric remote sensing. Laser Photonics Reviews **10**, 481-93 (2016).

21. E. L. Dawes & J. H. Marburger. Computer studies in self-focusing. Phys. Rev. **179**, 3, 862-868 (1969).
22. J. H. Marburger. Self-focusing: Theory. Prog. Quant. Electron. **4**, 35-110 (1975).
23. W. Liu, Q. Luo, F. Théberge, H. L. Xu, S. A. Hosseini, S. M. Sarifi, and S. L. Chin. The influence of divergence on the filament length during the propagation of intense ultra-short laser pulses. Appl. Phys. B **82**, 373–376 (2006).
24. S. Tzortzakis, B. Prade, M. Franco, A. Mysyrowicz. Time-evolution of the plasma channel at the trail of a self-guided IR femtosecond laser pulse in air. Optics Communications **181**, 123 (2000).
25. H. D. Ladouceur, A. P. Baronavski, D. Lohrmann, P. W. Grounds, P. G. Girardi. Electrical conductivity of a femtosecond laser generated plasma channel in air. Optics Communications **189**, 107-111 (2001).
26. Y.-H. Chen, S. Varma, T. M. Antonsen, and H. M. Milchberg. Direct measurement of the electron density of extended femtosecond laser pulse-induced filaments. Phys. Rev. Lett. **105**, 215005 (2010).
27. C. Hauri, W. Kornelis, F. Helbing, A. Heinrich, A. Couairon, A. Mysyrowicz, J. Biegert, and U. Keller. Generation of intense, carrier-envelope phase-locked few-cycle laser pulses through filamentation. Applied Physics B **79**, 673 (2004).
28. A. Mysyrowicz, A. Couairon, and U. Keller. Self-compression of optical laser pulses by filamentation. New Journal of Physics **10**, 025023 (2008).
29. K. Stelmaszczyk, P. Rohwetter, G. Mejean, J. Yu, E. Salmon, J. Kasparian, R. Ackermann, J.-P. Wolf, and L. Woste. Long-distance remote laser-induced breakdown spectroscopy using filamentation in air. Appl. Phys. Lett. **85**, 3977–3979 (2004).
30. D. J. Cook and R.M. Hochstrasser. Intense terahertz pulses by four-wave rectification in air. Opt. Lett. **25**, 1210 (2000).
31. C. D'Amico, A. Houard, M. Franco, B. Prade, A. Mysyrowicz, A. Couairon, V. T. Tikhonchuk. Conical forward THz emission from femtosecond-laser-beam filamentation in air. Phys. Rev. Lett. **98**, 235002 (2007).
32. J. Yao, G. Li, C. Jing, B. Zeng, W. Chu, J. Ni, H. Zhang, H. Xie, C. Zhang, H. Li, H. Xu. Remote creation of coherent emissions in air with two-color ultrafast laser pulses. New J. Phys. **15**, 023046 (2013).
33. M. Châteauneuf, S. Payeur, J. Dubois, J.-C. Kieffer; Microwave guiding in air by a cylindrical filament array waveguide. Appl. Phys. Lett. **92**, 091104 (2003).
34. B. Prade, A. Houard, J. Larour, M. Pellet, A. Mysyrowicz. Transfer of microwave energy along a filament plasma column in air. Applied Physics B **123**, 40 (2017).
35. P. Walch, L. Arantchouk, B. Mahieu, M. Lozano, Y.-B. André, A. Mysyrowicz, A. Houard. Study of consecutive long-lived meter-scale laser-guided sparks in air. Physics of Plasmas **30**, 083503 (2023) .
36. N. Jhajj, E.W. Rosenthal, R. Birnbaum, J.K.. Wahlstrand, H. Milchberg. Demonstration of long-lived high-power optical waveguides in air. Physical Review X **4**, 011027 (2014).
37. S. Fu, B. Mahieu, A. Mysyrowicz, A. Houard. Femtosecond filamentation of optical vortices for the generation of optical air waveguides. Opt. Lett. **47**, 5228-5231 (2022).

38. P. J. Skrodzki, T. Nutting, M. Burger, L. A. Finney, J. Nees, and I. Jovanovic. Guiding of Spectroscopic Signal with a Concatenated Filament-Driven Waveguide. in CLEO 2023, Technical Digest Series (Optica Publishing Group, 2023), paper ATh4I.4.
39. A. Houard, P. Walch, T. Produit, V. Moreno, B. Mahieu, A. Sunjerga, C. Herkommer, A. Mostajabi, U. Andral, Y.-B. André, M. Lozano, L. Bizet, M. C. Schroeder, G. Schimmel, M. Moret, M. Stanley, W. A. Rison, O. Maurice, B. Esmiller, K. Michel, W. Haas, T. Metzger, M. Rubinstein, F. Rachidi, and J.-P. Wolf. Laser-guided lightning. Nat. Photonics **17**, 231 (2023).
40. G. Fibich and B. Ilan. Vectorial and random effects in self-focusing and in multiple filamentation. Physica D: Nonlinear Phenomena. **157**, 112–146 (2001).
41. W. Liu and S.L. Chin. Direct measurement of the critical power of femtosecond Ti:sapphire laser pulse in air. Opt. Express **13**, 5750-5755 (2005).
42. P. Walch, B. Mahieu, V. Moreno, T. Produit, U. Andral, Y-B. André, L. Bizet, M. Lozano, C. Herkommer, M. Moret, R. Jung, R. Bessing, S. Klingebiel, Y. Bertho, T. Metzger, A. Mysyrowicz, J-P. Wolf, J. Kasparian & A. Houard. Long distance laser filamentation using Yb:YAG kHz laser. Sci. Rep. **13**, 18542 (2023).
43. R. Löscher, V. Moreno, D. Adamou, D. K. Kesim, M. C. Schroeder, M. Clerici, JP Wolf, C. J. Saraceno. High-power sub-picosecond filamentation at 1.03 µm with high repetition rates between 10 and 100 kHz. APL Photonics **8**, 111303 (2023).
44. F. Yin, TJ Wang, Y. Liu, J. Long, Y. Wei, B. Zhu, K. Zhou, and Y. Leng. Pulse repetition rate effect on the plasma inside femtosecond laser filament in air, Chin. Opt. Lett. **22**, 013201 (2024).
45. P. Polynkin, M. Kolesik, J. V. Moloney, G. A. Siviloglou, and D. N. Christodoulides. Curved plasma channel generation using ultraintense Airy beams. Science **324**, 229–232 (2009).
46. P. Polynkin, C. Ament, and J. V. Moloney. Self-focusing of ultraintense femtosecond optical vortices in air. Phys. Rev. Lett. **111**, 023901 (2013).
47. P. Polynkin, M. Kolesik, A. Roberts, D. Faccio, P. Di Trapani, and J. Moloney. Generation of extended plasma channels in air using femtosecond Bessel beams. Opt. Express **16**, 15733-15740 (2008).
48. M. Burger, P. Polynkin, and I. Jovanovic. Filament-induced breakdown spectroscopy with structured beams. Opt. Express **28**, 36812-36821 (2020).
49. F. Théberge, W. Liu, P. T. Simard, A. Becker, and S. L. Chin. Plasma density inside a femtosecond laser filament in air: Strong dependence on external focusing. Phys. Rev. E **74**, 036406 (2006).
50. T. D. Grow and A. L. Gaeta. Dependence of multiple filamentation on beam ellipticity. Opt. Express **13**, 4594-4599 (2005)
51. P. Polynkin, M. Kolesik, and J. V. Moloney. Extended filamentation with temporally chirped femtoseeond Bessel-Gauss beams in air. Opt. Express. **17**, 575–584 (2009).
52. M. Scheller, M. S. Mills, M.-A. Miri, W. Cheng, J. V. Moloney, M. Kolesik, P. Polynkin, and D. N. Christodoulides. Externally refuelled optical filaments. Nat. Photon. **8**, 297–301 (2014).

53. J. Papeer, M. Botton, D. Gordon, P. Sprangle, A. Zigler and Z. Henis. Extended lifetime of high density plasma filament generated by a dual femtosecond–nanosecond laser pulse in air. New J. Phys. **16** 123046 (2016).
54. S. Tzortzakis, G. Méchain, G. Patalano, M. Franco, B. Prade and A. Mysyrowicz. Concatenation of plasma filaments created in air by femtosecond infrared laser pulses. Appl Phys B **76**, 609–612 (2003).
55. P. Polynkin, Multi-pulse scheme for laser-guided electrical breakdown of air. Appl. Phys. Lett. **111**, 161102 (2017).
56. P. Polynkin, Z. Samsonova, A. Englesbe, A. Lucero, J. Elle, A. Schmitt-Sody, Channeling the dielectric breakdown of air by a sequence of laser-generated plasma filaments. JOSA B **36**, 3024 (2019).
57. J. Papeer, R. Bruch, E. Dekel, O. Pollak, M. Botton, Z. Henis, A. Zigler, Generation of concatenated long high density plasma channels in air by a single femtosecond laser pulse. Appl. Phys. Lett. **107,** 124102 (2015).
58. Y. Liu, M. Durand, S. Chen, A. Houard, B. Prade, B. Forestier, A. Mysyrowicz, Energy exchange between femtosecond laser filaments in air. Physical Review letters **105**, 055003 (2010).
59. D. V. Pushkarev, A. S. Lar'kin, E. V. Mitina, N. A. Zhidovtsev, D. S. Uryupina, R. V. Volkov, S. V. Karpeev, S. N. Khonina, A. A. Karabutov, Yu. E. Geints, O. G. Kosareva, and A. B. Savel'ev. Robust multifilament arrays in air by Dammann grating. Opt. Express **29**, 34189-34204 (2021).
60. J. Zhu, Z. Ji, Y. Deng, J. Liu, R. Li. Z. Xu. Study on lifetime of a plasma channel induced by femtosecond laser pulses and an external electric field. Acta Optica Sinica **27**, 6 (2007).

Chapter 2

Femtosecond Filaments Generated by Laguerre-Gaussian Beams

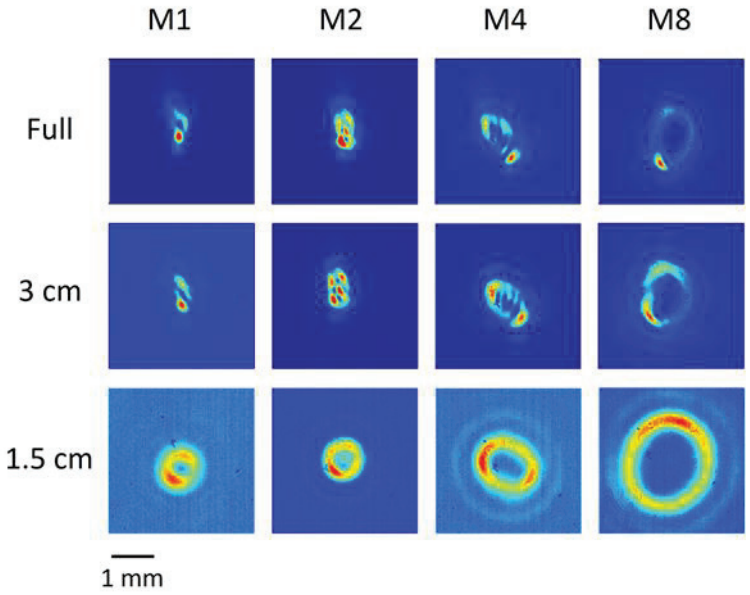

Figure 2.1. Profile of the Vortex Beam at the focus measured using a CMOS Camera for different topological orders *m* and different beam diameters.

In 1992, the introduction of photonic orbital angular momentum (OAM) made the experimental realization of Laguerre-Gaussian (LG) beams possible [1]. Over the past 25 years, significant achievements have been made in the generation, application, and detection of OAM and LG beams. In the last 15 years, researchers have used LG beams to generate filamentation in solid, liquid, and gas media. This has led to several important applications, such as laser material processing [2] air waveguides [3-6], drilling holes in clouds for optical communication [7], and exploring vortex lasing emission in nitrogen gas [8,9], thereby opening up new avenues for research and applications in the field.

2.1 Laguerre-Gaussian beams

2.1.1 Description of Laguerre-Gaussian beams

In 1953, Townes, Gordon, and Zeiger demonstrated the first microwave amplification by stimulated emission of radiation (Maser) at Columbia University. [10] In 1958, Schawlow and Townes proposed that the technology used in Masers could be applied to the optical domain. By constructing a centimeter-scale resonant cavity and selecting an appropriate gain medium, infrared laser output could be produced under the pumping of sufficiently energetic incoherent light [11].

In 1960, Maiman utilized this principle to create the first laser at Hughes Aircraft Company [12]. This development sparked interest in the modes of resonators. Fox and Li used diffraction optics methods to calculate the modes within a Fabry-Perot cavity [13]. They first assumed that the establishment of modes in a laser occurs through light oscillating back and forth within the resonator. By using computer simulations to model the repeated reflections of light within the resonator, they discovered that after a sufficient number of cycles, the light field no longer changes with each reflection cycle, resulting in the formation of stable modes within the resonator.

Meanwhile, Goubau *et al.* proposed a hypothesis: maybe there exist beams whose cross-sectional amplitude distribution can replicate the initial light field at a certain propagation distance. If such beams exist, their phase changes could be reconstructed to match the initial phase distribution through appropriate phase shifts [14]. Consequently, by using different phase modulation devices, a beam could propagate while maintaining its original field distribution.

Through theoretical derivation, they found that these elementary wave beams could be described using Laguerre polynomials, and any light field could be represented by these elementary beams [14]. In 1966, Kogelnik and Li summarized the previous work related to beams and resonators [15]. They started from the scalar wave equation and, under cylindrical coordinates, applied the paraxial approximation to the equation, obtaining the eigenvalue solutions of the wave equation. The solutions can be expressed in the following form:

$$u(r,\varphi,z)=\frac{C_{lp}^{LG}}{w(z)}\left(\frac{\sqrt{2}r}{w(z)}\right)^{|l|}\exp\left(-\frac{r^2}{w^2(z)}\right)L_p^{|l|}\left(\frac{2r^2}{w^2(z)}\right)$$
$$\times\exp\left(-ik\frac{r^2}{2R(z)}\right)\exp(-il\varphi)\exp(-ikz)\exp(-i\psi(z)) \quad , \qquad (2.1.1)$$

where $L_p^{|l|}$ are the generalized Laguerre polynomials, C_{lp}^{LG} is a normalization constant defined as

$$C_{lp}^{LG}=\sqrt{\frac{2p!}{\pi(p+|l|)!}}, \qquad (2.1.2)$$

$w(z)$ is the beam radius at a distance *z*, $R(z)$ is the curvature radius, and $\psi(z)$ is the Gouy phase.

Their relationships with the Rayleigh length z_R (where $z_R = \pi w_0^2 / \lambda$, and w_0 is the beam waist radius) are defined by

$$\begin{cases} w(z) = w_0 \sqrt{1 + \left(\dfrac{z}{z_R} \right)^2} \\ R(z) = z \left[1 + \left(\dfrac{z_R}{z} \right)^2 \right] \\ \psi(z) = (|l| + 2p + 1) \arctan \left(\dfrac{z}{z_R} \right) \end{cases} \tag{2.1.3}$$

These equations describe the variation of the beam radius, the radius of curvature, and the Gouy phase as the beam propagates.

l represents the azimuthal index, which can take any integer value. p represents the radial index, which takes positive integers values. Beams with the form of equation (2.1.1) are called LG (Laguerre-Gaussian) beams. Different combinations of l and p yield different LG beams.

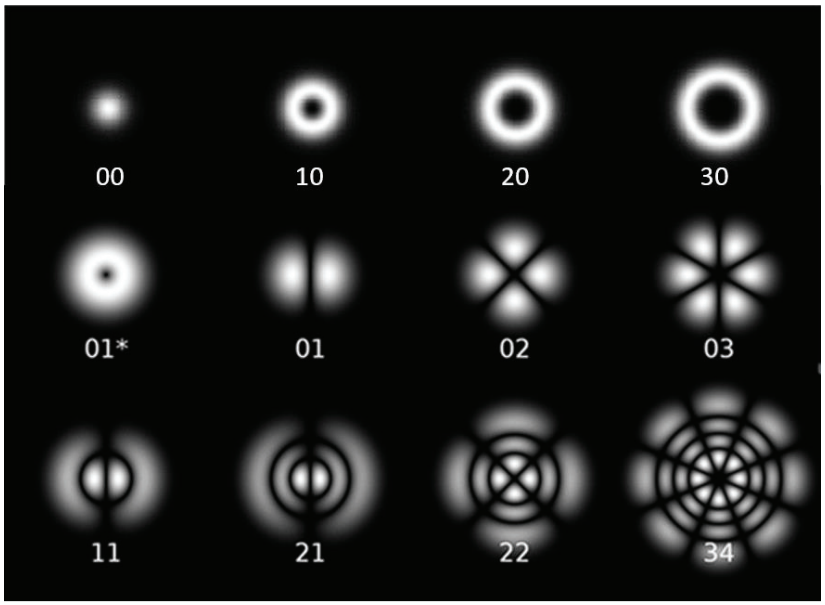

Figure 2.1.1. Spatial energy distributions of different Laguerre-Gaussian modes.

From Figure 2.1.1, it can be seen that when l = 0, the LG beam degenerates into a vortex beam, containing a helical phase and a central phase singularity, corresponding to the beam structure shown in the first row of Figure 2.1.1.

In our experiment, we also utilized beams referred to as 4- or 6-sectors beams. These correspond to the case where the Laguerre-Gaussian beam has $p = 0$ and $l \neq 0$. Under such conditions, in both the phase plane and beam profile, the beam is divided into $2l$ segments with alternating 0 and π phase components. This configuration corresponds to the beam structure illustrated in the second row of Figure 2.1.1.

2.1.2 Generating Laguerre-Gaussian beams in experiments

Over the decades, many methods have been developed to experimentally generate Laguerre-Gaussian (LG) beams. For example, Allen *et al.* proposed using a mode converter composed of two cylindrical lenses to transform a Hermite-Gaussian (HG) beam into an LG beam [1]. As shown in Figure 2.1.2, the converter is composed of two cylindrical lenses with the same focal length f, separated by a distance $1.414\ f$. When an HG beam is sent on one side, an LG beam of the same order is formed at the output of the optical system. This mode converter can also be used to detect the topological charge of LG beams as shown in Figure 2.1.2 (b).

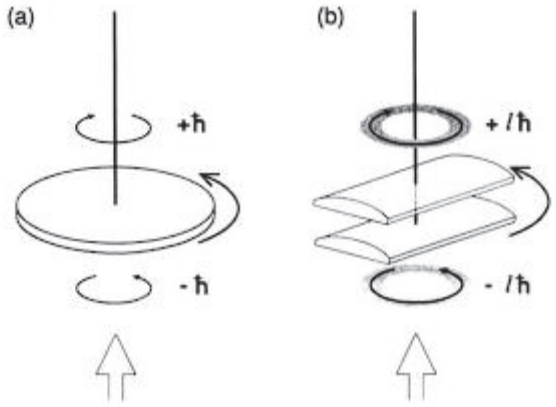

Figure 2.1.2. Schematic of angular momentum measurement of light: (a) Measurement of spin angular momentum (polarization state). (b) Measurement of orbital angular momentum (from [1]).

It is worth noting that in recent experiments on generating vortex air lasers using vortex filaments, this method has been employed to detect the topological charge of the produced LG lasing signal, although they used only one cylindrical lens [8,9], as shown in Figure 2.1.3.

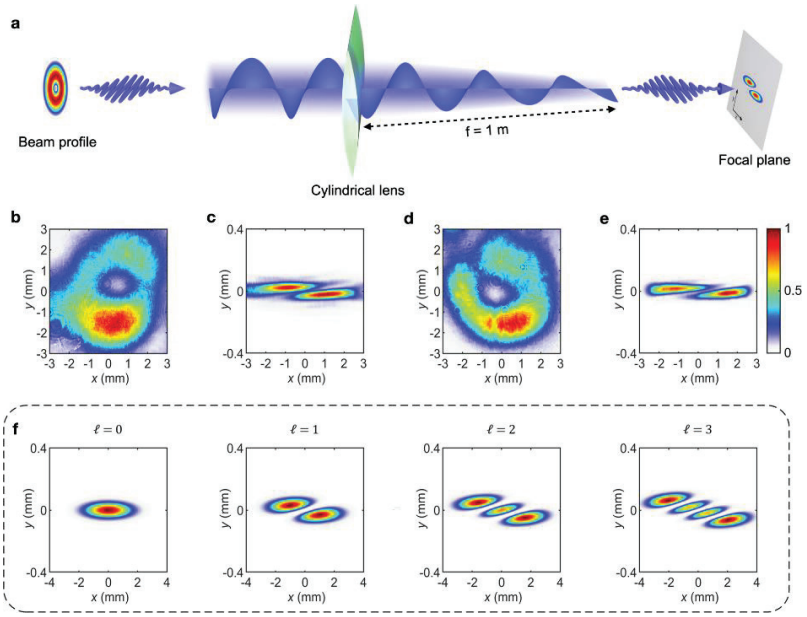

Figure 2.1.3. A cylindrical lens is used to detect the topological charge of a generated air laser signal. (a) is the experimental setup. (b) and (d) show the measured intensity distribution of lasing signal in the experiment. (c) and (e) are the beam profile at the focal point after passing through the cylindrical lens. (f) is the simulation of vortex beams with different topological charges (i.e., 0, 1, 2, and 3) after the cylindrical lens at the focal point.

After Allen *et al.* demonstrated in 2014 that orbital angular momentum (OAM) depends solely on the wavefront phase [16], the generation of OAM was simplified. We only need to modulate the wavefront phase of the beam to achieve the desired phase distribution. This can typically be done using spiral phase plates, q-plates (vortex half-wave plates), holographic gratings with "fork" geometry, among other methods. I will introduce these different methods below.

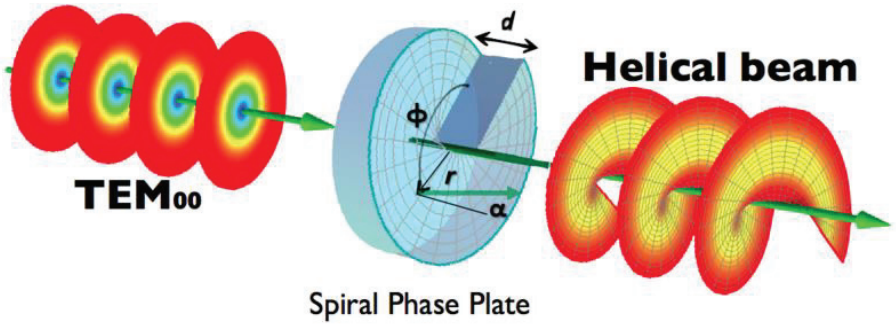

Figure 2.1.4. Principle of a spiral phase plate generating a vortex beam.

Figure 2.1.4 illustrates the principle of generating a vortex beam using a spiral phase plate. The phase plate is made of a transparent medium, whose thickness varies linearly with the azimuthal angle ψ around the optical axis. If the thickness variation over one full rotation is d , the topological charge of the loaded OAM is given by

$$m = \pm \frac{(n-1)d}{\lambda}, \tag{2.1.4}$$

where λ is the wavelength of the incident beam and n is the refractive index of the medium. Since the phase mask is generally of the transmission type, the sign of m can be changed by flipping the spiral phase plate. As shown in equation 2.1.4, this type of phase mask is suitable for a specific wavelength. Deviating from the designed working wavelength causes m to become fractional, resulting in fractional OAM. In my thesis, all phase plates from Holo/Or were manufactured using this method of introducing different optical path differences.

In our experiment, some of the phase plates were purchased from Thorlabs, specifically vortex half-wave plates. The working principle of vortex half-wave plates is not based on introducing an optical path difference but rather on generating OAM (Orbital Angular Momentum) through geometric phase (Pancharatnam's phase). In 2002, Erez Hasman *et al.* first proposed to use optical devices with a geometric phase that varies helically in space to

impart a helical wavefront to the beam [17]. This method of controlling the wavefront through geometric phase relies on the spatial anisotropic parameters along the light propagation path. By engineering the parameter space of the structure, it is possible to control the wavefront of the beam.

When a beam of left (or right) circularly polarized light passes through a half-wave plate, it is converted into right (or left) circularly polarized light with a certain geometric phase delay. The magnitude of the geometric phase is determined by the orientation of the fast axis of the half-wave plate. In a standard half-wave plate, the fast axis is fixed, whereas in a vortex half-wave plate, the fast axis can be considered to rotate around a central point. OAM can be achieved when the geometric phase change of one rotation is $\exp(il\varphi)$.

In our experiment, we only employed these two methods to generate Laguerre-Gaussian beams. However, there are many other techniques available for generating LG beams, such as computer-generated holograms, spatial light modulators (SLMs), and cylindrical lens mode converters.

2.1.3 Limitations in generating Laguerre-Gaussian beams in experiments

In experiments, the most commonly used methods for generating Laguerre-Gaussian (LG) beams are the two methods mentioned previously. However, there are several limitations associated with the generation of LG beams:

1. **Peak power of the beam:** High peak power can damage the optical phase plates. Furthermore, if the beam propagates through any nonlinear medium, the high peak power will induce more optical nonlinear responses, which can destroy the original phase mode of the beam [18].
2. **Sensitivity to beam quality:** LG beams are highly sensitive to the quality of the incident beam. Phase plates are designed to work optimally with a perfect Gaussian beam, but ensuring a perfectly Gaussian incident pulse in an experimental setup is challenging. Any imperfections in the incident beam phase can affect the quality of the generated LG beam.
3. **Defects in phase plates:** Defects in the phase plates and precision in alignment also significantly impact the generation of LG beams. Any imperfections or misalignments can lead to deviations from the desired beam profile.

For filamentation studies, maintaining a near-perfect phase mode is crucial. LG filaments are often used for air waveguides, to create a fiber-like structure in the air. The internal diameter of the filament is a critical parameter. If the phase mode of the LG filament is severely disrupted, all filaments will overlap, making it impossible to create an air waveguide.

To achieve a satisfactory LG beam, we commonly use an iris to reduce the numerical aperture of the beam. This approach has three benefits:

- The quality of the laser pulse output is generally better near the center and poorer at the edges. Reducing the diameter enhances the quality of the central portion of the beam.

- It smoothen the beam's focusing, reducing nonlinear interactions in the medium and minimizing the damage to the original phase.
- Reducing the numerical aperture extends the filament length and increases the internal diameter of the LG filament.

However, this method also introduces some issues. If the incident beam is a Gaussian beam, reducing the numerical aperture will turn it into a super-Gaussian beam, potentially affecting the filamentation process. Since our laser beam has a super-Gaussian intensity profile, we can only work with super-Gaussian beams in any case.

Most of the results in this thesis are obtained using the laser we call "ENSTAmobile," a Ti:Sa CPA laser system from Amplitude Technologies delivering laser pulses at 10 Hz with a central wavelength of 800 nm, which produces a super-Gaussian beam.

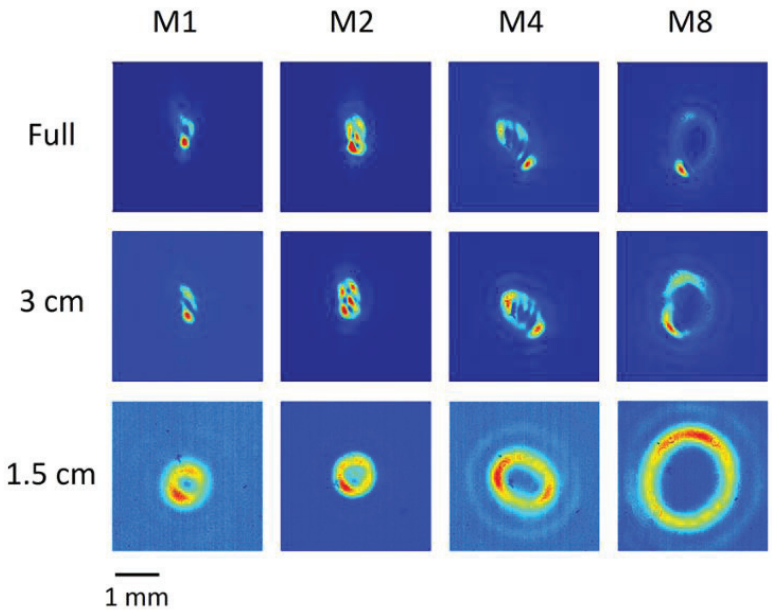

Figure 2.1.5. Beam profiles of vortex beam with topological orders 1, 2, 4 and 8 measured at the focal point of a lens f = 5 m with different iris diameters.

As an example, Fig. 2.1.5. shows the vortex beam profiles at the focal point using a 5-meter external focusing lens with different iris diameters. It can be observed that with the full beam (4 cm) and with a 3 cm diameter beam, the beam profile at the focal point is not ring-shaped, resembling Hermite-Laguerre beams, especially for the M1 case. Only when the iris diameter is sufficiently reduced do we obtain a satisfactory ring-shaped beam profile.

Under the same conditions, we also measured the beam profiles at the focal point using a 1-meter external focusing lens. Despites the stronger focusing, the LG beam's behavior at the focal point remains consistent with that observed under weak focusing. This demonstrates that the imperfections at the focus are mainly due to distortions in the non-central regions of the incident beam rather than to the influence of the numerical aperture.

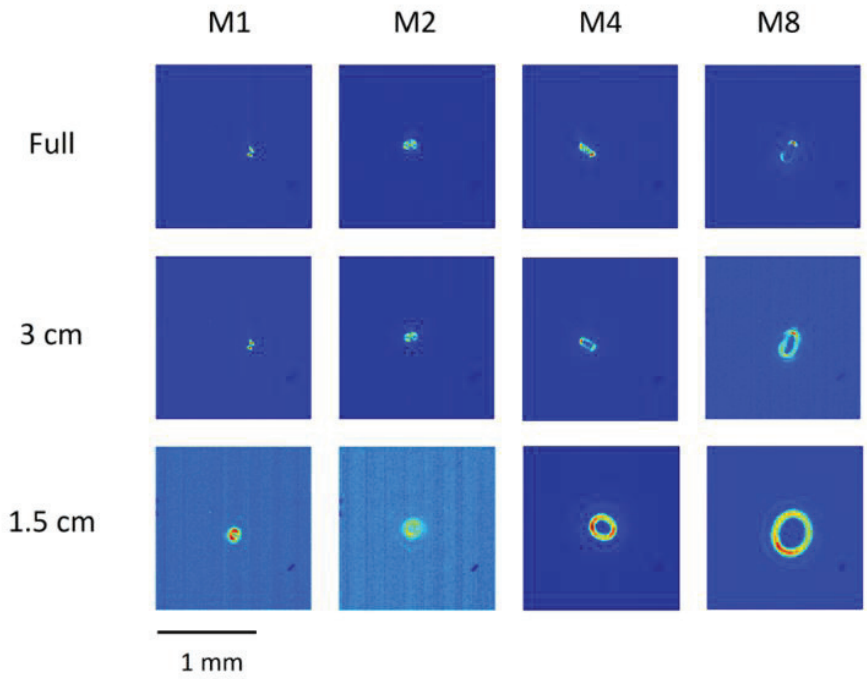

Figure. 2.1.6. Beam profiles at the focal point with different Iris diameters (external focusing with a 1 m Lens).

2.2 Measurement of the critical power for self-focusing with Laguerre-Gaussian beams

Filaments are generated due to the Kerr self-focusing and defocusing effects of the beam in the optical medium [19]. This complex nonlinear propagation process can be succinctly summarized as follows: when the incident laser power in air (or optical medium) exceeds a specific threshold, self-focusing effects can overcome beam diffraction, leading to beam collapse and the formation of filaments. This specific threshold is known as the critical power for self-focusing P_{cr}, which is a crucial physical parameter in filamentation studies and various filamentation applications.

In this section, we will describe our detailed study of the critical power P_{cr} for Laguerre-Gaussian beams generated in air using acoustic methods. We will also compare this method with other methods and discuss the influence of the external focusing this measurement.

2.2.1 Previous studies on CR power of Laguerre-Gaussian beams

Before introducing the critical power of Laguerre-Gaussian beams, let's first review the critical power of Gaussian beams. After more than 20 years of detailed research, it is now generally accepted that the critical power for Gaussian beams is given by [19]

$$P_{cr} = \frac{3.77\lambda^2}{8\pi n_2 n_0}, \tag{2.2.1}$$

where λ is the central wavelength of the laser pulse, and n_0 and n_2 denotes the linear refractive index and the nonlinear refractive index.

As early as 2008, Fibich *et al.* calculated the critical power of vortex beam for a continuous wave [20]. The result of his calculation is

$$P_{cr}^{(m)} = 4\sqrt{3}mP_{cr}^{(0)}, \tag{2.2.2}$$

where $P_{cr}^{(0)}$ is the self-focusing critical power of a Gaussian beam equation (2.2.1).

But for a femtosecond pulse, group velocity dispersion significantly increases the critical power for self-focusing [21,22]. Additionally, the beam duration affects the nonlinear refractive index (n_2) coefficient, thereby influencing the critical power for self-focusing [23,24]. The critical power for self-focusing of femtosecond vortex beams needs to be determined experimentally.

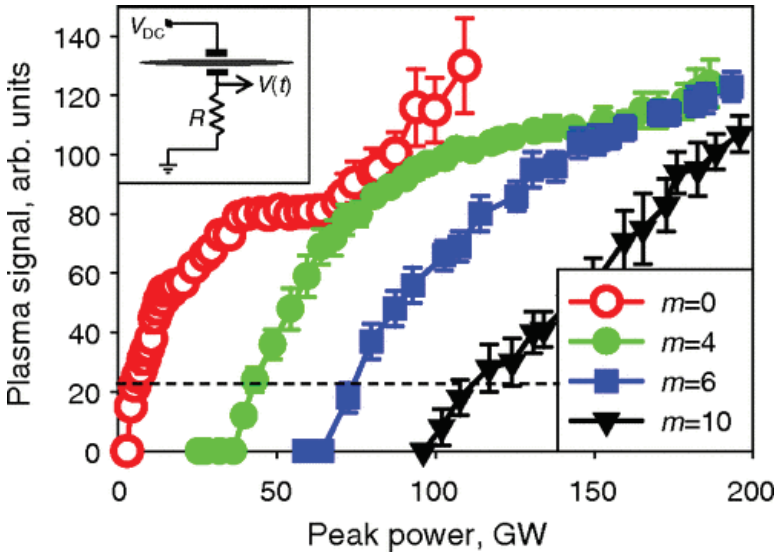

Figure 2.2.1. Measurement of the critical power of filaments produced by vortex beams with different topological number (m) using an air capacitor: electric signal detected between two electrodes as a function of the laser input peak power. The red line represents the Gaussian beam, while the green, blue, and black lines represent the cases with $m = 4$, 6, and 10, respectively. The inset in the upper left corner shows a schematic of the measurement setup (from [23]).

In 2013, Polynkin *et al.* proposed a method using a capacitor device to measure the critical power of Laguerre-Gaussian beams [25], as shown in Figure 2.2.1. They used a telescope with f = 3000 mm to focus the beam, with a pulse duration of 38 fs. They applied a high voltage across two flat metallic electrodes. When there is no plasma between the electrodes, no current flows in the system. When a plasma is generated, electrons released within the filament are accelerated by the DC electric field. Although most of the released electrons recombine with the nuclei, a small portion of the electrons reach the electrodes, causing a surge in the circuit current. By measuring the pulse voltage across the capacitor, the magnitude of the disturbance caused by the filament can be determined, which in turn allows the determination of the laser beam critical power. They presented the results for $P_{cr}^{(m)}$ / $P_{cr}^{(0)}$, as shown in Figure 2.2.2. Ultimately, they estimated

$$P_{cr}^{(m)} = 4\sqrt{3}\,/\,1.7mP_{cr}^{(0)}\,. \tag{2.2.3}$$

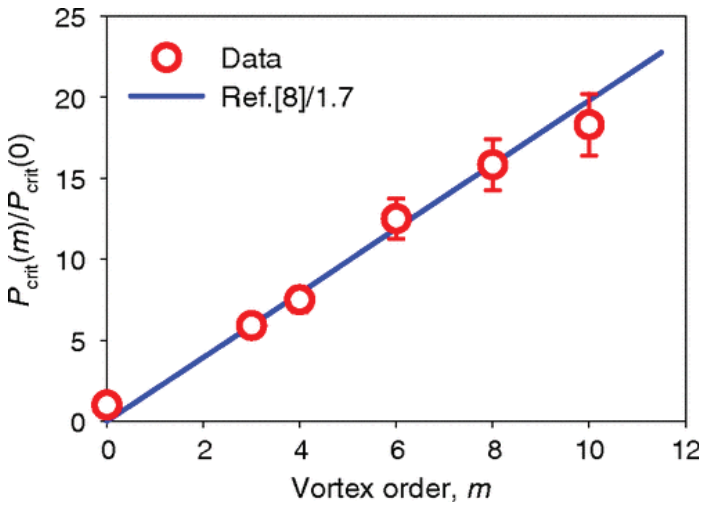

Figure 2.2.2. Experimentally measured critical power for filamentation of different m vortex beams (red circles) compared with theoretical results from [18] divided by 1.7 (from [25]).

In 2023, Wei Liang *et al.* determined the critical power for self-focusing of femtosecond vortex beams in air through side fluorescence measurement [26]. They measured the critical power for vortex beams with $m = 1,\ 2$, and 3. They used a focal length of $f = 500$ or $750\ mm$, with a pulse duration of $65\ fs$. They found that the critical power is approximately

$$P_{cr}^{(m)} \approx 2mP_{cr}^{(0)}(m \neq 0)\,. \tag{2.2.4}$$

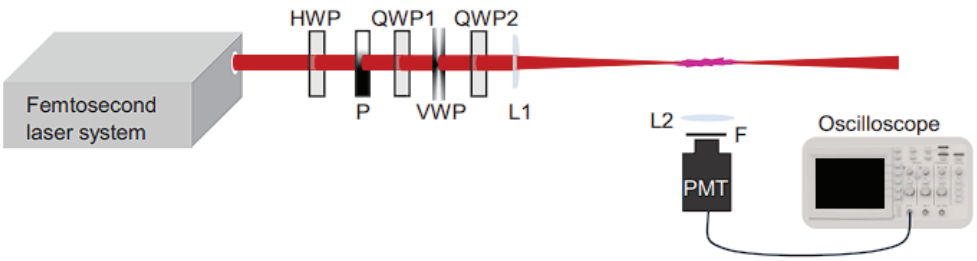

Figure 2.2.3. Schematic diagram of the setup for measuring the side fluorescence of the plasma using a photomultiplier tube (PMT) (from [26]).

These different methods yield different results, thus sparking our research interest in this issue.

2.2.2 Acoustic measurement of P_{CR} of Laguerre Gaussian beam

During the filamentation process, laser energy rapidly deposits in the medium, generating transverse acoustic waves [27,28]. This is a necessary condition for filament formation. Therefore, by measuring the acoustic signals, we can determine the presence of filaments.

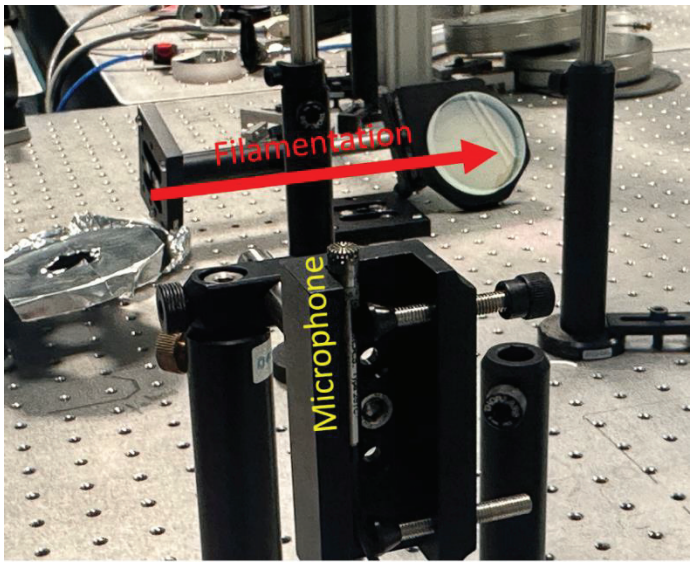

Figure 2.2.4. Image of the microphone measuring the acoustic signal emitted by the filament.

We used a broadband microphone (GRAS Model 46BH 1⁄4”) in our experiment, as shown in Fig. 2.2.4. The microphone was positioned 3 cm below the geometric focus of the beam. Here, we employed an external focusing lens with $f = 1000$ mm to generate the filament. The energy of the incident beam was measured using a joulemeter from Gentec.

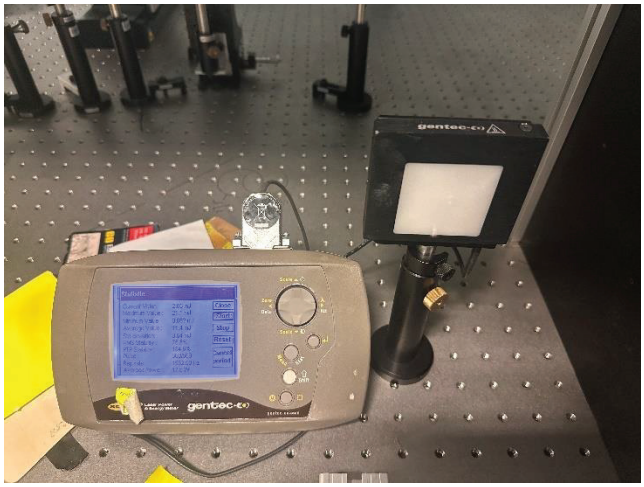

Figure 2.2.5. Joulemeter from Gentec.

Due to the fact that different pulse durations will introduce different nonlinear refractive indices (n_2), thereby affecting the critical power, we measured the critical power for filamentation of LG beams with two different pulse durations, 50 fs and 500 fs. Figure 2.2.6 shows the acoustic signals generated by vortex beams or 4-sectors and 6-sectors beams at different energies. We can see that each acoustic signal changes slowly at low energies but seems to increase rapidly after reaching a certain threshold. By performing a linear fit, we can quickly determine this threshold. This threshold corresponds to the critical power as detailed in [26].

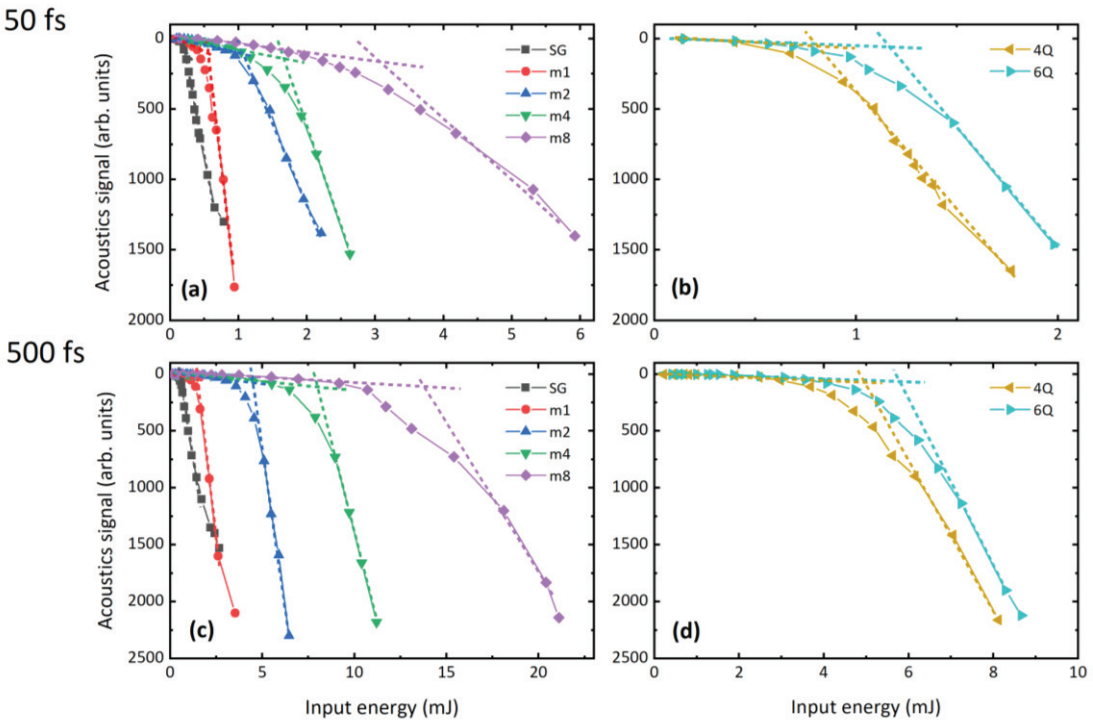

Figure 2.2.6. Amplitude of the acoustic signal measured as a function of the energy of the incident pulses. (a) and (b) are measured with a laser pulse duration of 50 fs, (c) and (d) with a pulse duration of 500 fs. (a) and (c) show the results for super-Gaussian beams and vortex beams. (b) and (d) show the results for 4-sectors and 6-sectors beams.

Table 2.2.1. presents the critical power measurements for different LG beams. It can be seen that for vortex beams, the critical power increases with the increase in topological number. For 4-sectors and 6-sectors beams, the critical power of the 4-sectors beam is lower than that of the 6-sectors beam. For vortex beams, this overall trend is consistent with previous studies [20,25,26]. For sectors beams, this result is easily understandable. The more the beam is divided, the less power each part receives, and thus the critical power required to generate the first filament is higher. For a 50 fs, the measured critical power for sector beam corresponds approximately to the critical power for a SG beam multiplied by the number of sectors.

	SG	m1	m2	m4	m8	4Q	6Q
50fs	0.22 mJ	0.55 mJ	1.07 mJ	1.66 mJ	3 mJ	0.81 mJ	1.16 mJ
Pcr (50 fs) in GW	4.4	11	21	33	60	16	22
P/Pcr (SG)	1	2.5	4.77	7.5	13.6	3.64	5
500fs	0.55 mJ	1.53 mJ	4.4 mJ	8 mJ	13.8 mJ	4.9 mJ	5.8 mJ
Pcr (500 fs) in GW	1.1	3.06	8.8	16	27.6	9.8	11.6
P/Pcr (SG)	1	2.78	8	14.54	25	8.9	10.5

Table 2.2.1. Critical power for filamentation of LG beams by acoustic measurement

By performing a more detailed analysis of the critical power for vortex beams, we found that the increment in critical power appears to have a linear relationship with the topological charge as shown in Figure 2.2.7:

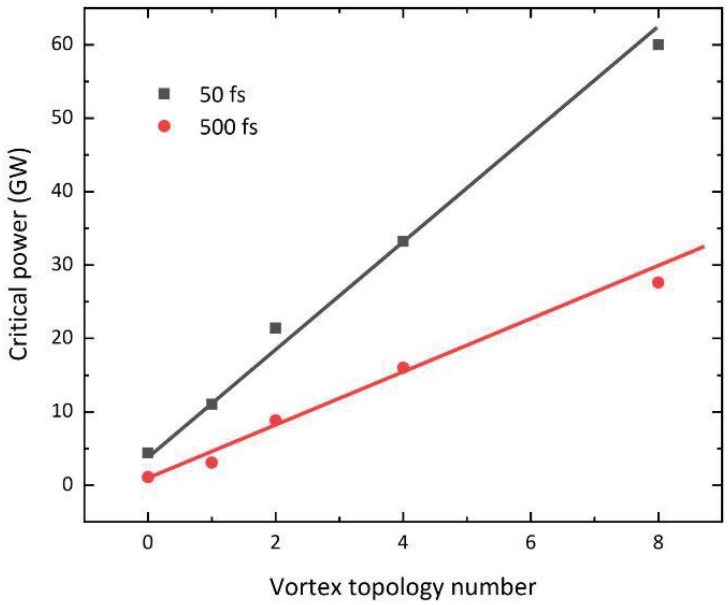

Figure 2.2.7. Relationship between the topological charge of the vortex beams and their critical power for self-focusing.

By performing a linear fit, we obtain the relation between the topological charge and the critical power. For an incident pulse duration of 50 fs, we have:

$$P_{cr}(m)(\mathrm{GW}) = 7.2 * m + 4.4,$$

and for an incident pulse duration of 500 fs, we have

$$P_{cr}(m)(\mathrm{GW}) = 3.67 * m + 1.1.$$

We can see that the laser pulse duration significantly affect the linear fitting parameters of the critical power. We believe this is because different incident pulse durations will significantly impact the value of the nonlinear Kerr refractive index n_2, due to the delayed contribution of n_2.

2.2.3 Comparison of the critical power measured using luminescence emission and acoustic signal

We used a photomultiplier tube (PMT) to detect the luminescence of the plasma and measure the critical power of vortex beams and compared it to the acoustic signals. Our experimental setup is similar to the one described in [26], where a 10 cm focusing lens collects the plasma fluorescence from the side of the filament and focuses it into the PMT.

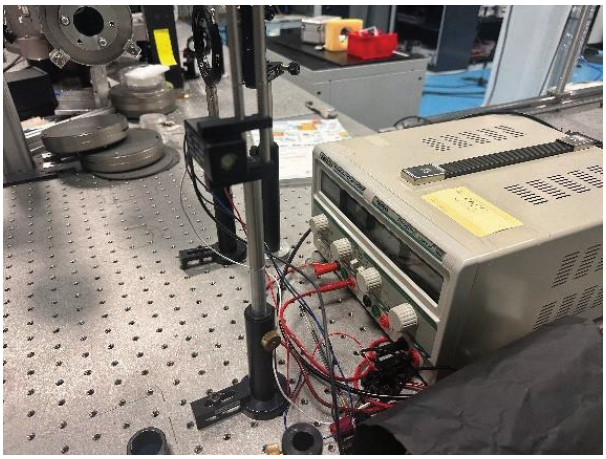

Figure 2.2.8. Photomultiplier tube used to measure the critical power.

Our experimental results are shown in Figure 2.2.9. We measured two cases, SG and m1, with the critical power for SG being 5.3 GW and for m1 being 11.6 GW. Compared to the acoustic signal measurements, which yielded 4.4 GW for SG and 11 GW for m1, we find a very good agreement. Therefore, we believe both methods are reliable. However, since the photomultiplier tube requires complete darkness during measurements, making it more demanding in terms of the measurement environment compared to the acoustic signal method, we ultimately chose to use the acoustic signal method to determine the critical power. Additionally, we noticed that our results differ significantly from those of Liang *et al.* [26], which we believe is due to the use of a much smaller numerical aperture in our case and the fact that the incident beam profile was a super-Gaussian beam.

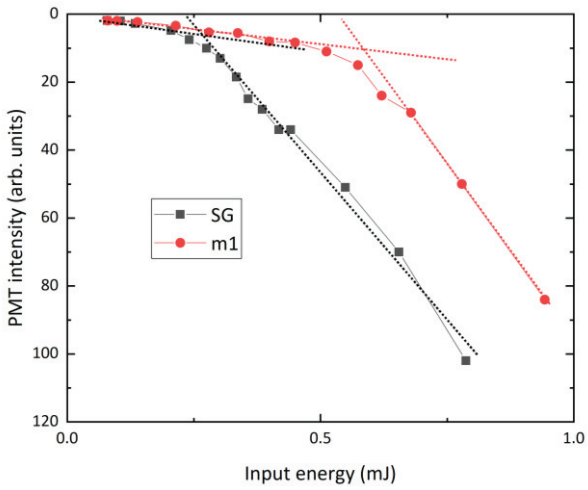

Figure 2.2.9. Amplitude of the lateral luminescence signal from the plasma produced at the focus of the lens detected by a PMT Critical as a function of the laser input energy. The black line represents LG_{00} (SG), and the red line represents LG_{10} (m1). The laser has a pulse duration of 50 fs.

2.2.4 Influence of the beam numerical aperture on the critical power

To study the effect of numerical aperture on the critical power of filaments, we changed the external focusing lens from $f = 1000$ mm to $f = 5000$ mm. Under the same

conditions, except for a pulse duration of 50 fs, we measured the critical power for the super-Gaussian (SG) beam and the m4 beam, as shown in Figure 2.2.10. For comparison, we also included the results for $f = 1000$ in the figure.

Using the same linear fitting method, we determined the critical power for the super-Gaussian beam and the m4 beam to be 32 GW and 76 GW, respectively, with $f = 5000$ mm. It can be seen that the numerical apertures has a significant impact on the critical power of a beam. This effect is often neglected in many experiments where people only consider the critical power of a collimated beam.

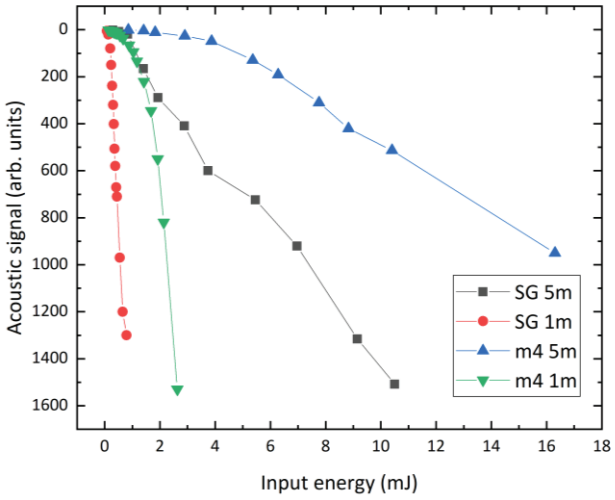

Figure 2.2.10. Effect of the external focusing on the critical power for self-focusing of a beam. The black and red lines represent the SG case. The blue and green lines represent the m4 case.

2.3 Measurement of deposited energy in filaments generated by Laguerre-Gaussian beams

To characterize filaments, another important parameter is the deposited energy. The primary mechanism for energy deposition is the generation of a plasma, which intuitively reflects the quantity of plasma. Additionally, stimulated rotational Raman scattering of air molecules can also produce energy loss of laser pulses. The energy stored in the kinetic and potential energy of the plasma free electrons and the rotational energy of air molecules is ultimately converted to thermal energy in the air after plasma recombination and rotational thermalization. Depending on the experimental conditions, this heating can range from 100 K to over 1000 K. Heating expels matter from the center of the channel, leaving behind a low-density channel. The hydrodynamics of the generation and evolution of these low-density channels are very important. They pave the way for long-distance air waveguides [3-6, 29], guiding high-voltage discharges [30-32] and enhancing the aerodynamics of aircraft [33,34]. All these applications depend on the magnitude of the air fluid dynamics induced by the filament, which is directly related to density of deposited energy. Therefore, studying energy deposition is essential.

To the best of our knowledge, there is no study of the deposition of energy by LG filaments in air, so a detailed analysis of this process is necessary. For the measurement of deposited energy, we used a joulemeter from Gentec, as shown in Figure 2.2.5. We measured the energy after the beam passed through all the optical components but before the filament generation and then measured the energy in the beam after the filament. The difference between these measurements represents the total deposited energy.

First, we measured the deposited energy for a pulse duration of 50 fs at different incident energies, as shown in Figure 2.3.1. Here, we also chose a 1-meter external focusing lens ($f = 1000$ mm). It can be seen that as the laser energy increases, the deposited energy also increases. Additionally, for vortex beams, the deposited energy gradually decreases with increasing topological charge. This is not surprising; in the previous section, we found that the critical power also increases with increasing topological charge, which means that higher topological charges generate fewer filaments at the same energy, resulting in lower deposited energy. Moreover, for a pulse width of 50 fs, 4-sectors ($4q$) and 6-sectors ($6q$) seem to exhibit the same deposited energy. However, as the energy increases, the deposited energy of 4-sectors gradually surpasses that of 6-sectors, possibly due to the generation of superfilaments by 4-sectors at higher energies.

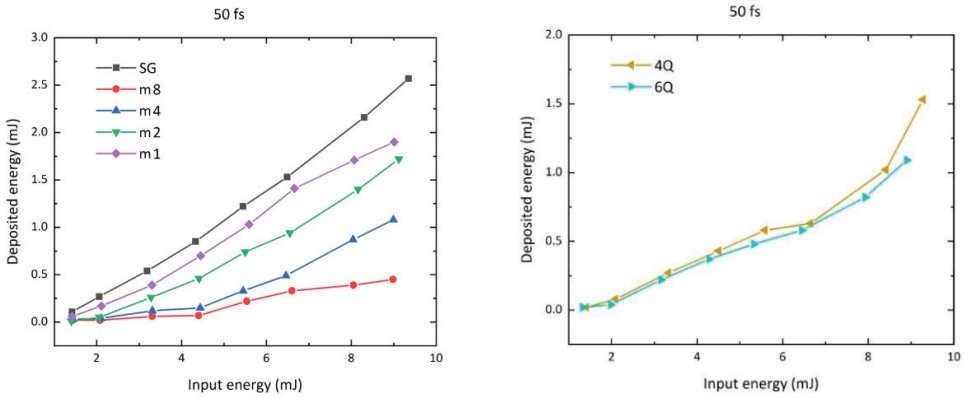

Figure 2.3.1. Deposited energy in LG filaments with a 50 fs incident pulse duration. The left panel shows the results for SG and vortex beams, while the right panel shows the results for 4-sectors and 6-sectors beams. A 1-meter focusing lens ($f = 1000$ mm) was used for external focusing.

We also studied the deposited energy in LG filaments under long pulse conditions (500 fs), as shown in Figure 2.3.2. From this result, we can see that the trend in deposited energy for long pulses is generally similar to that for short pulses, with the deposited energy decreasing as the topological charge increases. However, it is evident that the deposited energy for long pulses is significantly lower compared to short pulses. This is because, although long pulses have a higher nonlinear Kerr refractive index (n_2) and thus a lower critical power, the significant difference in peak power results in much less plasma generation. Additionally, from the 500 fs deposited energy measurements, we can see that almost no energy is deposited below the critical power, and the deposited energy rapidly increases after reaching the critical power. This trend is also observed in the 50 fs results (for m8). This suggests that measuring the deposited energy could be used to determine the critical power, although this method is less sensitive because it is based on the difference between two measurements with an important noise due to shot to shot instability.

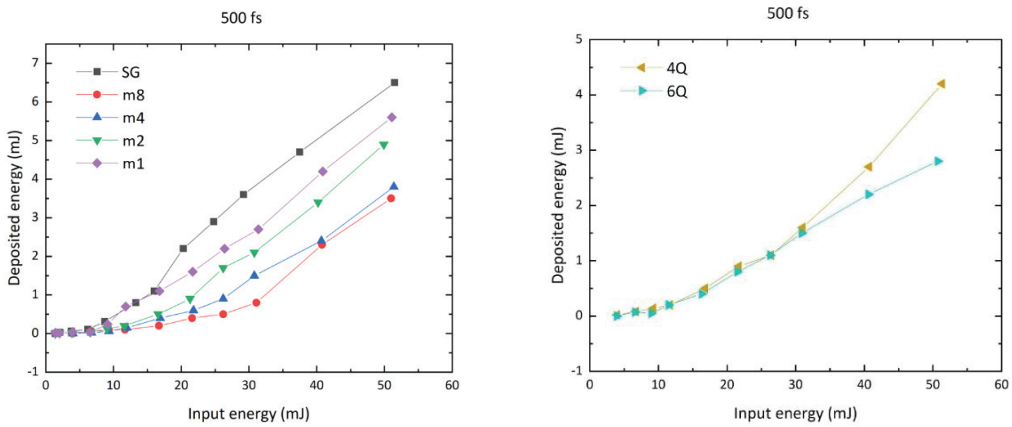

Figure 2.3.2. Deposited energy in LG filaments as a function of the laser input energy for a laser with a pulse duration of 500 fs. The left panel shows the results for SG and vortex beams, while the right panel shows the results for 4-sectors and 6-sectors beams. A 1-meter focusing lens ($f = 1000$) was used for external focusing.

For vortex beams, the measurement results of the deposited energy are very interesting. After the incident pulse energy exceeds the critical power, it seems that different topological charges correspond to different slopes in the deposited energy graph. The lower the topological charge, the higher the slope. For example, in the case of 50 fs, as shown in Figure 2.3.3, it appears that this slope has a linear relationship with the topological charge. This finding may provide a way to detect the topological charge of the incident pulse.

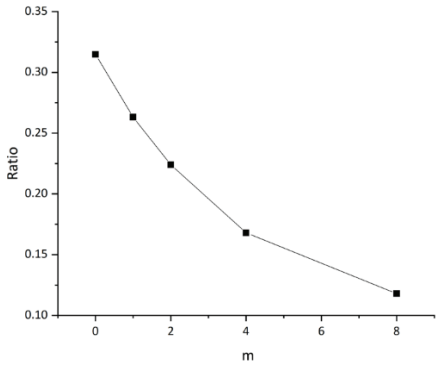

Figure 2.3.3. Ratio of deposited energy to incident energy as a function of the topological charge of vortex beams. The laser has a pulse duration of 50 fs.

2.4 Number of filaments generated by Laguerre-Gaussian beams

In most applications of filaments, we use higher peak power levels, often far exceeding the critical power. Under such conditions, the number and distribution of filaments become important subjects of study. We first measured the distribution of filaments at low energy levels using photosensitive paper, as shown in Figure 2.4.1. It can be observed that the super-Gaussian beam produced a single superfilament, the LG_{10} beam produced two filaments, LG_{20} produced four filaments, LG_{40} produced five filaments, and LG_{80} did not produce any filaments as it did not reach the critical power. The 4-sectors beam produced four filaments, and the 6-sectors beam produced six filaments. It can be seen that if there is sufficient energy, vortex beams with higher topological charges can produce more independent filaments. This is because higher topological charges produce a larger inner diameter, thus providing a greater area for generating more filaments.

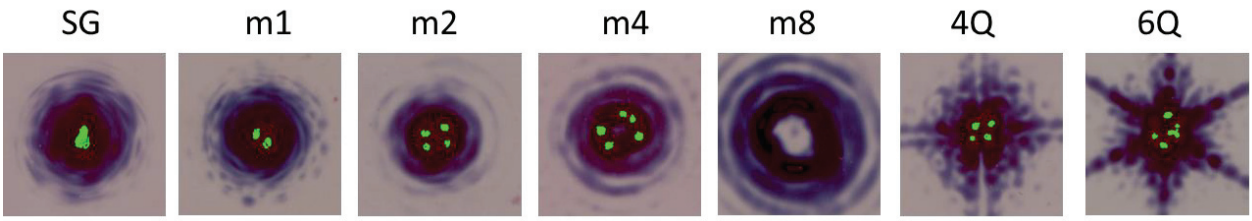

Figure 2.4.1. Filaments generated by different LG beams at the same energy. We measured the filaments and beam profiles using photosensitive paper positioned approximately 10 cm before the geometric focus. The external focusing lens had a focal length of $f = 5000$ mm. The incident pulse energy was 25 mJ, and the pulse duration was 500 fs.

References

1. L. Allen, M. W. Beijersbergen, R. J. C. Spreeuw, and J. P. Woerdman. Orbital angular momentum of light and the transformation of Laguerre-Gaussian laser modes. Phys. Rev. A **45**, 8185—8189 (1992).
2. B. Wetzel, C. Xie, P-A. Lacourt, J. M. Dudley, F. Courvoisier. Femtosecond laser fabrication of micro and nano-disks in single layer graphene using vortex Bessel beams. Applied Physics Letters **103**, 241111 (2013).
3. N. Jhajj, E. W. Rosenthal, R. Birnbaum, J. K. Wahlstrand, and H. M. Milchberg. Demonstration of long-lived high-power optical waveguides in air. Physical Review X **4**, 011027 (2014).
4. S. Fu, B. Mahieu, A. Mysyrowicz, and A. Houard. Femtosecond filamentation of optical vortices for the generation of optical air waveguides. Opt. Lett. **47**, 5228-5231 (2022).
5. A. Goffin, I. Larkin, A. Tartaro, A. Schweinsberg, A. Valenzuela, E. W. Rosenthal, and H. M. Milchberg. Optical Guiding in 50-Meter-Scale Air Waveguides. Phys. Rev. X **13**, 011006 (2023).
6. P. J. Skrodzki, T. Nutting, M. Burger, L. A. Finney, J. Nees, and I. Jovanovic. Guiding of Spectroscopic Signal with a Concatenated Filament-Driven Waveguide. in CLEO 2023, Technical Digest Series (Optica Publishing Group, 2023), paper ATh4I.4.
7. T. Wang, S. Bin Ali Reza, F. Buldt, P. Bassène, M. N'Gom. Structured light signal transmission through clouds. J. Appl. Phys. **133**, 043102 (2023).
8. Y. Hu, Z. Ye, H. Li, C. Lu, F. Chen, J. Wang, S. Pan, M. Zhang, J. Gao, and J. Wu. Generation of vortex N2 + lasing. Optica **10**, 682-687 (2023).
9. J. Gao, X. Zhang, Y. Wang, Y. Fang, Q. Lu, Z. Li, Y. Liu, C. Wu, Q. Gong, Y. Liu and H. Jiang. Structured air lasing of N2+. Commun Phys **6**, 97 (2023).
10. J. P. Gordon, H. J. Zeiger, and C. H. Townes. The Maser---New Type of Microwave Amplifier, Frequency Standard, and Spectrometer. Physical Review **99** , 1264-1274 (1955).
11. A. L. Schawlow and C. H. Townes. Infrared and Optical Masers. Phys. Rev. **112** (6), 1940-1949 (1958).
12. T. H. Maiman. Stimulated Optical Radiation in Ruby. Nature **187**, 493–494 (1960).
13. A. G. Fox, and T. Li. Resonant Modes in a Maser Interferometer. Bell. Syst. Tech. J. **40**, 453-488 (1961).
14. G. Goubau and F. Schwering. On the guided propagation of electromagnetic wave beams. IRE Transactions on Antennas and Propagation **9** (3), 248-256 (1961).
15. H. Kogelnik and T. Li. Laser Beams and Resonators. Appl. Opt. **5**, 1550-1567 (1966).
16. S. M. Barnett, L. Allen. Orbital angular momentum and nonparaxial light beams. Optics Communications, **110**, 5–6, 670-678 (1994).
17. G. Biener, A. Niv, V. Kleiner, and E. Hasman. Formation of helical beams by use of Pancharatnam–Berry phase optical elements. Opt. Lett. **27**, 1875-1877 (2002).
18. R. Feng, J. Qian, Y. Peng, Y. Li, W. Li, Y. Leng, R. Li. Terawatt-Class Few-Cycle Short-Wave Infrared Vortex Laser. Ultrafast Sci. 2023;**3**:0039.
19. A. Couairon, and A. Mysyrowicz. Femtosecond filamentation in transparent media. Phys. Rep. **441**, 47-189 (2007).

20. G. Fibich and N. Gavish. Critical power of collapsing vortices. Phys. Rev. A **77** (4), 045803 (2008).
21. P. Chernev and V. Petrov. Self-focusing of light pulses in the presence of normal group-velocity dispersion. Opt. Lett. **17**(3), 172–174 (1992).
22. S. A. Kozlov, A. A. Drozdov, S. Choudhary, M. A. Kniazev, and R. W. Boyd. Suppression of self-focusing for few-cycle pulses. J. Opt. Soc. Am. B **36**(10), G68–G77 (2019).
23. E. W. Rosenthal, J. P. Palastro, N. Jhajj, S. Zahedpour, J. K. Wahlstrand and H. M. Milchberg. Sensitivity of propagation and energy deposition in femtosecond filamentation to the nonlinear refractive index. J. Phys. B: At. Mol. Opt. Phys. **48** 094011 (2015).
24. W. Liu and S.L. Chin. Direct measurement of the critical power of femtosecond Ti:sapphire laser pulse in air. Opt. Express **13**, 5750-5755 (2005).
25. P. Polynkin, C. Ament, and J. V. Moloney. Self-focusing of ultraintense femtosecond optical vortices in air. Phys. Rev. Lett. **111**(2), 023901.
26. W. Liang, D. W. Li, J. W. Chang, T. T. Xi, L. F. Ji, D. M. Li, L. Z. Zhang, and Z. Q. Hao. Experimentally determined critical power for self-focusing of femtosecond vortex beams in air by fluorescence measurement. Opt. Express **31**(2), 1557–1566 (2023).
27. J. Yu, D. Mondelain, J. Kasparian, E. Salmon, S. Geffroy, C. Favre, V. Boutou, and J-P. Wolf. Sonographic probing of laser filaments in air. Appl. Opt. **42**, 7117-7120 (2003).
28. G. Point, E. Thouin, A. Mysyrowicz, and A. Houard. Energy deposition from focused terawatt laser pulses in air undergoing multifilamentation. Opt. Express **24**, 6271-6282 (2016).
29. O. Lahav, L. Levi, I. Orr, R. A. Nemirovsky, J. Nemirovsky, I. Kaminer, M. Segev, and O. Cohen. Long-lived waveguides and sound-wave generation by laser filamentation. Phys. Rev. A **90**, 021801(R) (2014).
30. D. Comtois, C. Y. Chien, A. Desparois, F. Génin, G. Jarry, T. W. Johnston, J.-C. Kieffer, B. L. Fontaine, F. Martin, R. Mawassi, H. Pépin, F. A. M. Rizk, and F. Vidal. Triggering and guiding leader discharges using a plasma channel created by an ultrashort laser pulse. Appl. Phys. Lett. **76**, 819–821 (2000).
31. S. Tzortzakis, B. Prade, M. Franco, A. Mysyrowicz, S. Hüller, and P. Mora. Femtosecond laser-guided electric discharge in air. Phys. Rev. E **64**, 057401 (2001).
32. A. Houard, P. Walch, T. Produit, V. Moreno, B. Mahieu, A. Sunjerga, C. Herkommer, A. Mostajabi, U. Andral, Y.-B. André, M. Lozano, L. Bizet, M. C. Schroeder, G. Schimmel, M. Moret, M. Stanley, W. A. Rison, O. Maurice, B. Esmiller, K. Michel, W. Haas, T. Metzger, M. Rubinstein, F. Rachidi, and J.-P. Wolf. Laser-guided lightning. Nat. Photonics **17**, 231 (2023).
33. P. Q. Elias, N. Severac, J. M. Luyssen, Y. B. André, I. Doudet, B. Wattellier, J. P. Tobeli, S. Albert, B. Mahieu, R. Bur, A. Mysyrowicz, and A. Houard. Improving supersonic flights with femtosecond laser filamentation, Science Advances **4**, eaau5239 (2018).
34. G. Dufour, B. Fornet, and F. Rogier. Numerical modeling of supersonic flow actuated by laser-induced plasma. Int. J. Aerodynamics **3**, 122 (2013).

Chapter 3

Controlling Femtosecond Filaments in the transverse plane— Generating Air Waveguides

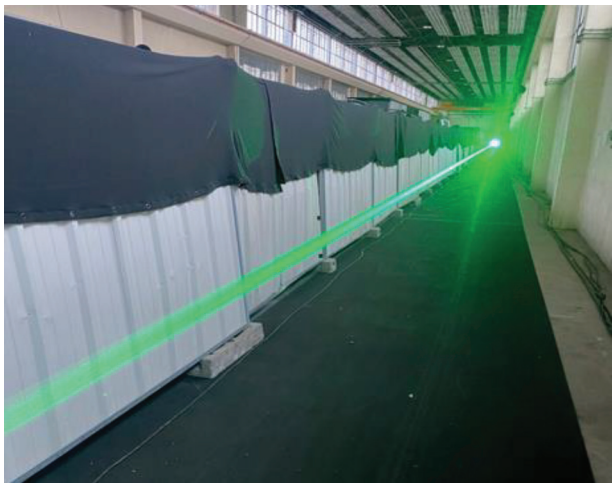

Figure 3.1. Photography of the LLR laser generating filaments over tens of meters.

As mentioned in the introduction, low-density channels play a crucial role in applications involving femtosecond filaments. These low-density channels can generate air waveguides [1-4], remotely focus laser beams [5], reduce breakdown threshold for high-voltage discharges, guide lightning [6-9], and clear clouds and fog for optical communications [10, 11], among other applications. In this chapter, we will focus on the application of air waveguides. First, I will present our work demonstrating for the first time the generation of air waveguides using vortex laser beams. Then I will explain how we overcome the focusing limitations by employing a multifocal phase mask to generate longer waveguides. Finally, I will show that we managed to produce air waveguides extending over tens of meters using only self-focusing femtosecond filaments, achieving long distance permanent air waveguides.

3.1 Principle of air waveguides

Air waveguides are structures similar to optical fibers formed in air. Therefore, before discussing air waveguides, I will recall the structure of optical fibers, taking the simplest step-index optical fiber as example.

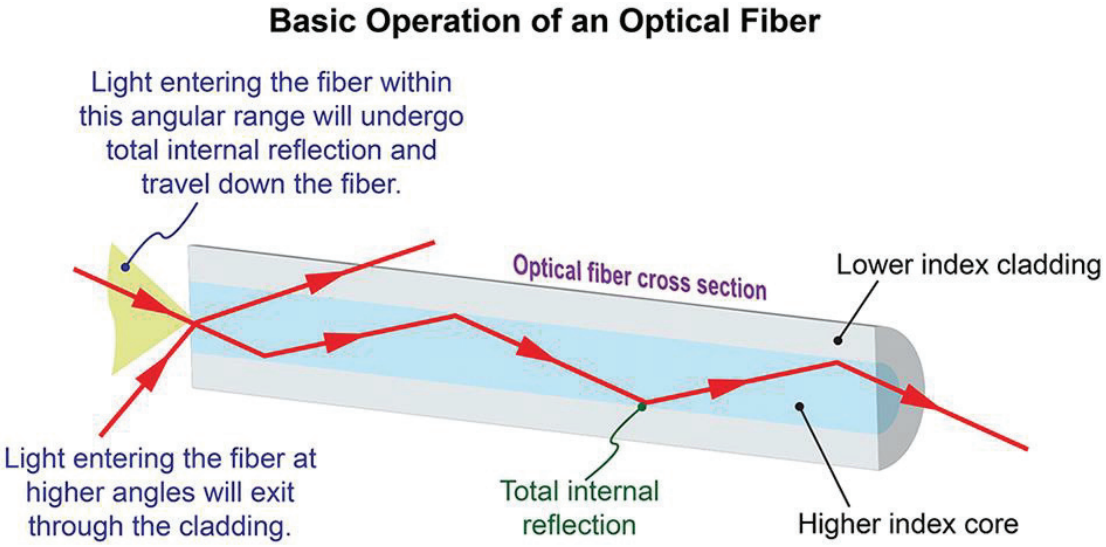

Figure 3.1.1. Basic structure of a step-Index optical fiber.

We can see that a step-index optical fiber consists of two parts: the cladding and the core. The cladding has a lower refractive index, while the core typically has a higher refractive index. Light incident at a certain angle will be continually reflected at the boundary due to the difference in refractive indices between the cladding and the core. A small part of the light will eventually be transmitted through the cladding resulting in a small energy loss. This is the most basic structure of optical fiber. New let us try to create this structure in the air.

Imagine a femtosecond laser beam with a hollow structure and far above the threshold intensity for air ionization, producing multiple filaments (plasmas) uniformly distributed in a ring-shaped structure. As mentioned in the introduction, each filament will heat the air, causing outward pressure waves (hydrodynamics) and changes in gas density within the filament on the microsecond timescale. After several hundred microseconds, these pressure waves will gradually merge and leave a relatively uniform low-density ring structure. In the center of this ring structure, due to the squeezing of the pressure waves, a high-density channel may also appear. This corresponds to the low-refractive-index cladding and high-refractive-index core in an optical fiber. We can guide optical signals through such a structure.

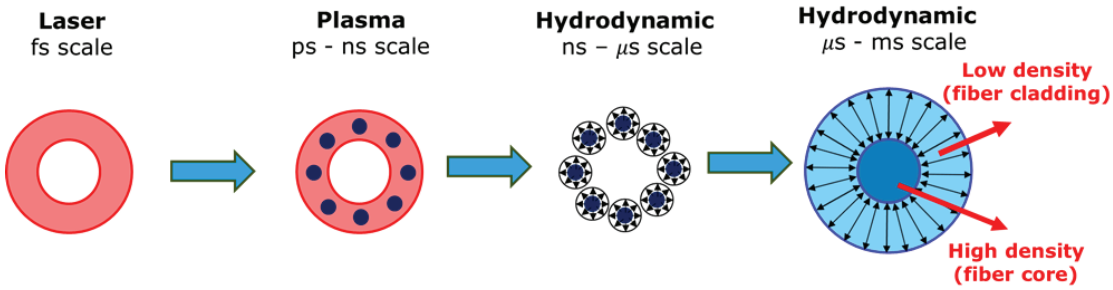

Figure 3.1.2. Schematic of air waveguide generation by filamentation.

Air waveguides have promising applications, particularly in the field of laser-induced breakdown spectroscopy (LIBS) [4], optical telecommunications, guiding of energy and remote sensing. For example, these waveguides can be utilized to guide energetic laser pulses or weak spectroscopic signals over long distances through the atmosphere. Additionally, the controlled air waveguides allow for precise targeting of specific regions in the atmosphere for scientific studies.

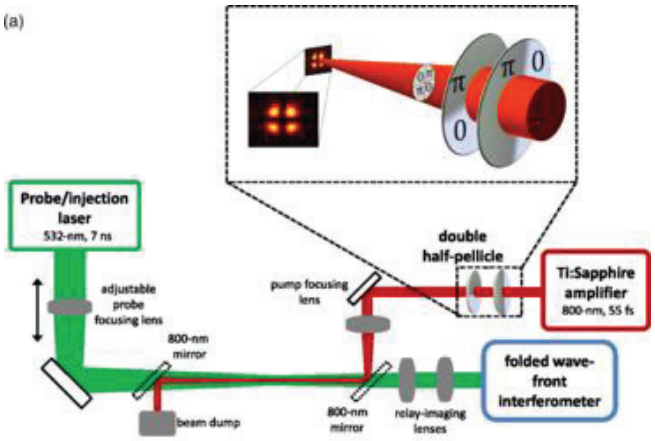

Figure 3.1.3. Schematic of the experimental setup used to demonstrate the first air waveguide. The authors used two phase plates to divide the beam into four parts and focused the laser beam to generate four filaments. From Jhajj *et al.* [1].

In 2014, Jhajj *et al.* first used four filaments to generate such air waveguides [1]. The authors used two phase plates to divide the beam into four parts, thereby producing four filaments evenly. The spacing between the four filaments was well controlled to produce specific hydrodynamic responses.

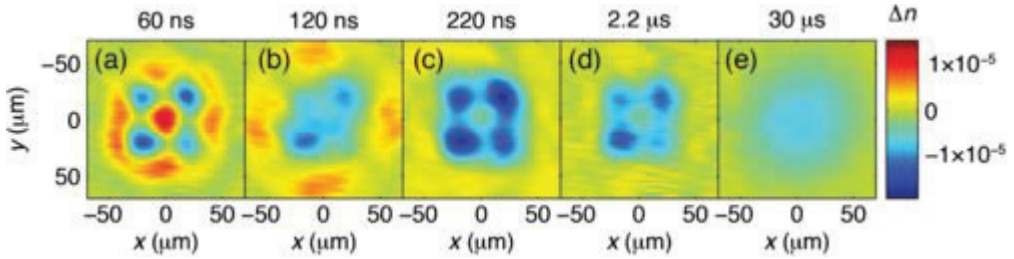

Figure 3.1.4. Air refractive index distribution recorded by interferometry in the case of a four-filament structure, showing two different waveguide structures. For short delay (a), an increase of the refractive index is generated on-axis by the superposition of the acoustic waves produced by the 4 filaments. It provides a guiding structure though the so-called acoustic waveguide mechanism. At longer delays ((c) and (d)), low-density channels from each filament form a "ring" around a center point with normal air density, which can last for several microseconds. This is referred to as the thermal guidance state. Adapted from Jhajj *et al.* [1].

In this article, the authors considered two waveguide modes: the acoustic waveguide and the thermal waveguide. The lifetime of the acoustic waveguide is only a few tens of nanoseconds while that of the thermal waveguide can reach several milliseconds. After irradiating the guiding structure with a 532nm Nd:YAG laser as a probing pulse, waveguide structures exceeding 70 cm length were demonstrated. This single-mode guidance achieved a peak efficiency exceeding 50%.

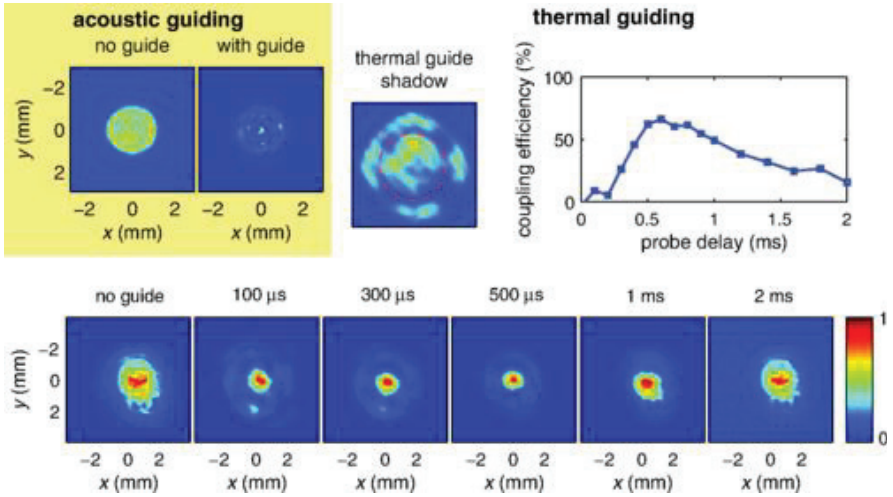

Figure 3.1.5. The guiding of 7 ns, 532 nm laser pulses in 70 cm long acoustic and thermal air waveguides generated by four filaments is demonstrated. The panel in the top left corner shows the probing beam, which is imaged after the filamentation region, with or without filaments (guide). The probe has a delay of 200 ns, corresponding to the acoustic guiding state. The effect of the thermal waveguide, indicated by shadows that can be seen in the image at the top center (red dashed circles represent the position of the low-density ring), is shown at the bottom row, where the probe beam is imaged after the air waveguides with and without filamentation. The relationship between coupling efficiency and injected pulse delay is shown in the top right. From Jhajj *et al.* [1].

3.2 Optical air waveguides generated by vortex femtosecond filaments

In the previous section, we mentioned that generating such air waveguides requires a beam with a ring-shaped transverse intensity distribution, leading to the formation of filaments distributed on a ring. It is evident that vortex beams of Laguerre-Gaussian modes can easily and naturally produce such filamentation regime. After conducting detailed studies on the filamentation of Laguerre-Gaussian beams, we attempted to achieve air waveguides using vortex femtosecond filaments.

I will first introduce the low-density channels generated by vortex femtosecond filaments produced by a low-power laser platform working at 100 Hz (Thales Alpha 100). Although we did not succeed in achieving air waveguides in this case, the stable beams provided important guidance for our experiments at higher energies. Then, I will discuss the vortex filaments generated by a TW laser platform (ENSTA mobile) and the low-density channels they produce. Finally, I will present the air waveguides generated using these low-density channels.

3.2.1 Low-density channels generated by vortex femtosecond filaments at low energy

We first studied filamentation of vortex beams with relatively low energies. We used the Alpha100 laser, delivering laser pulses with an energy of 11 mJ, a minimum pulse duration of 50 fs at a repetition rate of 100 Hz. The vortex phase is generated by introducing a vortex phase-plate in the beam path before the focusing lens. Phase plates with topological order of 1 and 2 were tested. We first observed the presence of filaments in the beam using photosensitive paper. This paper is not precisely calibrated but the intensity threshold for ablation is supposed to be close to the intensity threshold for plasma generation in air at 800 nm. Therefore, we can deduce the presence of plasma and filament by the color of the ablation. In the following images, the burned areas corresponding to ionization intensity were converted in green processed images. As shown in Figure.3.2.1, we found that we can obtain a quasi-continuous tubular plasma channel over several tens of centimeters around the geometrical focus of the beam.

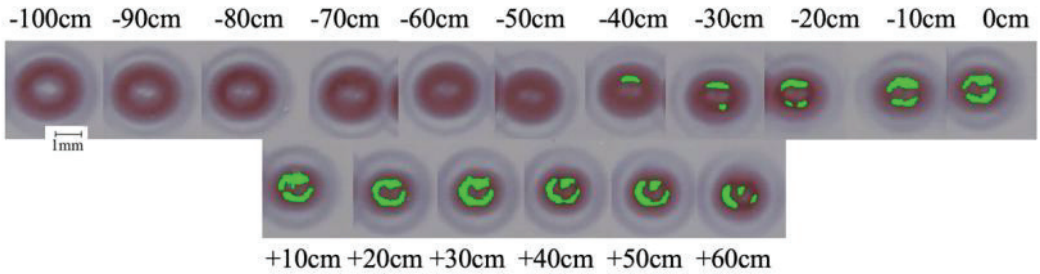

Figure 3.2.1. Impact of the laser vortex beam on photosensitive paper measured at different propagation distances z. The beam has an energy of 11 mJ, a pulse duration of 50 fs, a

topological order m = 2 and is focused by a lens f = 5 m, whose geometrical focus corresponds to position z = 0 cm.

We further investigated these tubular plasmas using other diagnostics. We measured the air density variation induced by the filaments after a delay of 1 µs using transverse interferometry. The principle of this diagnostic is detailed in the introduction.

In figure. 3.2.2, we compare the low-density channel produced by the vortex beam described in figure. 3.2.1 with a Gaussian beam with the same energy, pulse duration and diameter. We can see that the low-density channel produced by the vortex beam presents two channels, while the Gaussian beam generated a single large channel.

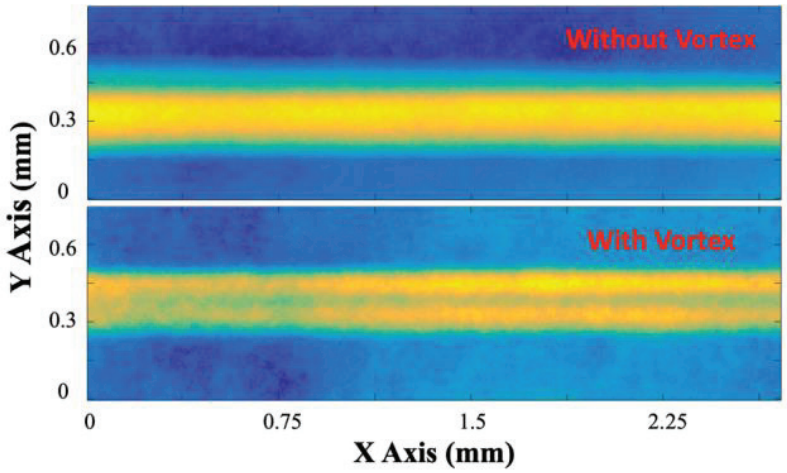

Figure 3.2.2. Comparison of the low-density air channels generated by a laser beam with 11 mJ, 50 fs focused by a 5 m focusing lens, with (bottom) and without the vortex plate (top). We used a wavefront detection system to study apparition of the low-density air channels 1 µs after filament formation.

We found that with a laser energy of 11 mJ/shot, we can create a significant air density variation around the focus, but the length of the filament was limited to a few centimeters, or tens of centimeters. Therefore, to create a meter-scale air waveguide, we decided to use a laser with higher energy.

3.2.2 Vortex femtosecond filaments generated by a TW laser system

This section is taken from my article [Optics Letters **47**, 5228 (2022)]. To generate a strong low-density channel over a meter with a vortex femtosecond laser, we had to use a laser with higher input energy than the Alpha 100 laser. So, we chose the ENSTAmobile laser that can deliver laser pulses at 800 nm with 200 mJ energy, 50 fs duration, with a diameter of 25 mm FWHM at a repetition rate of 10 Hz. In the previous chapter, we found that using the full pupil of the laser beam could destroy the hollow structure of the vortex beam around the focus. Therefore, we had to limit the diameter of the laser beam on the vortex plate to 1 cm using an iris, resulting in a super-Gaussian profile with an energy of 25 mJ. The pulse duration was adjusted between 50 fs and 2 ps by detuning the grating compressor of the laser to add a

positive chirp. The beam was then focused by a convex lens with a focal length of f = 4 m, and a vortex plate with topological order m = 4 from Holo/Or was inserted on the beam path to produce the helical phase pattern.

We first characterized the propagation of the focused optical vortices at low energy (E ≈ µJ) using a CMOS camera and at high energy (E = 25 mJ) using photosensitive paper. Figure.3.2.3(a) presents the evolution of the beam profile along the propagation axis z measured with photosensitive paper. The green color indicates the burned area of the paper, corresponding to a filament laser intensity. For a pulse with a duration τ = 200 fs (P = 160 GW ≈ 16 Pcr), we observe between 3 and 6 distinct filaments organized in a circle over a distance of 1.5 m around the geometrical focus. The diameter of this ionized circle matches well the diameter of the low intensity vortex beam up to z = −25 cm and then becomes slightly smaller over 70 cm after the focus [see figure.3.2.3(d)]. This contraction might be explained by Kerr self-focusing appearing at high intensity. When the initial laser pulse duration τ is chirped from 200 to 800 fs (P = 36 GW), the number and the length of the filaments produced are both decreased.

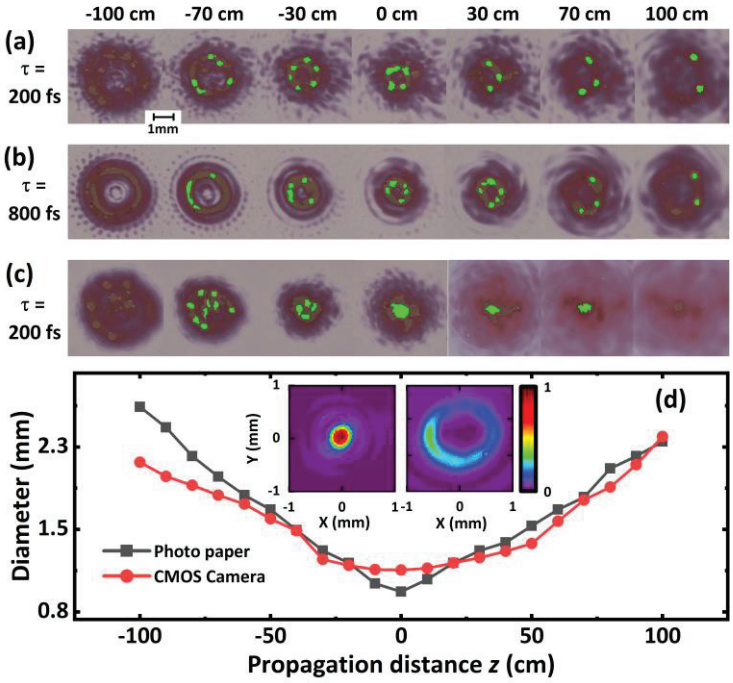

Figure 3.2.3. Beam profile measured as a function of the propagation distance z by impact on photosensitive paper for a vortex beam with 25-mJ energy and a duration of (a) 200 fs and (b) 800 fs and (c) for a super-Gaussian beam with duration 200 fs. The linear focus of the lens is at z = 0. (d) Diameter of the ionized ring measured at high intensity with τ = 200 fs (black curve) and diameter of the intensity ring measured at low intensity by a CMOS camera (red curve) as a function of z. The inset compares the low intensity profile measured at the focus for a super-Gaussian and a vortex beam.

As shown by [12-13], the formation of long-lived low-density channels resulting from filamentation is directly related to the density of energy deposited inside the filament through

ionization and Raman absorption. To characterize the deposition of energy by the vortex filament, we used a broadband microphone GRAS Model 46BH ¼" placed on the side of the beam at a distance of 20 mm. This microphone measures the transverse pressure wave generated by the filament that is proportional to the density of deposited energy in the filaments. The results are presented in Fig. 3.2.4(a) for a vortex beam and for a super-Gaussian beam with the same input energy. For a vortex beam with 200 fs duration, a quasi-constant signal is measured over 1 m from z = −90 to +25 cm. The super-Gaussian beam shows a signal 5 times higher with a peak over 30 cm, typical from a regime of superfilamentation [14].

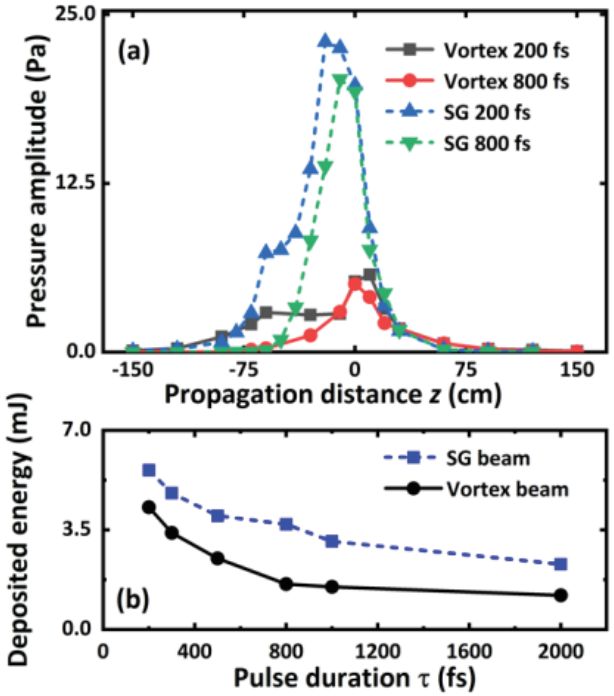

Figure 3.2.4. (a) Amplitude of the lateral acoustic wave measured by the microphone 20 mm away from the beam for the 25-mJ laser pulse. (b) Energy deposited in the filament for an input pulse energy of 25 mJ for a super-Gaussian beam (blue curve) and a vortex (m = 4) beam (black curve) as a function of the laser pulse duration.

The total energy deposition in the vortex filaments was measured as a function of the laser input pulse duration τ [Fig. 3.2.4(b)]. We can see that this energy deposition is decreased by a factor of 2 when the laser pulse duration is increased from 200 fs to 800 fs and then remains quasi constant, around 1.3 mJ, for longer pulse durations. We note that the total energy deposited with the super-Gaussian beam is only 30% higher than the vortex one, while the ratio of their acoustic signals is approximately 3 to 4. Considering that the shape of the energy deposition follows the measured pressure wave presented in Fig. 3.2.4(a), we can estimate the maximum lineic energy deposition to be 95 µJ/cm for the super-Gaussian beam and 52 µJ/cm for the vortex beam. Therefore, despite the much lower intensity generated at the focus by the vortex beam, the energy deposition of the vortex beam is comparable to that produced by the super-Gaussian beam, taking into account its larger mode.

3.2.3 Structured air channels generated by vortex femtosecond optical filaments for air waveguides

After generating and studying these hollow structured femtosecond filaments, we investigate the air structures produced by these filaments using the interferometric detection system.

The temporal evolution of the vortex filaments after plasma recombination was characterized using transverse interferometry by means of a probe laser with 10-µs duration at a wavelength of 640 nm, whose phase profile was analyzed by a Phasics SID4HR wavefront sensor (see Ref. [15] for a description of the setup). The plane $z = 0$ containing the propagation axis is imaged on the sensor to get the profile of the gas density in this plane. Figure 3.2.5(a) and (b) present the phase shift measured on the vortex filament after 1 µs and 500 µs. At 1 µs, one can see 4–5 distinct low-density channels generated by filaments with a ~100 µm size. After 500 µs, these filaments broaden to form two low-density channels with a 300 µm width. We note that the magnitudes of the phase variations measured with a 200 fs and 800 fs pulse were very similar. This can be explained by the mechanism of intensity clamping inside the filament. The phase shift profile integrated along z is also plotted in Fig. 3.2.5(c) and (d) for delays of 1 µs and 500 µs, respectively. The phase shift produced by the vortex beam is compared with that produced by the super-Gaussian beam. One can see that the phase difference is only 50% higher for the super-Gaussian case with a Gaussian density profile, while the vortex generates a hollow profile.

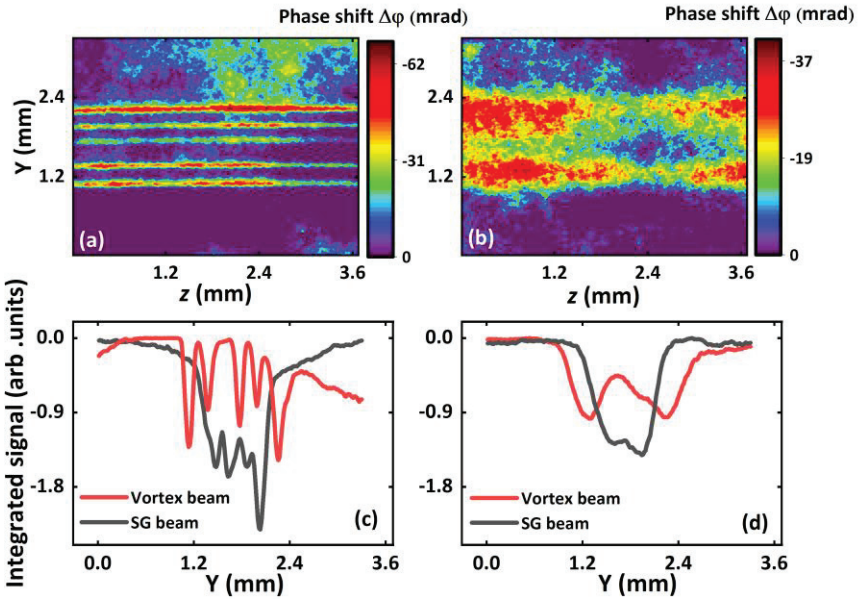

Figure 3.2.5. Transverse image of the filaments produced by the vortex beam with 800-fs duration measured (a) 1 µs and (b) 500 µs after the filament formation at position $z = -30$ cm obtained by interferometry. Phase shift Δϕ integrated along z for a delay of (c) 1 µs and (d) 500 µs for a super-Gaussian beam (black curve) and a vortex beam (red curve).

We assume an axial symmetry along the z-axis for the air density channel generated after a long delay. By employing Abel inversion, we can calculate the corresponding air density modulation after 500 µs. For the detailed computational procedures, please refer to [16]. The computed results are depicted in Figure 3.2.6. As observed, the air density profile generated by the vortex beam exhibits a channel with density higher than that of ambient air at the center, corresponding to the core structure of a fiber. Surrounding this core, there exists a region with a density lower than that of ambient air, analogous to the cladding in a fiber. This elucidates why we can employ this structure for guidance.

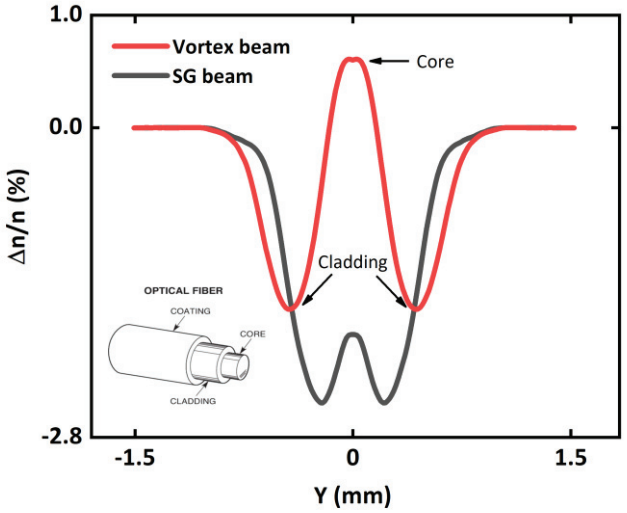

Figure 3.2.6. Air density variations corresponding to the phase measurement presented in Figure 3.2.5. To illustrate the structure of an optical fiber, a simplified step-index fiber structure was inserted in the bottom left corner.

3.2.4 Air waveguide generated by vortex optical filaments

To test the ability of tubular filaments to act as an optical guide, we built the setup shown in Fig. 3.2.7. A probe beam at 532 nm with µJ-level energy and 10 ns pulse duration was delivered by a Yb:YAG laser, synchronized with the Ti:Sapphire fs laser system. The delay between the two lasers could be controlled using a digital delay generator. A dichroic mirror was used to combine the two beams and glass color filters were used to block the 800 nm beam after the filament. The profile of the probe beam at 532 nm was imaged by a CMOS camera placed 4 m after the geometrical focus of the beams. Similar waveguides were first demonstrated by Jhaj *et al.* using an array of four filaments [1].

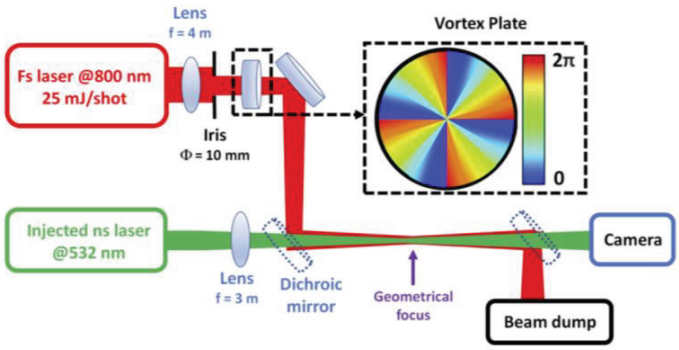

Figure 3.2.7. Experimental setup used for the optical waveguide experiment.

The beam profile of the probe laser in the absence of the femtosecond laser is presented in Fig. 3.2.9(a), with a Gaussian profile and a FWHM of 9 mm. The output profile of the 532-nm beam in the presence of the vortex beam is then presented for different delays Δt between the fs vortex beam and the ns probe beam, ranging from 2 μs to 2 ms. For delays of a few μs, the probe beam is perturbed by the vortex beam, but no guiding is observed. However, for Δt ranging from 100 μs to 1 ms, an intense spot with a width of 1.5 mm can be observed in the beam profile, signature of a laser guiding effect. We define the guided energy as the percentage of laser energy in a circle of 5-mm diameter, corresponding to the guided mode [see red dotted circle in Fig. 3.2.9 (c). The percentage of guided energy in this mode is plotted in Fig. 3.2.9 (f) as a function of the probe delay Δt and in Fig. 3.2.9 (g) as a function of the pulse duration of the vortex beam. The guiding is maximum for a delay of 500 μs and lasts for a millisecond, similar to the results of Ref. [1] with an array of four filaments. Surprisingly, the guiding efficiency does not depend on the vortex pulse duration (or peak power). This result is in agreement with the interferometric measurements made for different laser pulse durations, as shown in Fig. 3.2.8.

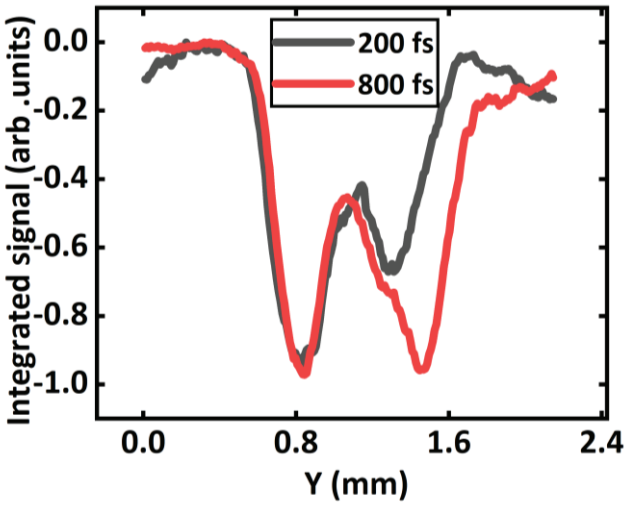

Figure 3.2.8. Phase shift Δϕ integrated along z generated by low-density channels produced with different pulse durations. The black curve represents the results for 200 fs, while the red curve represents the results for 800 fs.

Indeed, as shown in Fig. 3.2.4(a), increasing the peak power of the vortex beamextends the filaments toward the laser, but will not modify the guiding part around and after the focus. In addition, an advantage compared with the waveguide produced by four filaments is the scalability of the vortex, since the diameter of the guide can be increased with the topological order of the waveplate (or by decreasing the beam numerical aperture), while adjusting the input laser energy.

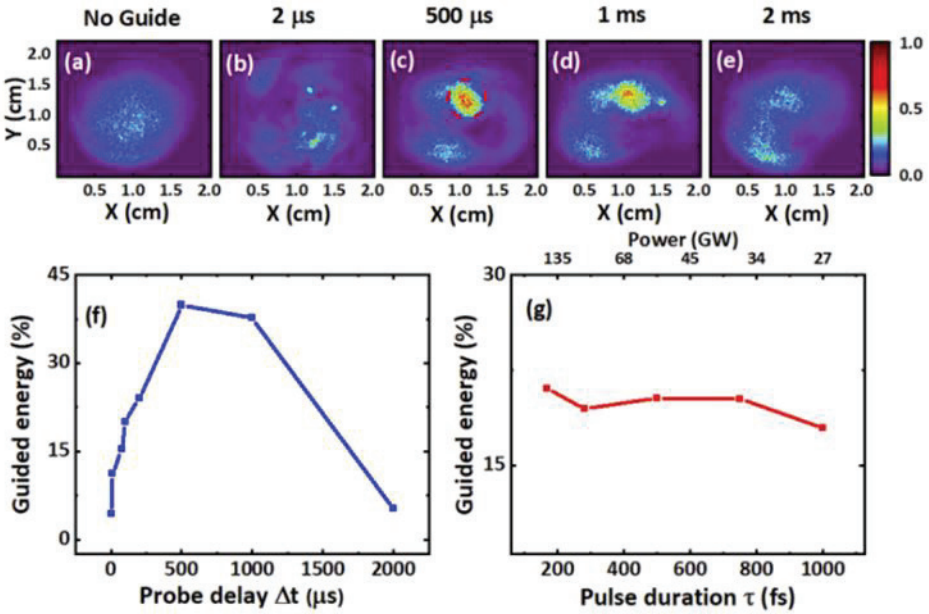

Figure 3.2.9. Far-field profile of the probe beam measured 4 m after the geometrical focus (a) in the absence of vortex beam, and in the presence of vortex beam for delays of (b) 1 µs, (c) 500 µs, (d) 1 ms, and (e) 2 ms. (f) Percentage of guided energy as a function of the delay Δt between the two pulses, and (g) as a function of the pulse duration τ of the input vortex pulse for a delay of 100 µs.

3.3 Multifocal phase mask extended air waveguides

In the previous section, we demonstrated a very simple method to generate a ring-shaped filamentary beam and thereby created an air waveguide extending 1.5 meters. In this work, we found that the efficiency of the air waveguide seems to be insensitive to the peak power of the incident pulses. This suggests that triggering such an air waveguide may not require very large energy deposition. Therefore, we sought for a way to extend the filamentation axially with the same laser energy, in order to generate longer air waveguides.

Methods for extending filamentation axially without increasing laser energy have been explored for twenty years. As early as 2003, Tzortzakis *et al.* proposed to divide the beam into two parts to generate two aligned filaments and then stringing these filaments together through nonlinear interaction [17]. This concatenated filamentation has been used to guide discharges over longer distances [18,19]. Alternatively, focusing the beam at different positions with a "broken lens" can generate a series of concatenated filaments [20].

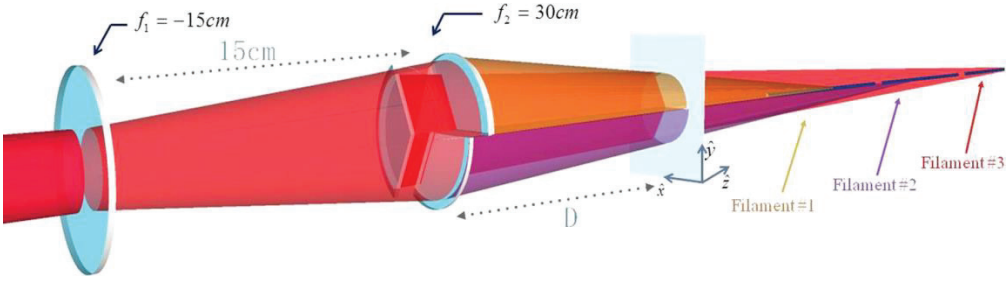

Figure 3.3.1. Method to generate concatenated filaments using a "broken lens." The beam is first expanded with a -15 cm lens, then a 30 cm focusing lens divided into three segments focus the beam at different positions, creating concatenated filaments (from [20]).

However, these methods require complex focusing optical devices and delay control systems. Additionally, they can hinder complex filament structures, such as those generated by vortex laser pulses. With the continuous advancement of diffractive optics, we can now utilize specially designed Multi-Focus Diffractive Optical Elements (DOE). These components allow to focus the same beam at different focal positions with a uniform spacing and energy distribution along the axial direction, as shown in Figure 3.3.2. This technological development provides us with a flexible and efficient approach to create complex focusing structures, thus enabling the generation of automatically aligned multi-focus filaments.

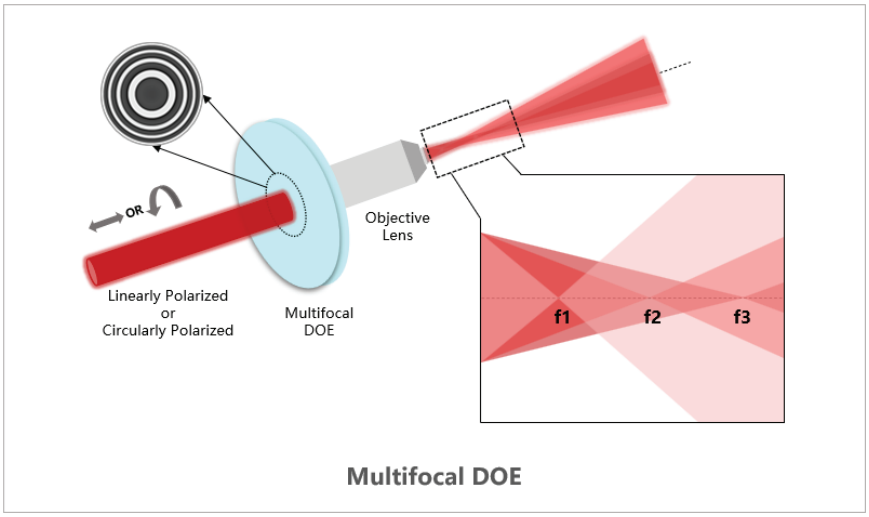

Figure 3.3.2. Principle of the multi-focus phase plate (from [21]).

3.3.1 Multifocal phase mask (MPM) generated filaments

The principle of generating filaments using MPM is illustrated in Figure 3.2.11. A focused laser beam is diffracted by a diffractive optical element (Holo/Or model TF-014-800). This allows the incident beam to be focused at three focal distances along the propagation axis, with equal laser energy [22], where the focal positions depend on the external focusing conditions. Table 3.3.1. presents the relative distances of the multi-focal points produced by different external focusing. Here, f1, f2, f3 refer to the first, second, and third focal point distances from the external focusing geometric focus position. It can be observed that the larger the focal length of external focusing, the greater is the difference in focal lengths between different focal points.

External focusing focal length (m)	F1(m)	F2(m)	F3(m)	F1-F3 (m)
1	-0.09	0	0.1	0.19
1.5	-0.18	0	0.24	0.42
2	-0.37	0	0.43	0.8
2.5	-0.5	0	0.7	1.2
3	-0.7	0	1.1	1.8
4	-1	0	2.2	3.2
5	-1.5	0	4.1	5.6

Table 3.3.1. Focus positions produced by a multi-focus phase mask under different external focusing.

We now consider the process of filament generation. A filament is generated at each focus during each focusing event. Due to the finite length of the filaments, we should control the external focusing and the laser input energy to make these filaments merge, thereby

producing a continuous filamentation. In the bottom right corner of Figure 3.3.3, we provide an image of the beam after the multi-focal phase mask using photosensitive paper. We can see that the intensity distribution of the beam consists of several concentric rings. By using an iris to control the input diameter of the beam, we found that the different rings focus at different positions along *z*.

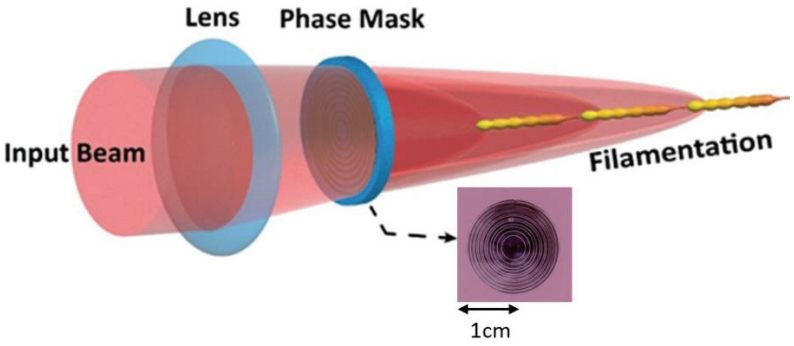

Figure 3.3.3. Setup for generating extended laser filamentation.

To study the intensity distribution and the wavefront phase of the beam more accurately, we used the wavefront sensor to detect both the intensity and phase distributions of the beam. Figure 3.3.4 shows the measured intensity and phase maps of the beam exiting the phase plate. Due to the size limitation of the detector, we only measured a quarter of the beam. Figure 3.3.4(a) presents the intensity distribution of the beam, while (b) shows the phase distribution of the beam.

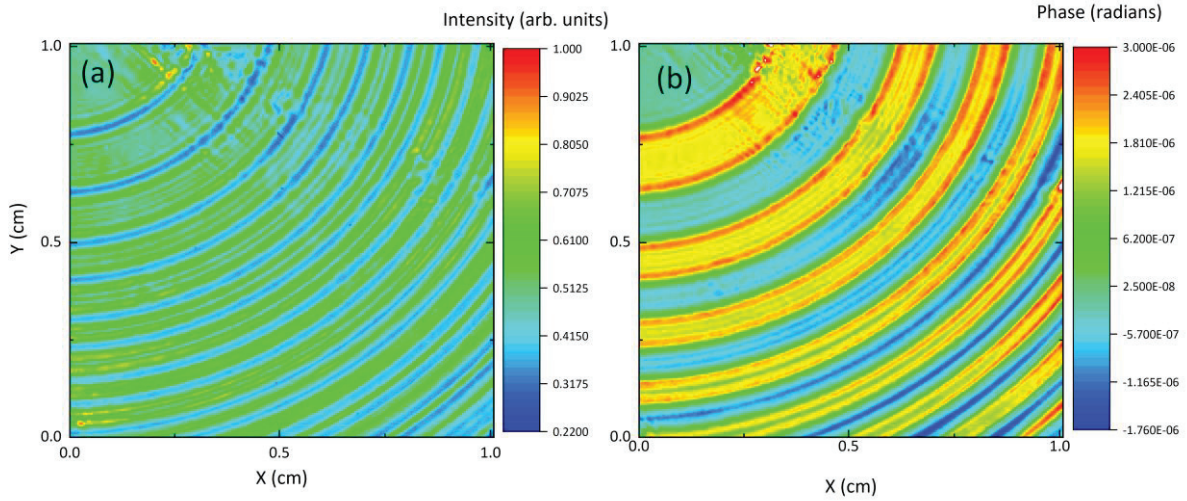

Figure 3.3.4. Intensity and phase distributions of the beam measured by an SID4 wavefront sensor after the multi-focal phase plate. (a) shows the intensity distribution, while (b) displays the phase distribution.

From Figure 3.3.4 (a), we can observe that the beam is composed of several concentric circles, consistent with the results obtained from the photosensitive paper. In the phase

measurement, we can see that the beam is composed of three phase components: the zero-phase component represented by the central circle (green), the negative phase components (blue) and the positive phase components (red and yellow), corresponding to the parts of the beam focused at the central focal points (the second focal point), the first focal point, and the third focal point, respectively. However, even though our measurements were made just after the phase plate, the beam exhibits significant diffraction effect, as indicated by the appearance of red diffraction rings near the yellow positive phase component. In Figure 3.3.5, the phase distribution is represented as a function of the radius. It is evident from this result that there are distinct diffraction patterns and the three different phase components as mentioned earlier.

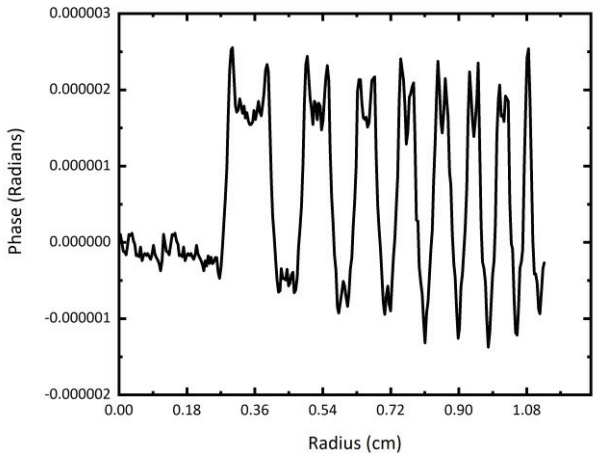

Figure 3.3.5. Measured phase distribution measured after the multi-focal phase plate aas a function of the beam radius.

To study the characteristics of the filaments generated by the multi-focal phase mask, we used a 3-meter lens to produce filaments in air. First, we imaged the beam fluence and the filaments distribution at different z-axis positions using photosensitive paper (Figure 3.3.6).

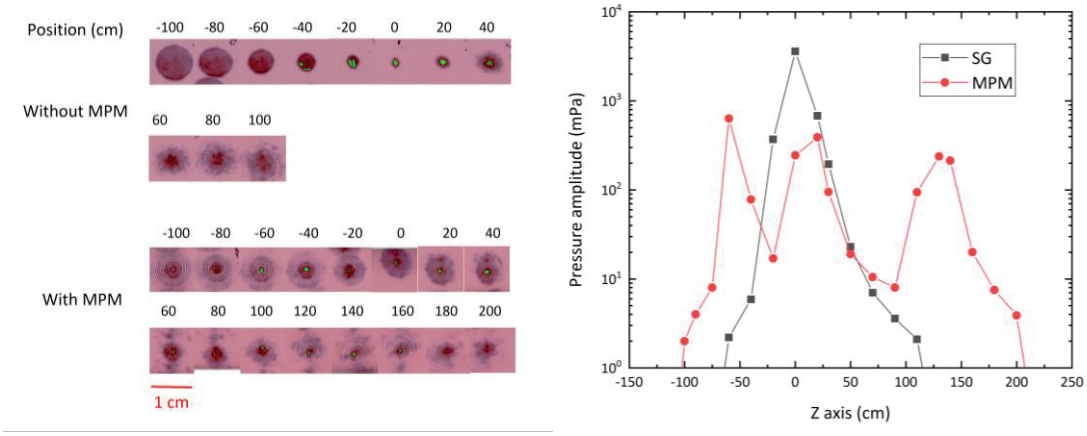

Figure 3.3.6. Filaments generated by the multi-focal phase mask. Left: Impact of the laser beam with and without the multifocal phase mask (MPM) on photosensitive paper measured at different propagation distances *z*. Right: Amplitude of the transverse acoustic wave measured by a microphone 30 mm away from the laser filament axis. The black line represents the results generated using a super-Gaussian beam, the red line represents the results generated using the multi-focal phase mask. Laser energy is 50 mJ, pulse duration is 500 fs, and external focusing is performed with a 3-meter lens.

Without using the multi-focal phase mask, filamentation is observed from z = -40 cm to z = 40 cm. However, upon adding the multi-focal phase mask, we observe continuous filamentation on the photosensitive paper from -60 cm to 160 cm. The length of the filaments is increased by nearly a factor three. The results from the acoustic signal agree with those observed with the photosensitive paper.

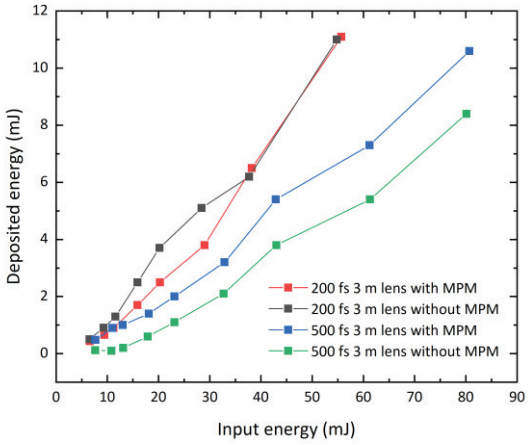

Figure 3.3.7. Dependence of the deposited energy in filaments generated with the MPM and without MPM for different input pulse duration. The red (with MPM) and black lines (without MPM) represent results obtained with 200 fs input pulses, while the blue (with MPM) and green lines (without MPM) represent results obtained with 500 fs input pulses.

Subsequently, we measured the deposited energy of filaments generated by multi-focal phase masks for two different pulse durations. We observed an increase in the deposited energy with the use of multi-focal phase mask with the case of 500 fs. In particular, in the low-energy region (below 15 mJ), using multi-focal phase masks resulted in a doubling of the energy deposition. However, when we used a pulse duration of 200 fs, we did not observe this increased energy deposition with the MPM. This may be due to the fact that at high peak power, the length of the filaments generated by the multi-focal phase mask and those generated by the regular super-Gaussian beam became similar, eventually resulting in the same level of multiphoton ionization and Raman absorption.

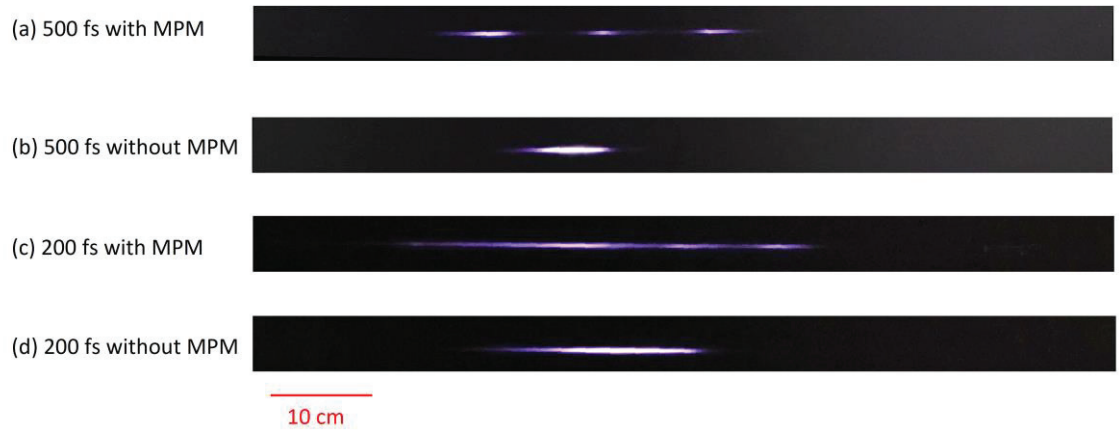

Figure 3.3.8. Measurement of the plasma luminescence from filaments generated by different pulse durations using a commercial camera. (a) and (b) shows the cases with and without the MPM for an incident pulse duration of 500 fs, respectively. (c) and (d) shows the cases with and without the MPM for an incident pulse duration of 200 fs, respectively. The input pulse energy was 55 mJ, and an external focusing of a 1 m lens was chosen. All images are single-shot measurements.

To understand the improvement in deposited energy, we measured the plasma luminescence for two different input pulse durations of 500 fs and 200 fs, using a commercial camera, as shown in Figure 3.3.8. With long pulses (500 fs), the filament length is extended three times by the MPM. However, when we used 200 fs pulses, the MPM only extended the filament length by 1.5 times. Considering that dispersed focusing reduces plasma density (as confirmed by acoustic signals shown in Figure 3.3.6), when the filament length is not significantly extended by the MPM, the number of plasmas generated by the MPM is not significantly increased. This may explain why we did not observe any increase in energy deposition with short pulses. Due to risks of damaging the phase plate, we did not test shorter pulse durations.

3.3.2 Optimization of air waveguides with multifocal phase masks

Using a multifocal phase mask (MPM) can significantly extend the length of filaments, which seems to imply that this method can also significantly improve any atmospheric applications sensitive to filament length, such as the guiding of high-voltage discharges [6], air waveguides [1], optical communication through fog [10] and cloud layers [11], satellite communication [23] and plasma waveguides for microwaves [24]. We will discuss the guiding of high-voltage discharges in detail in Chapter 4. In this section, we will demonstrate the improvement in air waveguide using MPM.

As mentioned in the previous chapter, a larger focal length for the external focusing will increase the distances between the different focal points. Considering our laser energy and the spatial constraints of our laboratory, we chose a four-meter lens for the air waveguide experiment.

First, we need to verify whether satisfactory air waveguide structures can be generated when the vortex beam and the multifocal phase mask work together. Obviously, for such a satisfactory air waveguide, there are two conditions: first, it should be able to produce consistently continuous filaments, and second, it should ensure that the vortex beam maintains a sufficiently large inner diameter throughout. We used an input energy of 92 mJ, an input pulse duration of 500 fs, and an M8 vortex phase plate to ensure a sufficiently large filament structure inner diameter. First, we scanned the filament structure using photosensitive paper. As shown in Figure 3.3.9, in the absence of a multifocal phase mask, we observed the phase structure of a hollow vortex femtosecond filament extending over 2 meters. With the addition of the multifocal phase mask, this hollow femtosecond filament was greatly extended, and we observed filamentation structures over at least 4.5 meters. Furthermore, although the inner diameter of this hollow structure fluctuated, it remained open along the propagation axis, creating favorable conditions to generate air waveguides.

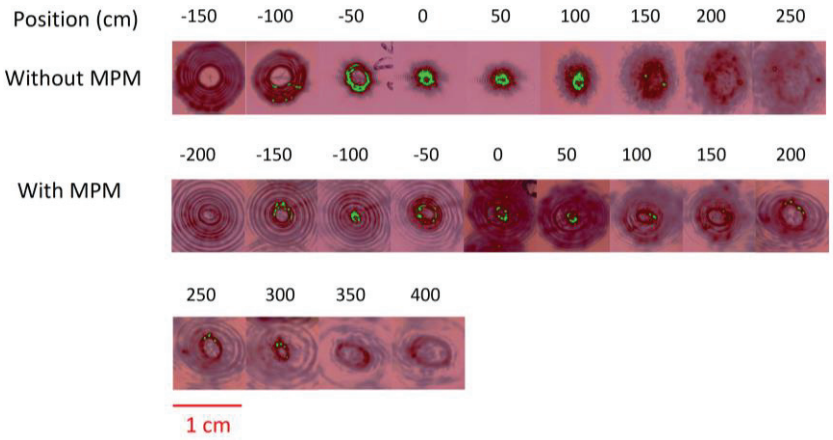

Figure 3.3.9. Filaments generated by the vortex beam, measured using photosensitive paper. The upper part shows the filaments produced without the multifocal phase mask; the lower part shows the filaments produced with the multifocal phase mask. The laser energy was 92 mJ, the pulse duration was 500 fs, and we used a 4-meter lens for external focusing.

Next, we tested the extended air waveguide produced with the MPM. The setup is illustrated in Figure 3.3.10. An 800 nm pump beam with a pulse duration of 500 fs and energy of 92 mJ was focused using a 4-meter lens. The beam then passed through a vortex phase plate with m = 8 and the multifocal phase mask to create the extended cylindrical filamentation area. A 532 nm Yb:YAG laser pulse with an energy in the μJ-level and a pulse duration of 10 nanoseconds in focused at the beginning of the filaments using a f = 3 m lens. The profile of the 532-nm probing beam was captured by a CMOS camera located 10 meters behind the lens, with a color filter to block the light from the fs laser at 800-nm. This setup is similar to the one depicted in Figure 3.2.7, with the addition of the multifocal phase mask in the pump beam path.

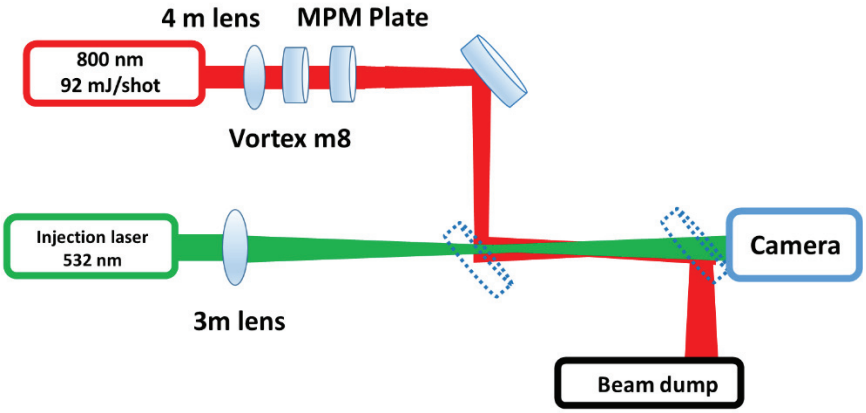

Figure 3.3.10. Experimental setup for extending the air waveguide using a multifocal phase mask.

In the previous studies, we determined that the efficiency of this air waveguide is highest at a delay of 500 µs after the formation of the filament. Therefore, in Figure 3.3.11. (c-d) we present the profile of the probing pulse at the output of the air waveguide sent 500 µs after the generation of the filament, as captured by the CMOS camera. One can see that the diameter of the guided beam measured 6 meters after the lens geometrical focus is almost two times smaller in the case of the extended vortex beam (3.2 mm width instead of 6.4 mm). This corresponds to the diffraction of a guided beam with a diameter of 0.8 mm FWHM going out of the waveguide at z = 150 cm without MPM and at z = 350 cm with the MPM. The air waveguide is therefore extended by 2 m in the presence of the MPM.

In Figure 3.3.1 we present the acoustic signals produced by the normal vortex filaments and the extended vortex filaments 1. For the normal vortex filaments, acoustic signals were observed between z = -150 cm and z = 200 cm. In contrast, with the extension of the vortex filaments, the plasma spans from z = -225 cm to z = 450 cm, which corresponds to the observed extension of the air waveguide length.

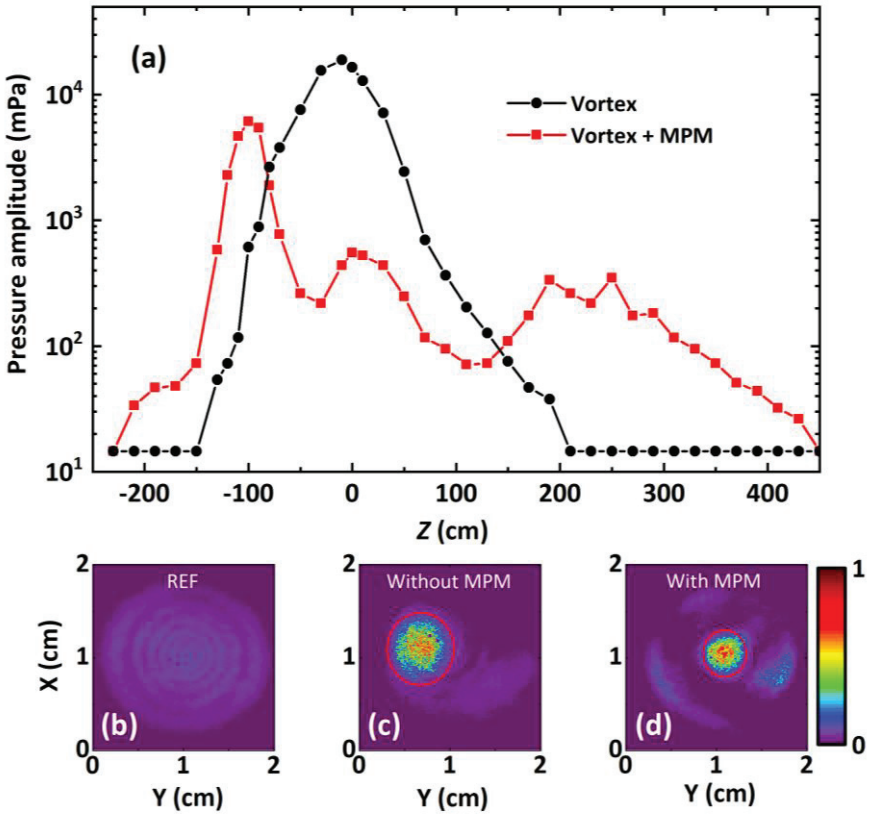

Figure 3.3.11. Air waveguide produced by the extended vortex filaments. (a) Amplitude of the transverse acoustic wave measured by a microphone 30 mm away from the laser filament axis. The laser beam has an energy of 92 mJ, a duration of 500 fs and a vortex topological charge m = 8. (b-d) profile of the probe beam measured at z = 10 m at the output of the air waveguide, in the absence of filament (b), in the presence of filaments generated by the vortex phase-plate (c), and in the presence of filaments generated by the vortex phase and the MPM (d). The probe beam is sent 500 µs after the fs laser pulse.

3.4 Long permanent air waveguide produced by filamentation of a collimated Laguerre-Gauss beam

In this section, we will demonstrate the generation of a 20 m long permanent air waveguide using the cumulative effect of low-density channels produced by laser filaments.

3.4.1 Cumulative effect of low-density channels produced by laser filaments

Let us revisit the physical process of low-density channels creation by laser filaments in air. If the density change caused by the filamentation in air is high enough, the time required to dissipate this density change will be sufficiently long to produce a permanent effect. In Figure 3.4.1, we show the effect of a nanosecond laser beam, used as a probe beam, propagating along the axis of the filament at different times after the filament has been generated.

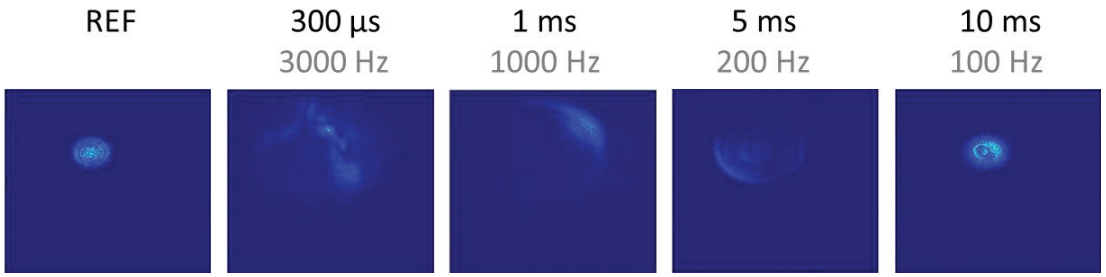

Figure 3.4.1. Beam profiles of the probe beam passing through the low-density channel at different time delays after filamentation. A nanosecond (ns) probe beam is used to propagate along the axis of the filament at different time delays. These different time delays correspond to the intervals between high-repetition-rate laser pulses. We used a super-Gaussian beam with 90 mJ, 10 Hz, and 800 fs, focused in air by an $f = 4000$ mm lens to produce the filament.

It can be observed that even at a 10 ms delay after the filament generation, the beam profile of the ns probe beam is still affected by the low-density channel produced by the previous filament. A 10 ms delay corresponds to the time interval between pulses of a 100 Hz laser. This means that the pulses of a 100 Hz laser will be influenced by the low-density channel produced by the filamentation of the previous pulse. Therefore, when the repetition rate of the laser exceeds 100 Hz, the impact of this integrated effect should be considered.

In 2021, our group conducted a detailed study of this cumulative effect [15]. As shown in Figure 3.4.2, (a) illustrates the differences in the low-density channels produced by lasers with different repetition rates under the same conditions, as measured and simulated. It can be observed that higher repetition rates result in greater changes in air density. (b) shows the profile of the low-density channel created by laser filaments generated at 100 Hz. It can be seen that the low-density channel produced by the 100 Hz laser has stabilized in the form of a mm size low density channel. This indicates the possibility of creating a permanent air waveguide (steady air waveguide).

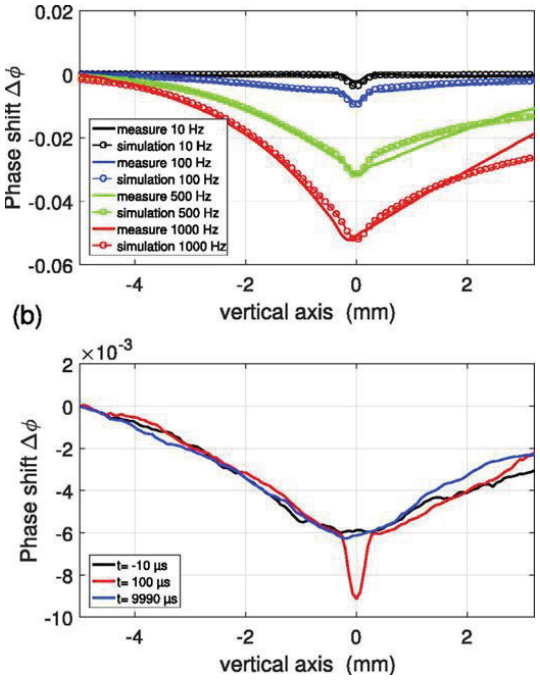

Figure 3.4.2. Effect of the laser repetition rate on low-density channels. (a) Low-density channels produced by lasers with different repetition rates. (b) Low-density channel produced by a 100 Hz repetition rate laser measured at different delay times (from [15]).

3.4.2 Characteristics of filamentation produced by the LLR laser

To realize the application of this cumulative effect in generation of air waveguides, we need to use a laser with a higher repetition rate. The LLR laser provides us with this opportunity. The LLR laser, also known as the laser from the Laser Lightning Rod project [9], theoretically delivers pulses with 720 mJ, 1030 nm, and 1 ps at a repetition rate of 1000 Hz. Figure 3.4.3 shows the layout of the LLR laser system. During my experiments, due to damage in one of the laser multipass amplifiers, it could only operate at a maximum energy of 240 mJ. For detailed information about this laser, please refer to [25].

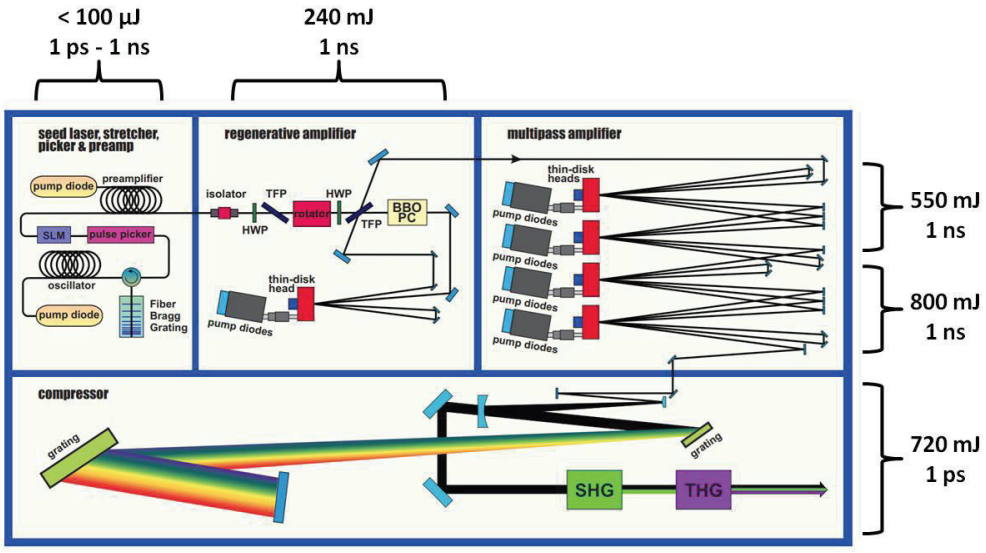

Figure 3.4.3. Layout of the LLR laser system.

We first attempted to generate long LG filaments using this very powerful kHz laser. In our initial experiments, we used a 20 m focusing lens to create the filaments. Due to the size of the phase plate, the initial beam diameter was limited to 1.6 cm, which meant the maximum energy of 240 mJ was reduced to 150 mJ. Figure 3.4.4 shows the beam profile and filament distribution along the z-axis measured using photosensitive paper, with an incident beam energy of 100 mJ. Since the repetition rate of laser cannot be adjusted, we used a chopper to reduce the beam's repetition rate to 100 Hz to be able to perfom photosensitive paper measurements of the beam profile. In this section, all the results from the photosensitive paper method were obtained using the chopper method.

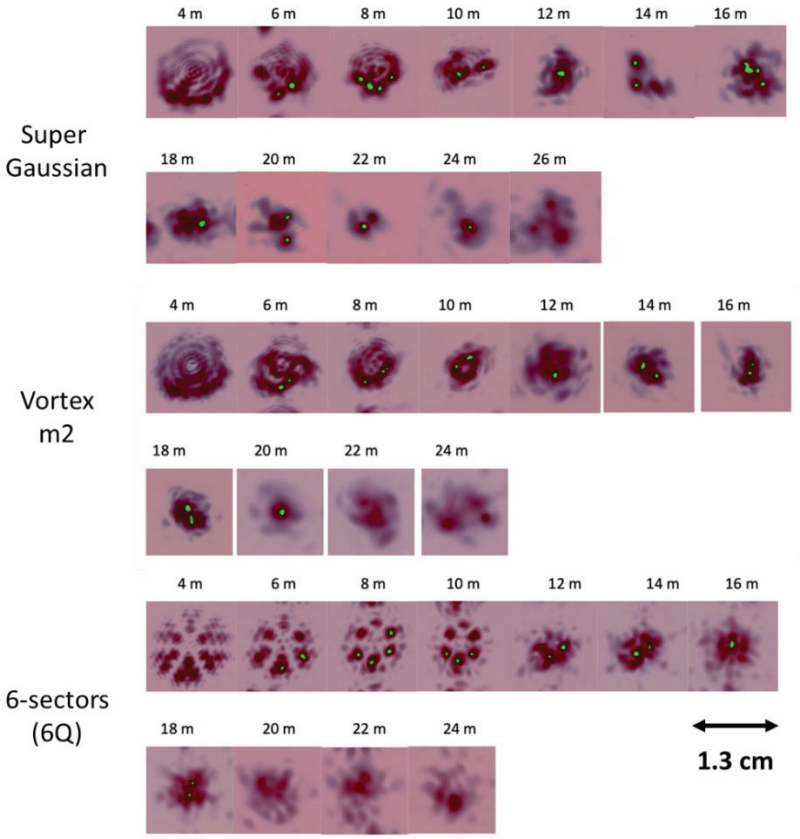

Figure 3.4.4. Beam profile and filament distribution measured using photosensitive paper. A 20 m lens was used, with an incident laser energy of 100 mJ, a pulse duration of 1 ps, at a central wavelength of 1030 nm.

It can be seen that among the three types of beams, the super-Gaussian beam produced the longest filament, particularly beyond the geometric focus. However, we believe the measurements with photosensitive paper are more important for providing information on the cross-section of the filaments. The photosensitive paper measurements can only give a rough estimate of the filament length range. Because the laser system did not offer the possibility to reduce its repetition rate or to work in single shot regime, we had to use photosensitive paper while the laser was continuously shooting. This involves quickly moving the photosensitive paper through the laser beam to capture the beam profile and filament

distribution. The resulting air disturbances and the surface debris caused by the interaction between the previous pulses and the photosensitive paper can somewhat affect the measurement results.

More precise acoustic signal measurements also confirm the filament length. Figure 3.4.5 shows the radial acoustic pressure wave measured using a microphone placed 3 cm away from the filament. It can be seen that the filament lengths produced by the three types of beams are essentially the same.

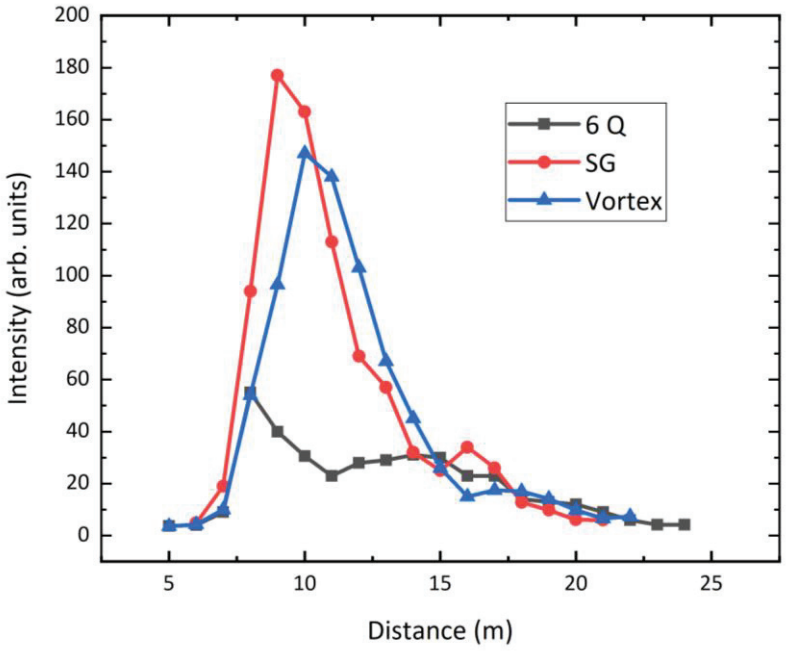

Figure 3.4.5. Acoustic signals along the z-axis of filaments produced using a 20 m focusing lens. The laser energy is 100 mJ, the pulse duration is 1 ps, and the central wavelength is 1030 nm.

Due to experimental environment limitations, the noise was too high to measure the low-density channel by the wavefront detector. We can refer to Figure 3.4.2 for the shape of the low-density channel produced by high repetition rate laser filaments. It can be seen that as the laser repetition rate increases, the radius of this low-density channel gradually increases from a few 100 µm to a few mm. Therefore, it is required that the high repetition rate filaments producing the air waveguide have a larger diameter hollow structure than in the previous air waveguide experiments. Despite numerous attempts, the LG filaments still did not produce a hollow structure with a diameter large enough to be used for air waveguides. For example, the diameter shown in Figure 3.4.4 does not meet the requirements for creating an air waveguide.

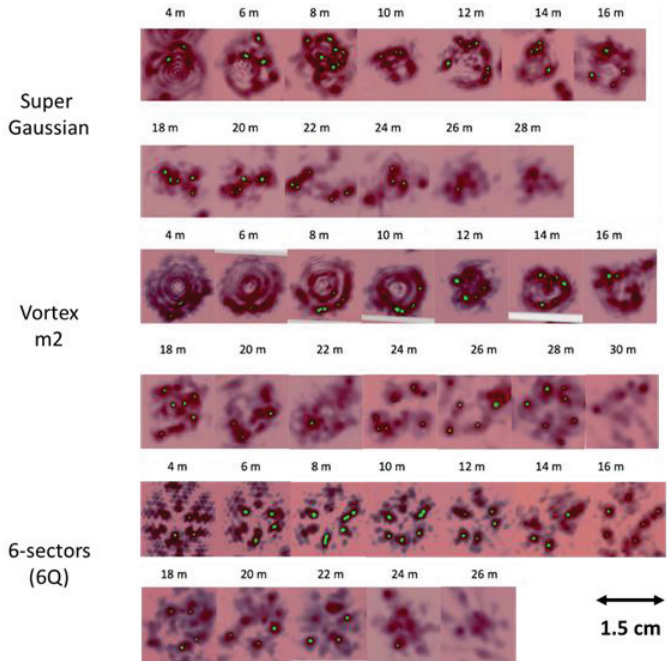

Figure 3.4.6. Beam profiles of the collimated beam and the self-focused filament measured using photosensitive paper. The incident energy of the laser was 150 mJ, with a pulse duration of 1 ps and a central wavelength of 1030 nm with a beam diameter of 1.6 cm.

Therefore, we attempted to use the collimated beam directly to generate light filaments in order to overcome the limitations of the focused beam waist. Similarly, we used photosensitive paper to measure the beam profile and filament distribution, as shown in Figure 3.4.6, with the beam energy set to the maximum value of 150 mJ. It can be observed that the light filaments are produced when the beam has propagated approximately 3-4 meters. Moreover, these filament distributions generated solely by Kerr self-focusing are relatively uniform. For Laguerre-Gaussian (LG) beams, these filament distributions generally follow the mode of beams, with the diameter of the hollow structures exceeding 5 mm. This creates conditions for generating air waveguides with LG beams and LLR laser.

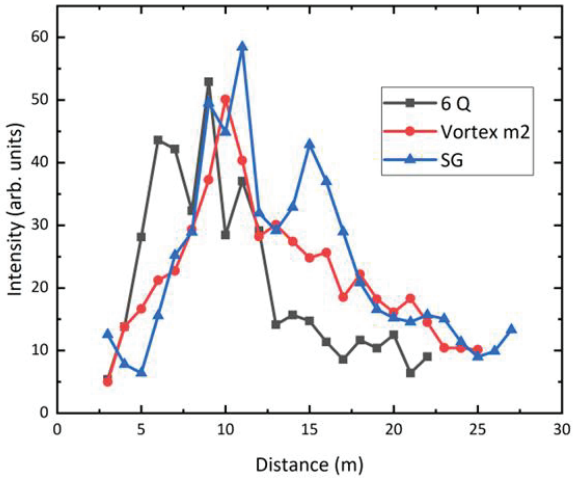

Figure 3.4.7. Acoustic signals along the z-axis of the filaments generated using a collimated beam. The laser energy is 150 mJ, pulse duration is 1 ps at a central wavelength of 1030 nm with a beam diameter of 1.6 cm.

Similarly, we measured the acoustic signals produced by the filaments using a microphone positioned 3 cm away from the filaments to determine their length. From Figure 3.4.7, it can be observed that the three types of beams generated filaments over approximately 20 meters. The 6-sectors beam produced the peak acoustic signal first. In the experiment, we also observed that the 6-sectors beam initially produced a weak plasma. As shown in Figure 3.4.8, our mirror, placed 2 meters behind the beam output, was burned by the hot spots generated by the 6-sectors plate, leaving the profile of the 6-sectors beam on the mirror coating.

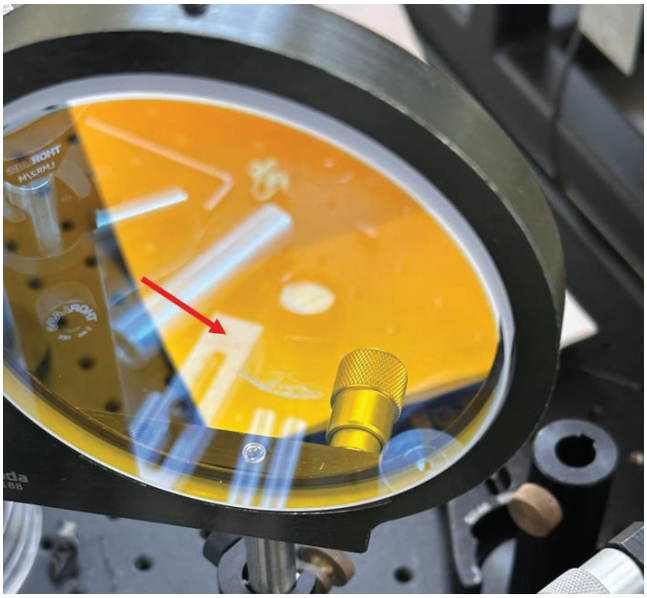

Figure 3.4.8. Burn marks on the mirror placed 2 meters behind the beam output, caused by the weak plasma generated by the 6-sectors beam.

3.4.3 Permanent air waveguides generated using a collimated Laguerre-Gaussian beam

After achieving satisfactory hollow-structured filaments, we attempted to use LLR lasers to generate permanent air waveguides. First, we made a choice between the vortex beam and the 6-sectors beam. As shown in Figure 3.4.6, the stability and the distribution of the filaments produced by the 6-sectors beam are significantly better than that of the vortex beam. If we fit a ring to the filament distribution, we can see that, except for the hollow structure diameter being smaller (5.5 mm) at 4 meters, the diameter at other positions remains relatively stable at approximately 6.5 mm. Based on this advantage in stability, we ultimately chose the 6-sectors beam to generate air waveguides.

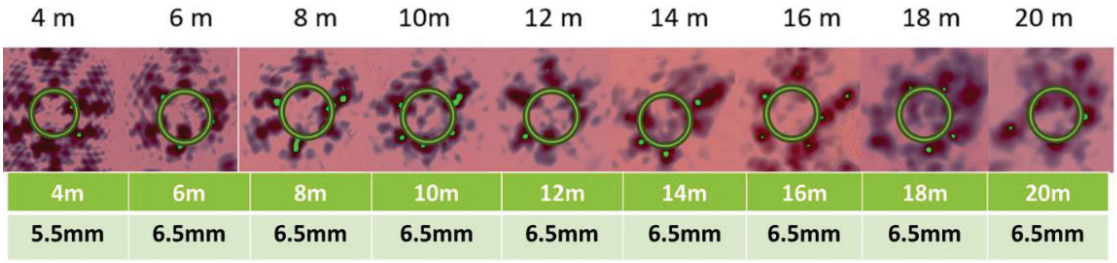

Figure 3.4.9. Ring fitting of the filament structure.

Our experimental setup is shown in Figure 3.4.10. The LLR laser passes through a hard steel iris with a diameter of 16 mm and a 6-sectors phase plate. A CW laser is focused into the hollow structure of the filament by a telescope with an effective focal length of 19 m and then imaged at $z = 60\ m$ on a CMOS camera placed behind several filters to block the beam at 1030 nm. The camera has an integration time of 60 µs. On the right side of Figure 3.4.10, we also provide an actual photograph of this experiment.

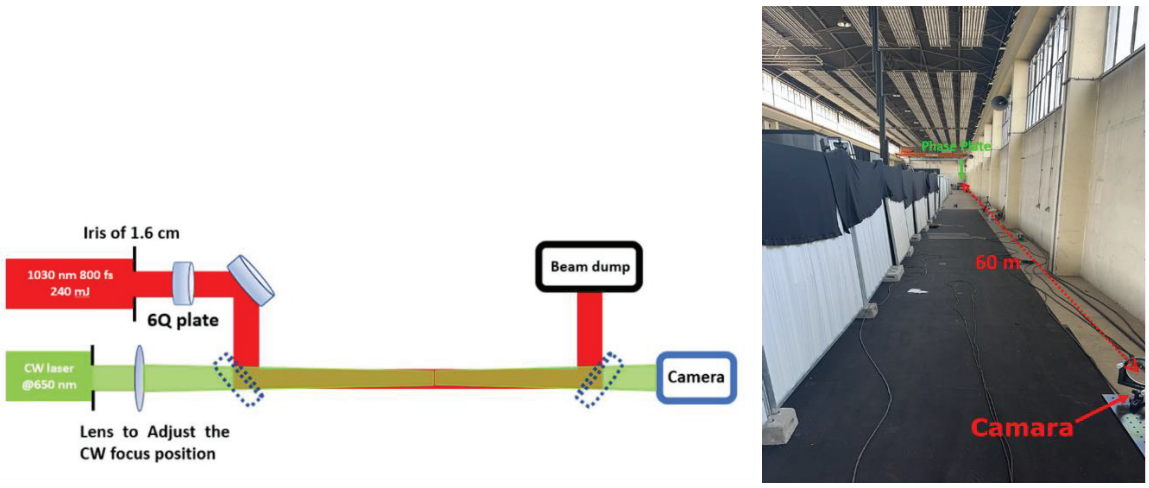

Figure 3.4.10. Experimental setup for generating permanent air waveguides. Left: Schematic diagram of the experimental setup. Right: Actual photograph of the experimental setup and environment.

Fig. 3.4.11 presents the probe beam profile measured for different input energies of the Yb:YAG laser. One can see that a guided mode with a mm size intense spot on the center of the beam appears when the input energy exceeds 61 mJ, corresponding to a peak power of 61 GW. The probe beam profile with 146 mJ pulse energy is also measured for different delays between the Yb:YAG pulse and the camera ranging from 0 to 800 µs. One can see that the shape of the probe beam remains constant over time, with a pointing stability significantly better than the one observed with a laser at 10 Hz [2]. This indicates that we have successfully created permanent air waveguides.

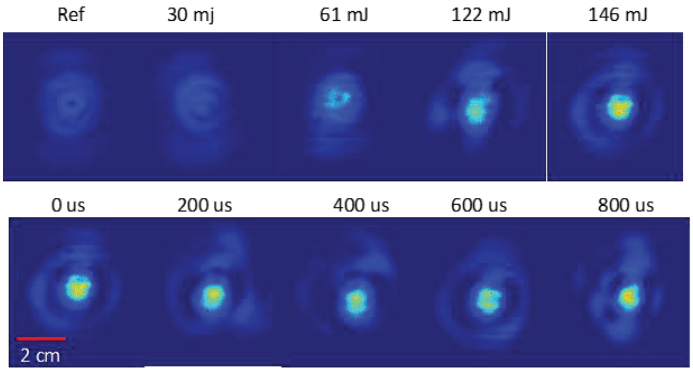

Figure 3.4.11. Image of the probe beam measured on a CMOS camera for different input energies of the Yb:YAG laser (top raw) and for different delays between the filament formation and the camera with the laser energy 146mJ (bottom raw).

We simulated the propagation of the beam in this hollow structure. Based on our experimental results and previous studies on low-density channels [15] and air waveguides [2], we provided an approximate structure of the low-density channel, as shown in Figure 3.4.12. It can be seen that a low-refractive-index air low-density channel is generated at the position of the filament (r = 0.35 cm).

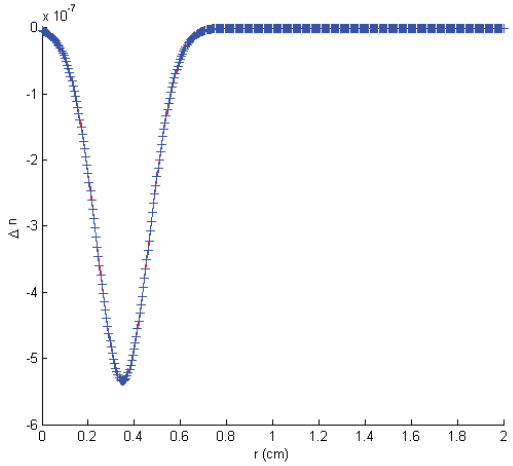

Figure 3.4.12. Refractive index variation in the low-density channel used in the simulation of air waveguides.

The comparison between simulation and experiment are shown in Figure 3.4.13. We observe a qualitative agreement with the simulations, even though the guided beam is slightly smaller in the simulation. We believe this is because, in our simulation, we used an ideal super-Gaussian beam (flat-topped beam). However, as seen in Figure (a), the actual incident beam mode is complex.

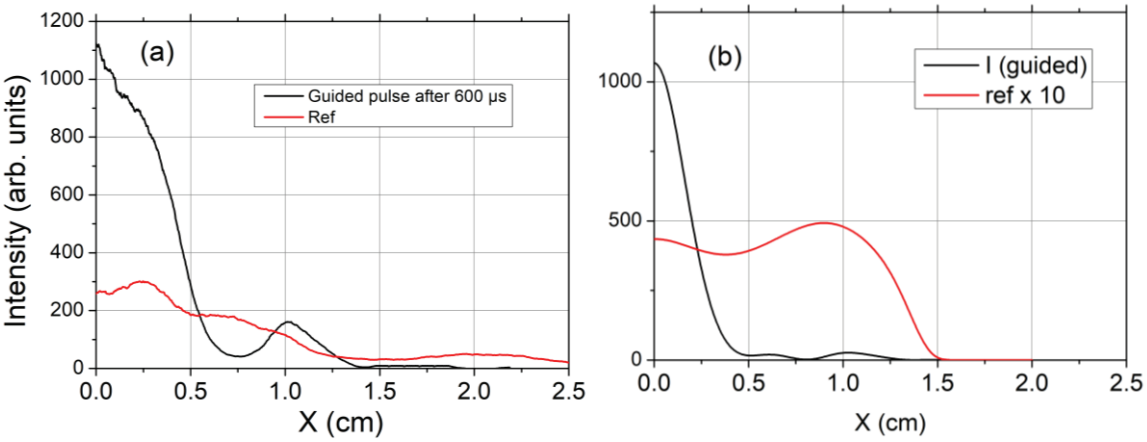

Figure 3.4.13. Beam profiles after propagation through the air waveguide structure in experiment (a) and simulation (b). The black lines represent the results with the air waveguide, and the red lines represent the beam profiles in the absence of air waveguide.

3.4.4 Generation of a “Quasi-Axicon” using a focusing lens

In our experiments, we also discovered some other interesting phenomena. We found that even without using any OAM (Orbital Angular Momentum), when the probe beam was directly focsused into the single low-density channel created by a supergaussian beam, we also observe a reduction of the probe beam diameter at long distance. The observed profile is different from that shown in Figure 3.4.1. since it appears as a very stable quasi bessel beam.

Our experimental setup is shown in Figure 3.4.14.

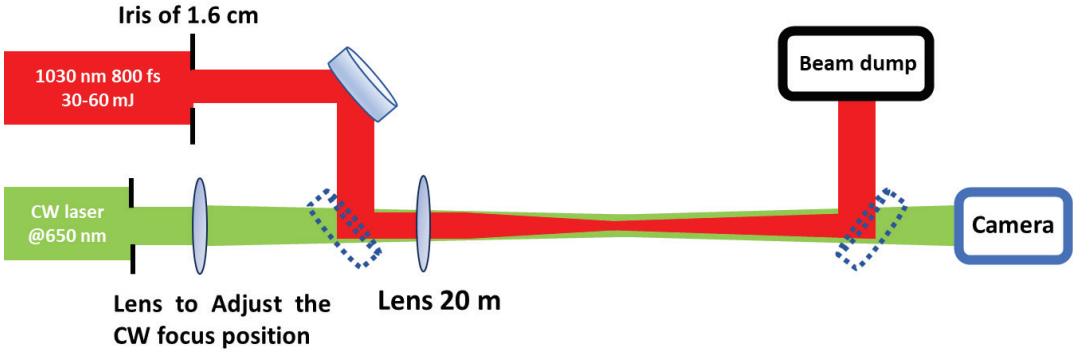

Figure 3.4.14. Experimental setup for generating a “quasi-bessel beam” in air.

Here, we chose a relatively low energy to produce long single filaments. Our experimental results are shown in Figure 3.4.15. It can be seen that when the incident pulse energy exceeds 30 mJ, we obtained very distinct profiles resembling focused quasi-Bessel beams.

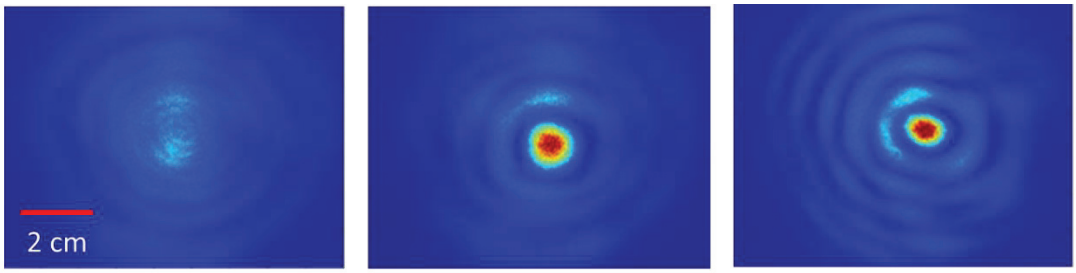

Figure 3.4.15. "Quasi-Bessel beam" generated in air by low density channel.

In fact, such results are not surprising. In previous studies [15], as shown in Figure 3.4.2, we observed that the low-density channel created by high repetition rate filaments resembles the structure of an axicon. Also this focusing effect has been previously reported with shorter filements by Lahav *et al.* [5]. We subsequently performed simulations for this situation. Figure 3.4.16 shows the structure of the low-density channel used in these simulations.

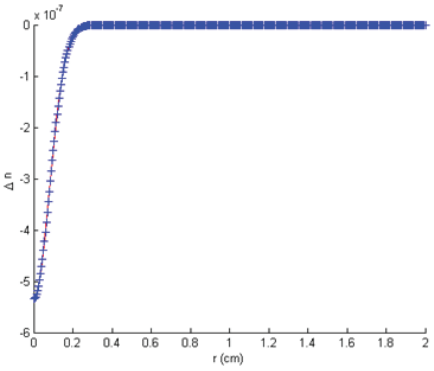

Figure 3.4.16. Low-density channel used in the quasi-axicon simulation.

The comparison results between experiment and simulation are shown in Figure 3.4.17. It can be seen that our experimental results and simulations are in very good agreement.

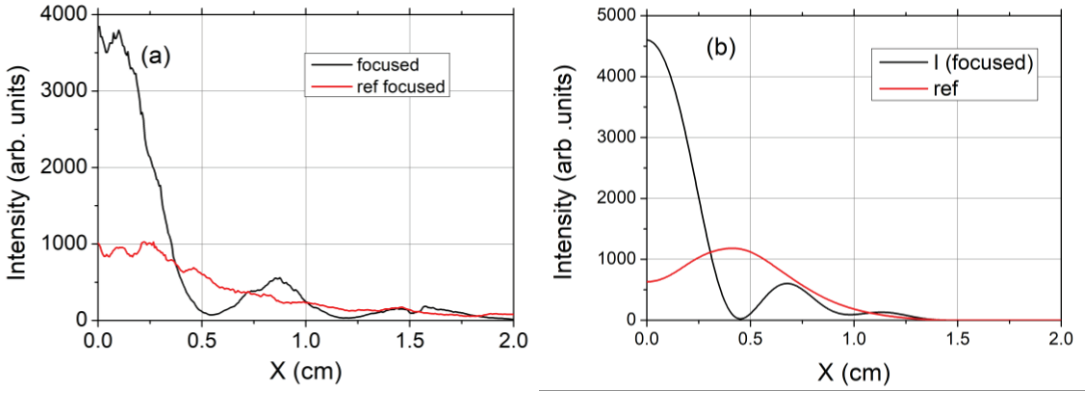

Figure 3.4.17. Beam profiles after propagation through the "quasi-axicon" structure in air. The black lines represent the results with focusing, and the red lines represent the beam profiles without the filament. (a) Experimental results. (b) Simulation results.

3.5 Conclusions and outlook

In this chapter, we demonstrated that the filamentation of vortex beams can be used to create air waveguides. By introducing a multi-focus phase plate, we achieved control over the focal structure, enabling the creation of air waveguides over longer distances. Most importantly, we utilized the cumulative effect of low-density air channels to generate permanent air waveguides several tens of meters long, as recently reported over a smaller scale in [26]. In this work, we also found that long-distance, high repetition rate filamentation can produce structures in air resembling an axicon, resulting in the formation of a quasi-Bessel beam.

These air waveguides generated through filamentation hold promise for improving applications such as remote Laser-Induced Breakdown Spectroscopy (LIBS) [4], where filaments could be used to generates a plasma on a ample and air waveguide would be used to guide the LIBS signal from the plasma. Additionally, the air waveguide and "quasi-axicon" suggest that the hydrodynamic effects created by filaments, especially those generated by high repetition rate lasers, could potentially be used to manipulate laser beams through the formation of diffractive, dispersive, or focusing elements made of gas.

References

1. N. Jhajj, E.W. Rosenthal, R. Birnbaum, J.K.. Wahlstrand, H. Milchberg. Demonstration of long-lived high-power optical waveguides in air. Physical Review X **4**, 011027 (2014).
2. S. Fu, B. Mahieu, A. Mysyrowicz, A. Houard. Femtosecond filamentation of optical vortices for the generation of optical air waveguides. Opt. Lett. **47**, 5228-5231 (2022).
3. A. Goffin, I. Larkin, A. Tartaro, A. Schweinsberg, A. Valenzuela, E. W. Rosenthal, and H. M. Milchberg. Optical Guiding in 50-Meter-Scale Air Waveguides. Phys. Rev. X **13**, 011006 (2023).
4. P. J. Skrodzki, T. Nutting, M. Burger, L. A. Finney, J. Nees, and I. Jovanovic. Guiding of Spectroscopic Signal with a Concatenated Filament-Driven Waveguide. in CLEO 2023, Technical Digest Series (Optica Publishing Group, 2023), paper ATh4I.4.
5. O. Lahav, L. Levi, I. Orr, R-A. Nemirovsky, J. Nemirovsky, I. Kaminer, M. Segev, and O. Cohen. Long-lived waveguides and sound-wave generation by laser filamentation. Phys. Rev. A **90**, 021801(R) (2014).
6. D. Comtois, C. Y. Chien, A. Desparois, F. Génin, G. Jarry, T. W. Johnston, J.-C. Kieffer, B. L. Fontaine, F. Martin, R. Mawassi, H. Pépin, F. A. M. Rizk, and F. Vidal. Triggering and guiding leader discharges using a plasma channel created by an ultrashort laser pulse. Appl. Phys. Lett. **76**, 819–821 (2000).
7. S. Tzortzakis, B. Prade, M. Franco, A. Mysyrowicz, S. Hüller, et P. Mora. Femtosecond laser-guided electric discharge in air. Phys. Rev. E **64**, 057401 (2001).
8. S. Uchida, Y. Shimada, H. Yasuda, S. Motokoshi, C. Yamanaka, T. Yamanaka, Z. Kawasaki, and K. Tsubakimoto. Laser-triggered lightning in field experiments. J. Opt. Technol. **66**, 199–202 (1999).
9. A. Houard, P. Walch, T. Produit, V. Moreno, B. Mahieu, A. Sunjerga, C. Herkommer, A. Mostajabi, U. Andral, Y.-B. André, M. Lozano, L. Bizet, M. C. Schroeder, G. Schimmel, M. Moret, M. Stanley, W. A. Rison, O. Maurice, B. Esmiller, K. Michel, W. Haas, T. Metzger, M. Rubinstein, F. Rachidi, and J.-P. Wolf. Laser-guided lightning. Nat. Photonics **17**, 231 (2023).
10. G. Schimmel, T. Produit, D. Mongin, J. Kasparian, and J-P. Wolf. Free space laser telecommunication through fog. Optica **5**, 1338-1341 (2018).
11. T. Wang, S. Bin Ali Reza, F. Buldt, P. Bassène, M. N'Gom. Structured light signal transmission through clouds. J. Appl. Phys. **133**, 043102 (2023).
12. J. K. Wahlstrand, N. Jhajj, E. W. Rosenthal, S. Zahedpour, and H. M.Milchberg. Direct imaging of the acoustic waves generated by femtosecond filaments in air. Opt. Lett. **39**, 1290 (2014).
13. G. Point, C. Milián, A. Couairon, A. Mysyrowicz, and A. Houard. Generation of long-lived underdense channels using femtosecond filamentation in air. J. Phys. B **48**, 094009 (2015).
14. G. Point, Y. Brelet, A. Houard, V. Jukna, C. Milián, J. Carbonnel, Y. Liu, A. Couairon, and A. Mysyrowicz. Superfilamentation in Air. Phys. Rev. Lett. **112**, 223902 (2014).
15. P. Walch, B. Mahieu, L. Arantchouk, Y.-B. Andre, A. Mysyrowicz, and A. Houard. Cumulative air density depletion during high repetition rate filamentation of femtosecond laser pulses: Application to electric discharge triggering. Appl. Phys. Lett. **119**, 264101 (2021).
16. P. Georg. A New Method for Numerical Abel-Inversion. Zeitschrift für Naturforschung A,. **46**, 639-641 (1991).
17. S. Tzortzakis, G. Méchain, G. Patalano, M. Franco, B. Prade and A. Mysyrowicz. Concatenation of plasma filaments created in air by femtosecond infrared laser pulses. Appl Phys B **76**, 609–612 (2003).

18. P. Polynkin. Multi-pulse scheme for laser-guided electrical breakdown of air. Appl. Phys. Lett. **111**, 161102 (2017).
19. P. Polynkin, Z. Samsonova, A. Englesbe, A. Lucero, J. Elle, A.Schmitt-Sody. Channeling the dielectric breakdown of air by a sequence of laser-generated plasma filaments. JOSA B **36**-11-3024 (2019).
20. J. Papeer, R. Bruch, E. Dekel, O. Pollak, M. Botton, Z. Henis, A. Zigler. Generation of concatenated long high density plasma channels in air by a single femtosecond laser pulse. Appl. Phys. Lett. **107**, 124102 (2015).
21. LBTEK website. https://www.lbtek.com/product/746.html
22. L. L. Doskolovich, E. A. Bezus, A. A. Morozov, V. Osipov, J. S. Wolffsohn, and B. Chichkov. Multifocal diffractive lens generating several fixed foci at different design wavelengths. Opt. Express **26**, 4698-4709 (2018).
23. I. Dicaire, V. Jukna, C. Praz, C. Milián, L. Summerer and A. Couairon. Spaceborne laser filamentation for atmospheric remote sensing. Laser & Photonics Reviews **10**, 481-493 (2016).
24. M. Châteauneuf, S. Payeur, J. Dubois, J.-C. Kieffer. Microwave guiding in air by a cylindrical filament array waveguide. Appl. Phys. Lett. **92**, 091104 (2008).
25. C. Herkommer, P. Krötz, R. Jung, S. Klingebiel, C. Wandt, R. Bessing, P. Walch, T. Produit, K. Michel, D. Bauer, R. Kienberger, and T. Metzger. Ultrafast thin-disk multipass amplifier with 720 mJ operating at kilohertz repetition rate for applications in atmospheric research. Opt. Express **28**, 30164-30173 (2020)
26. A. Goffin, A. Tartaro, and H. M. Milchberg. Quasi-steady-state air waveguide. Optica **10**, 505-506 (2023).

Chapter 4

Extending Filaments Along the Laser Axis - Guiding Longer Discharges

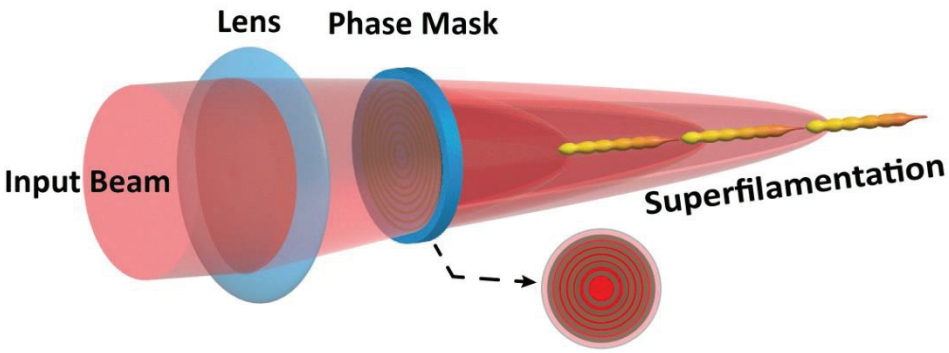

Figure 4.1. Extending superfilamentation using multifocal phase mask

The lightning rod designed by Benjamin Franklin in the 18th century could change the path of lightning, giving humanity the ability to control this natural force for the first time. However, in the past two hundred years, while these lightning rods have been widely installed on human structures, there has been little technological advancement. In 2021, the LOA group in collaboration with Univeristy of Geneva demonstrated the use of lasers to guide lightning [1], marking a significant step forward in the field of precisely directing and triggering lightning discharges. In this chapter, we will discuss the principles and historical development of guiding high-voltage discharges using lasers, and present our successful extension of high-voltage discharge distances using two different methods.

4.1 Development and principles of laser-guided discharges

4.1.1 Development of laser-guided discharges

The lightning rod designed by Benjamin Franklin in the 18th century can alter the path of lightning and provide some protection for buildings. This cheap and effective method is still widely used today. However, the limitations of this method are quite evident. First, it can only be installed on top of buildings. Second, it cannot control the direction and location of the lightning discharge. Most importantly, the protective capability of the lightning rod is constrained by its height with a maximum protection range of 30 m. The radius of the protected area is roughly equal to the height of the lightning rod. For example, a 20-meter-high lightning rod can at most protect an area within a 20-meter radius from lightning strikes. To protect large infrastructure, such as airports, it is therefore necessary to develop new types of lightning protection.

Figure 4.1.1. Photography of the Oriental Pearl Tower in Shanghai, China, struck by lightning.

To overcome these limitations, people have tried to launch small rockets trailing metal wires into thunderclouds. In the presence of the thundercloud electric field the wire becomes polarized and generates discharge precursors at its tips toward the clouds and the ground. When the connection is realized the lightning spark is then guided through the wire to the ground [2]. However, this technique is expensive and requires precise monitoring of the ambient electric field for a success rate of only 60%. Additionally, it is a single-use method for which the falling debris from the rockets poses a certain danger [3].

In the 1970s, with the advent of energetic lasers such as Q-switched Nd:YAG and CO_2 lasers with peak power in the MW range, as well as the possibility of inducing optical breakdown of air, the idea of using lasers to trigger lightning emerged [4,5]. However, these lasers typically have long pulse durations, in the nanosecond scale, which makes it difficult for the laser to generate very long plasma channel due to avalanche ionization.

In the 1990s, the generalization of solid-state Ti:sapphire femtosecond lasers using chirped pulse amplification technology brought new prospects to the field of laser-triggered lightning. Filamentation in air can generate a continuous column of weakly ionized plasma over distances of several hundred meters with a moderate laser energy [6,7], making it a much more effective way to guide electric discharges in air. Until 2012, filamentation has been proven to trigger and guide electric sparks several meters long [8] and even to alter the natural path of discharges [6]. Notably, during my Ph.D. thesis, the LLR project led by my supervisor, Dr. Aurelien Houard, was the first to demonstrate the possibility of using lasers to guide lightning [1].

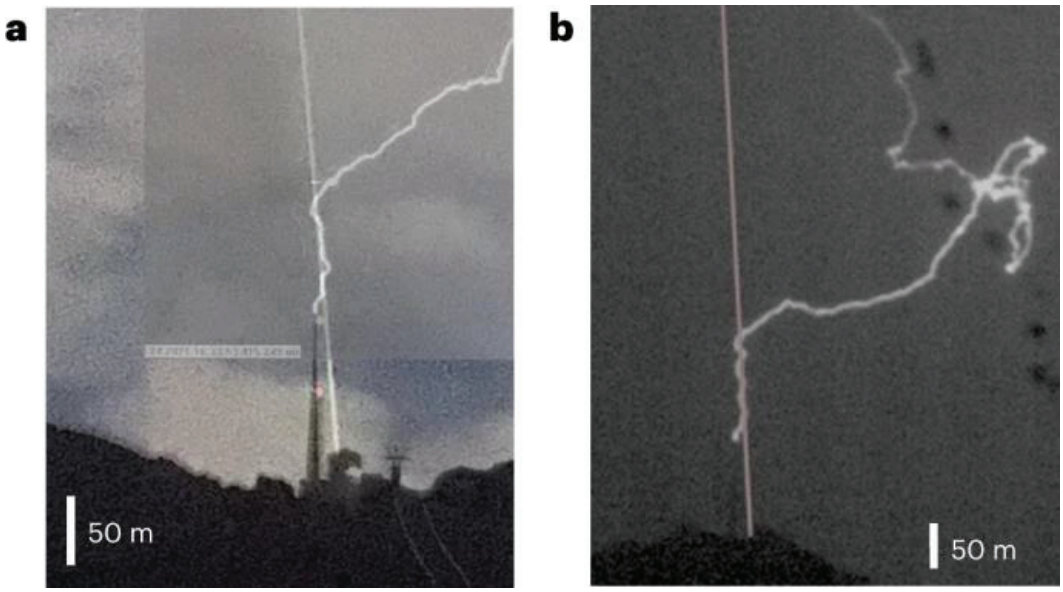

Figure 4.1.2. Photography of a guided lightning using laser filaments. It can be seen that the lightning is directed along the path of the laser (from [1]).

4.1.2 Townsend discharge and Paschen's law

The earliest model describing the formation of discharges in air in the early 20th century, is called Townsend discharge or Townsend avalanche. In this model, two electrodes have a potential difference U and are separated by a distance d, creating a constant electric field E generated by the electrodes.

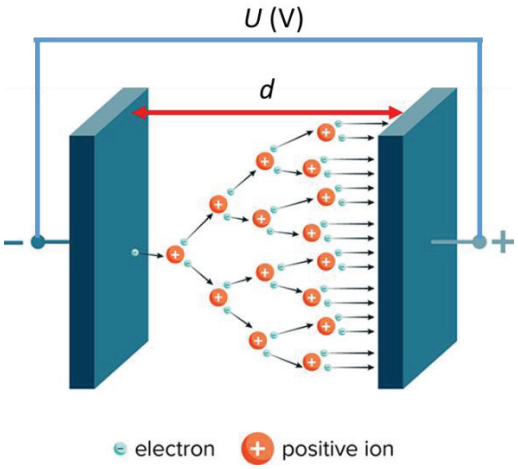

Figure 4.1.3. Schematic of the Townsend discharge.

A small number of electrons, called seed electrons, are present in the medium and often come from ionization of the ambient gas by cosmic radiation. These electrons are accelerated towards the cathode by the electric field. They gradually gain kinetic energy before colliding with molecules of the medium. If the acquired kinetic energy is sufficient for ionization, the electron collision with the molecule will produce two low-energy electrons, which will again be accelerated by the electric field. The number of free electrons will double with each cycle, leading to an electron avalanche and a complete ionization of the medium, thereby initiating a discharge.

However, there are electron recombination and attachment phenomena in the medium, meaning that some electrons will disappear from the medium rather than participate in the avalanche ionization. In this case, if the number of electrons produced by the avalanche per unit length is less than the number of electrons recombined/captured per unit length, nothing will happen in the medium, as free electrons disappear at approximately the same rate they are produced. Conversely, if the number of electrons produced by the avalanche per unit length is greater than the number of electrons recombined/captured per unit length, an electron avalanche will occur, leading to a discharge, as shown in Figure 4.1.3.

Based on this model, we can derive an expression for the voltage required to initiate a discharge, known as the breakdown voltage. This expression is referred to as Paschen's Law [9]. We again consider two charged plane electrodes separated by a distance d, creating a constant electric field E between them. We assume that the electrons accelerated by the electric field generate other electrons through collisions with a linear efficiency α, and no recombination or capture occurs. This gives us the following equation for the electron density N_e:

$$\frac{dN_e}{dz} = \alpha(E,p)N_e(z), \tag{4.1.1}$$

where p denotes the gas pressure.

Assuming that the seed electron is generated at $z = 0$, the number of electrons as a function of distance z is given by:

$$N_e(z) = N_e(0)\exp(\alpha(E,p)z)\,. \tag{4.1.2}$$

During the propagation of electrons towards the anode, $(\exp(\alpha(E,p)d) - 1)$ new electrons and positive ions are generated. Townsend introduced a second coefficient γ, to account for heavy ions reaching the cathode and knocking out new electrons. Therefore, the total number of free electrons left in the gap after the avalanche is:

$$N_{e,\text{final}} = \frac{\exp(\alpha(E,p)d)-1}{\gamma}, \tag{4.1.3}$$

where γ is the dimensionless second Townsend coefficient. The condition for the gap medium to become conductive (breakdown condition) is

$$N_{e,\text{final}} \geq 1. \tag{4.1.4}$$

Thus, we get

$$\frac{\exp(\alpha(E,p)d)-1}{\gamma} \geq 1. \tag{4.1.5}$$

This simplifies to

$$\exp(\alpha(E,p)d) \geq 1 + \frac{1}{\gamma}. \tag{4.1.6}$$

Taking the natural logarithm on both sides, we obtain

$$\mathrm{A}(E,p)d \geq \ln\left(1 + \frac{1}{\gamma}\right). \tag{4.1.7}$$

Townsend showed that the first Townsend coefficient α follows the semi-empirical formula:

$$\alpha(E,p) = Ap\exp\left(\frac{-Bp}{E}\right), \tag{4.1.8}$$

where A and B are constants determined from experimental data. Substituting α into the above equation, we get:

$$Apd\exp\left(\frac{-Bp}{E}\right) \geq \ln\left(1 + \frac{1}{\gamma}\right). \tag{4.1.9}$$

Considering the voltage between the electrodes $U = E \cdot d$, we can rewrite E as $\frac{U}{d}$

$$Apd\exp\left(\frac{-Bpd}{U}\right) \geq \ln\left(1 + \frac{1}{\gamma}\right). \tag{4.1.10}$$

Solving for the breakdown voltage U_{bd}, we get

$$\frac{-Bpd}{U_{bd}} = \ln\left(\frac{\ln\left(1+\frac{1}{\gamma}\right)}{Apd}\right). \tag{4.1.11}$$

Rearranging, we find

$$U_{bd} = \frac{Bpd}{\ln(Apd) - \ln\left(\ln\left(1+\frac{1}{\gamma}\right)\right)}. \tag{4.1.12}$$

This formula describes the relation between breakdown voltage, gas pressure, and gap length, which was first empirically derived by Paschen and later independently discovered by Townsend. This relationship is known as Paschen's Law [9].

4.1.3 Streamer discharge

In the decades following the introduction of Townsend discharge and Paschen's Law, it gradually became evident that this theory could not explain phenomena observed in long-distance and highly asymmetric gap discharges, for which the estimated breakdown threshold was significantly higher than the experimental results. In the 1940s, Loeb, Meek, and Raether independently introduced the concept of streamer discharge [10,11] to address the high-voltage discharge phenomena that the traditional Townsend discharge model could not explain. The process of streamer discharge can be summarized as follows:

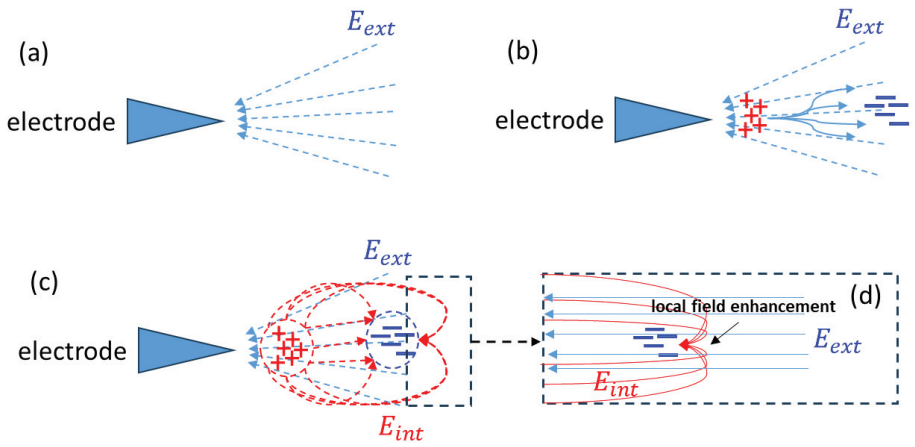

Figure 4.1.4: Schematic of a streamer discharge (a): Initial inhomogeneous electric field (blue dashed lines) when the electrode is negatively charged. (b): Avalanche process generating free electrons and ions, with electrons rapidly moving towards the positive electrode under the influence of the electric field. (c): Formation of dipolar space charge field (red dashed lines). (d): Enhancement effect of the local electric field.

1. Initiation of a discharge

Streamer discharges typically occur in an inhomogeneous electric field environment. Suppose we have two asymmetric electrodes, one positively charged and the other negatively charged. Due to the asymmetry of the electrodes, the electric field distribution between them is also uneven, with a higher field strength near the electrode with the smaller radius of curvature (usually a pointed electrode). This corresponds to the process in Figure 4.1.4 (a).

2. Generation of seed electrons and initial avalanche

This process is similar to the Townsend discharge as described in section 4.1.2. This corresponds to the process in Figure 4.1.4 (b).

3. Formation of space charge field

Since the mobility of electrons in the electric field is much higher than that of ions, the free electrons produced during the avalanche quickly leave their original position, leaving behind positive ions to form a plasma. As the electron avalanche develops and the external electric field accelerates, the number of electrons in the front region increases sharply, forming a high-density electron region. This leads to the creation of a space charge field, similar to a dipole field. Within this dipole field, the direction of the electric field is opposite to the external electric field, but at the discharge tip, the space charge field enhances the total electric field at the avalanche head, making the avalanche process more intense. This corresponds to the process in Figure 4.1.4 (c).

4. Formation of corona discharge and streamer

In the absence of space charge field, the discharge process is led by the external electric field, and the avalanche will propagate around the electrode as long as the local external electric field is high enough to sustain ionizing collisions (typically over a few centimeters). Therefore, the resulting plasma remains confined near the electrodes, usually manifesting as a uniform corona discharge.

When the space charge field is strong enough, it can significantly alter the distribution of the external electric field, forming a localized high electric field region, corresponding to the process in Figure 4.1.4 (d). This results in the maintenance of significant ionization even in areas where the background electric field is lower than the breakdown threshold. Consequently, the discharge will propagate further than the predictions of the Townsend model. Moreover, during the electron avalanche process, the recombination of high-energy electrons will emit high-energy photons. These photons can further ionize the surrounding gas molecules, promoting the extension of the discharge process. This type of discharge can form elongated, finger-like streamer structures, as shown in Figure 4.1.5.

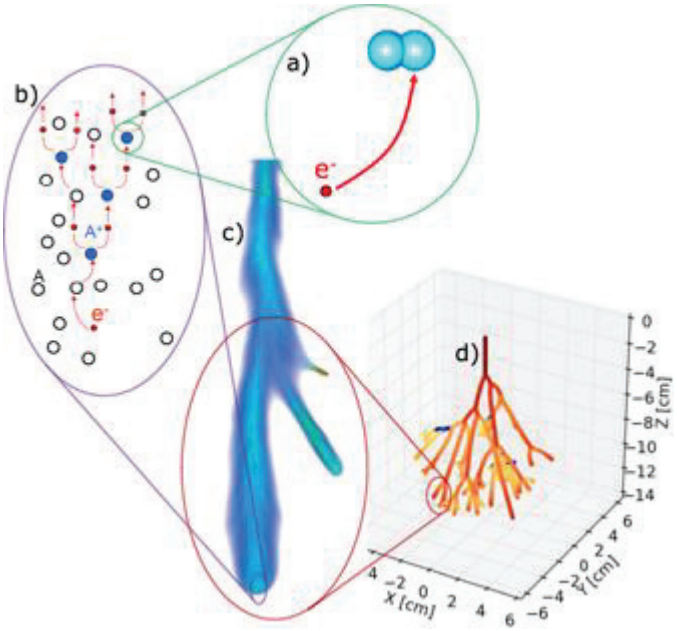

Figure 4.1.5. Description and structure of a streamer discharge: (a) Electrons colliding with atoms or molecules; (b) Multiple electrons accelerated by the space charge field and colliding with neutral gas molecules to form an ionization avalanche; (c) Branching streamer discharge with enhanced field at the tip; (d) Elongated, finger-like streamer structures. From [12].

Streamer discharges typically form low-density and low-temperature plasma. The processes of electron recombination and attachment of free electrons to oxygen ions in this type of plasma are highly efficient, resulting in a plasma lifetime on the order of nanoseconds. The ionization wave of the streamer propagates at a speed of approximately 10^7 to 10^8 m $\cdot$ s^{-1} [13]. As the streamer propagates away from the cathode, the external electric field gradually weakens, and the induced electric field also decreases with propagation. This results in a maximum propagation distance for a streamer of a few 10s of centimeters at atmospheric pressure.

4.1.4 Leader discharge

For large-scale discharge phenomena such as lightning, streamer discharges are clearly insufficient to provide an explanation. Here, we need to introduce another physical phenomenon: the leader discharge phenomenon. Leader discharges typically follow streamer discharges and are essential for the development of long spark discharges, such as lightning. They appear when multiple streamers, which create initial ionization channels, fail to bridge the entire gap between electrodes. The combined currents from these streamers heats significantly the point from which they originate, raising the plasma temperature and increasing its conductivity. This results in the formation of a highly conductive leader channel at the base of the streamers, which propagates slowly through the gap. Leaders move much slower than streamers, typically at speeds of 10^4 to $10^5 m/s$, and can propagate in steps, particularly in lightning scenarios. The leader channel maintains high conductivity due to the high temperature, preventing electron recombination and allowing further extension. The leader-streamer system ensures continuous ionization and extends the discharge path. When this system nears the opposite electrode, the electric field intensifies, leading to a rapid final jump that completes the conductive channel across the gap, resulting in a full spark discharge. Leaders can bridge much larger gaps than streamer discharges, making them crucial to explain long spark discharges like lightning.

4.1.5 Using lasers to guide and trigger discharges

After discussing the principles of discharge in air, let's return to the topic of using laser filaments to guide discharges. During the fifty years of attempts to use lasers to guide discharges, several models have been proposed to explain the underlying physics of this process. The main models include:

1. Considering the plasma created by the filaments as a conductor

One can consider the plasma created by the filament as a conductor, like the metallic wire pulled by rockets to trigger lightning. However, it is necessary to take into account the time required for the plasma to reach equipotential, known as the polarization time. If such a filament were a perfect conductor with no resistance, this time would be zero. However, considering the filament we create in the air is only weakly ionized, the polarization time is on the order of microseconds, while the plasma lifetime in the filament is on the order of nanoseconds. Clearly, this means that the filament cannot act as a conductor during the discharge process due to its short lifetime.

2. Free electrons in the filament as seed electrons

The free electrons produced in the filament can act as seed electrons, enhancing the avalanche process during discharge propagation. This helps in initiating the discharge propagation, but experiments have shown that the speed of such discharge is about $10^4 - 10^5 \mathrm{m/s}$. Considering the plasma lifetime is on the order of nanoseconds, discharges beyond a few centimeters would not be feasible. However, experimentally, we observe discharge guidance over several tens of meters [1].

3. Low-density channels created by heating from femtosecond filaments

The currently widely accepted theory involves the low-density channels created by heating from femtosecond filaments. After the formation of a filament, some of the kinetic energy of the free electrons leads to heating of the surrounding medium. As discussed in the section on air waveguides, the heat is initially confined to the volume occupied by the plasma filament. It is then quickly released into the surrounding medium, forming an outward pressure wave and creating a low-density channel. This low-density channel will slowly expand radially, with a lifetime of a few milliseconds. This low-density locally increases the electron mean free path, reducing the breakdown voltage. It produced a preferred path for the propagating discharge responsible for the guiding effect.

Therefore, to guide discharges, the length of the filament is crucial. Additionally, the plasma generated by filamentation needs to be sufficiently dense to create a low-density channel that effectively reduces the electron mean free path and, consequently, the breakdown voltage.

4.2 Optimization of discharge guiding using filaments generated by Laguerre-Gaussian beams

In Chapters 2 and 3, we discussed in detail the generation of Laguerre-Gaussian (LG) filaments for the creation of air waveguides. In this chapter, we will introduce the advantages of using laser filaments generated by LG beams for the guiding of electric discharges.

4.2.1 Advantages of filaments generated by Laguerre-Gaussian beams

After conducting extensive research on the filaments produced by Laguerre-Gaussian (LG) beams in my thesis, the potential advantages of using LG beam-generated filaments for discharge guidance have become very clear.

First, Laguerre-Gaussian beams can produce longer filaments. In our air waveguide experiments, we observed that LG beams generated longer filaments compared to super-Gaussian beams [14]. This is directly related to the effectiveness of discharge guidance. As previously mentioned, longer filaments create longer low-density channels, which increases the length of the guiding effect.

Second, Laguerre-Gaussian beams can produce more stable filaments. Due to the unique phase structure of LG beams, the filaments they produce exhibit better stability [15]. This stability ensures a more consistent low-density channel, which may be crucial to guide discharges.

Third, Laguerre-Gaussian beams can generate multiple filaments. As discussed in the final subsection of Chapter 2, LG beams with high topological charges can simultaneously generate multiple filaments. This multi-filament structure can cover a larger area and provide multiple discharge paths, increasing the possibility of successful discharge guidance.

4.2.2 Experimental and numerical study of Laguerre-Gaussian filaments for discharge guiding

In this experiment, we compared the filaments produced by a supergaussian beam LG00, a vortex beam LG40 and a 6-sectors beam LG03 with similar input power. In particular we studied their ability to guide electric discharges.

We used the ENSTA mobile laser. The laser beam was limited by a diaphragm with a diameter of 22 mm and focused by a converging lens with a focal length of 5 m (corresponding to a numerical aperture N.A. = 0.0044). The energy was fixed to 22 mJ, and the pulse was positively chirped to 550 fs to avoid damage in the phase plate, corresponding to a peak power of 31 GW. LG beams were produced by inserting phase plates (spiral phase plates manufactured by Holo/or) into the beam path after the focusing lens. The experiment was conducted at 10 Hz, and the beam profile and the onset of filamentation were characterized along the *z* propagation axis by inserting photosensitive paper into the beam path [16].

Numerical simulations were performed to analyze the nonlinear propagation of the the three different beams. We modeled the beam and filament distribution by solving the nonlinear Schrödinger equation using the frozen time approximation. The model includes the effects of diffraction, the optical Kerr effect with nonlinear refractive index coefficient $n_2 =$

$2.9 \times 10^{-19}\, cm^2/W$, plasma induced effects including plasma defocusing, plasma absorption and nonlinear losses due to multiphoton ionization with cross section $\sigma_8 = 3.7 \times 10^{-96} \mathrm{s}^{-1}\ \mathrm{cm}^{16}.\mathrm{W}^{-8}$. Ionization induced effects are implemented by a preliminary mapping between peak intensity and electron density through the ionization model using a fixed Gaussian pulse profile over the whole propagation length. The numerical scheme for space marching the laser pulse relies on standard technique, propagating the spectral angular components of the field envelope for linear effects and field spatial components in direct space for nonlinear effects [17]. To start from realistic input conditions, the initial laser beam in the simulations is a 2.2 cm large super-Gaussian beam of order 16, which represents the experimental beam immediately after the focusing lens and thus carries a parabolic phase describing the effect of the lens, a phase increment describing the effect of the 6-sectors or M4 phase plate, and additional white noise describing the irregularities of the beam profile.

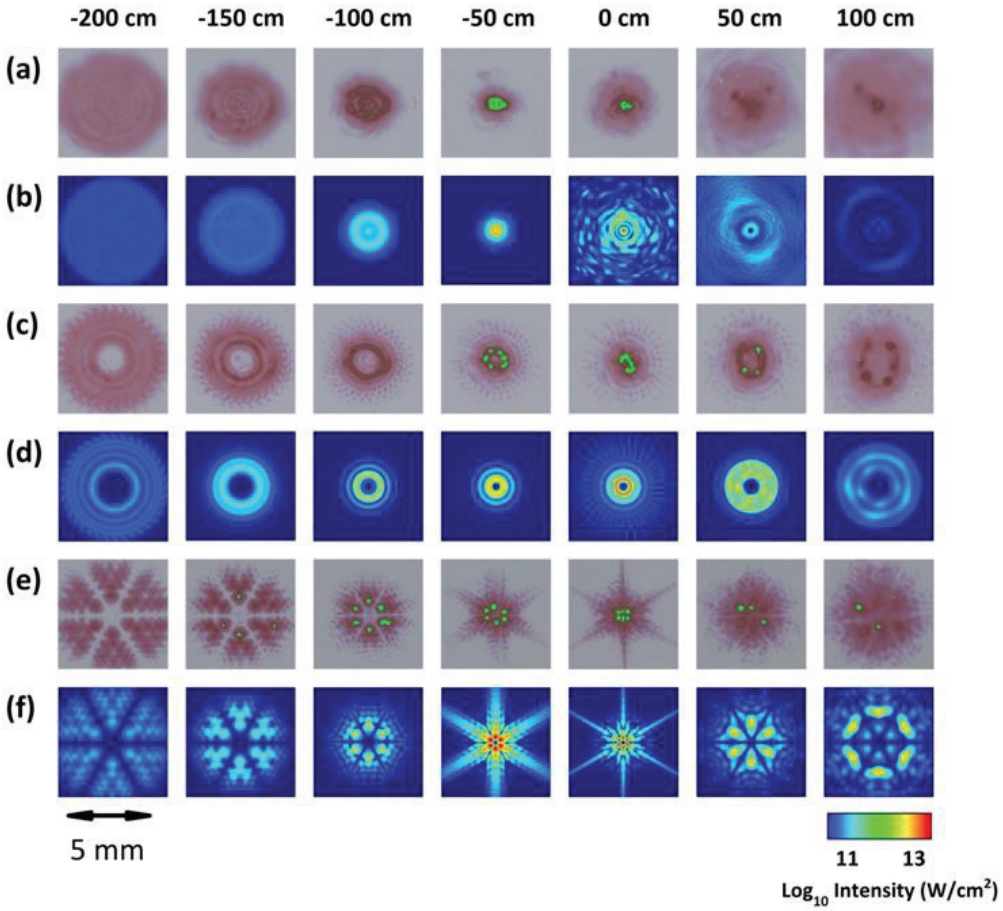

Figure 4.2.1. Beam profile measured along propagation axis *z* on photosensitive paper for a supergaussian beam LG00 (a), a vortex beam LG40 (c) and a 6-sectors beam LG03 (e). The corresponding intensity profiles obtained from numerical simulations are respectively shown in subfigure (b), (d) and (f). The laser pulse propagates from left to right and position z = 0 corresponds to the geometrical focus of the beam.

Figure 4.2.1 shows the evolution of the beam profile along the propagation axis z, obtained by a single shot laser impact on photosensitive paper. The pink areas indicate

moderate laser intensity, while the green areas represent the burned regions of the paper, where the laser intensity exceeds the ionization threshold of air. It should be noted that the response of the paper is not linear with respect to the laser intensity.

In the case of the supergaussian beam (Fig. 4.2.1(a)) filamentation appears about 1 meter before the focus, then a dense bundle of fused filament is observed over 1 meter. This seems to corresponds to the superfilamentation regime, where the fusion of multiple filaments creates a filament with intensity higher than the clamping intensity [16, 18]. After the focus, only a weak classical filament is observed on the axis over one meter.

In the case of the vortex, the filaments appear at z = -50 cm. About 6 filaments are visible at -100 cm, forming a quasi-continuous ring of plasma at the focus. Then this ring diverges and only 3 filaments remain 50 cm after the focus.

In the case of the 6-sector beam, on can see first strong diffraction effects during the linear propagation of the beam. The beam pattern observed at z = - 200 cm results from the diffraction of the beam on the edge of the waveplate sectors and by the circular aperture of the diaphragm. At z = - 150 cm the first filaments appear at the intensity maxima created by the diffraction pattern. Then between -100 cm and 50 cm one can distinguish 6 filaments perfectly aligned on a ring, whose diameter varies between 1.9 mm (at the beginning) and 0.7 mm (at the geometric focus). Note that the size of the filament ring generated by the m4 vortex is very close to the size of the ring of filament produced by the 6-sector beam (Fig 4.2.1 (b) and (d)).

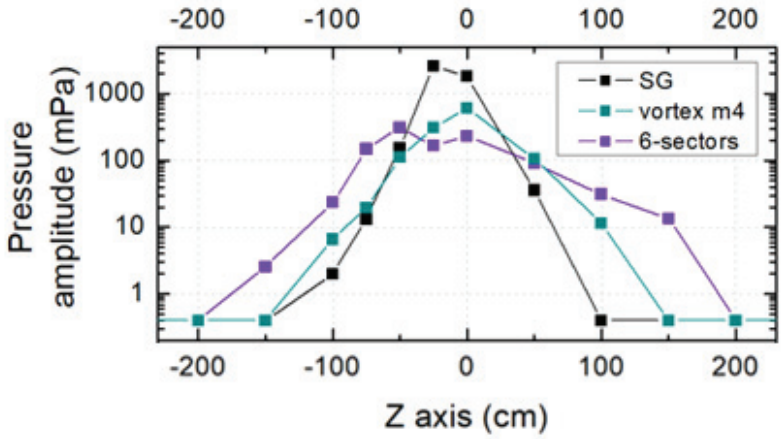

Figure 4.2.2. Amplitude of the lateral pressure wave recorded by a microphone as a function of the position *z* along the laser axis for the three laser modes considered.

Then the energy deposition produced by the filament along z axis has been characterized using transverse acoustic measurement. Indeed, the amplitude of the radial pressure wave produced by the filament is proportional to the density of deposited energy in the filament [19]. Our broadband microphone placed 3 cm away from the beam center has been displaced along z to measure the amplitude of the radial pressure wave emitted by the filament (see Figure 2.2.4 for description). The result is presented in Fig.4.2.2 (a) for the three beams considered. For the supergaussian beam, one can see that the energy deposition is

maximum 20 cm before the focus and that the width (FWHM) of the heated zone is about 150 cm. The vortex case (blue curve) presents a maximum at the focus and a width of 200 cm. Finally, the 6-sectors beam (violet curve) produces a maximum at z = -50 cm and extends over ~250 cm. These results are in good agreement with the burn patterns presented in Fig. 4.2.1 The total deposited energy was respectively of 3.8 mJ for the supergaussian beam, 2.2 mJ for the 6 sectors beam and 1.8 mJ for the vortex.

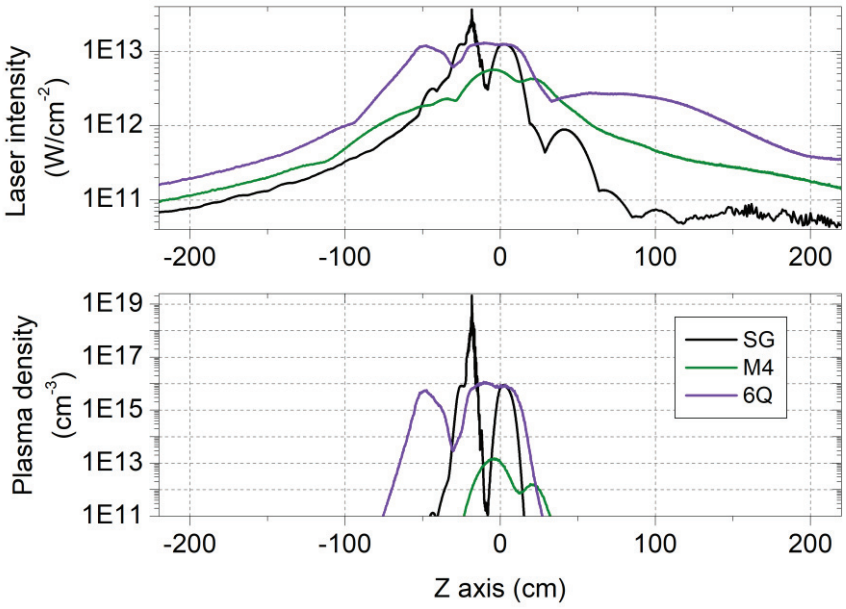

Figure 4.2.3. Calculated laser maximum intensity (a), plasma density (b) as a function of the propagation distance *z* for the three considered laser modes.

Our numerical simulations also gave similar conclusions. The results are presented in Fig. 4.2.3, where the laser maximum intensity and plasma density are plotted as a function of the propagation distance z. Note that the calculated plasma density observed for the vortex beam is relatively low compared to classical filament, with a density between 10^{11} and $10^{13} cm^{-3}$, while the 6-sectors filament exhibit classical features of femtosecond filamentation, such as the saturation of the laser intensity at $10^{13} W/cm^2$ and a peak plasma density around $10^{16} cm^{-3}$. In the case of the supergaussian beam we retrieve an intensity profile corresponding to a superfilamentation regime around the geometrical focus, in agreement with the acoustic measurement presented in Fig. 4.2.2.

4.2.3 Measurement of breakdown voltage reduction by Laguerre-Gaussian filaments

To measure the optimization of breakdown voltage by Laguerre-Gaussian beams, we used the following setup and provided high voltage using a spark gap, as shown in Figure 4.2.4.

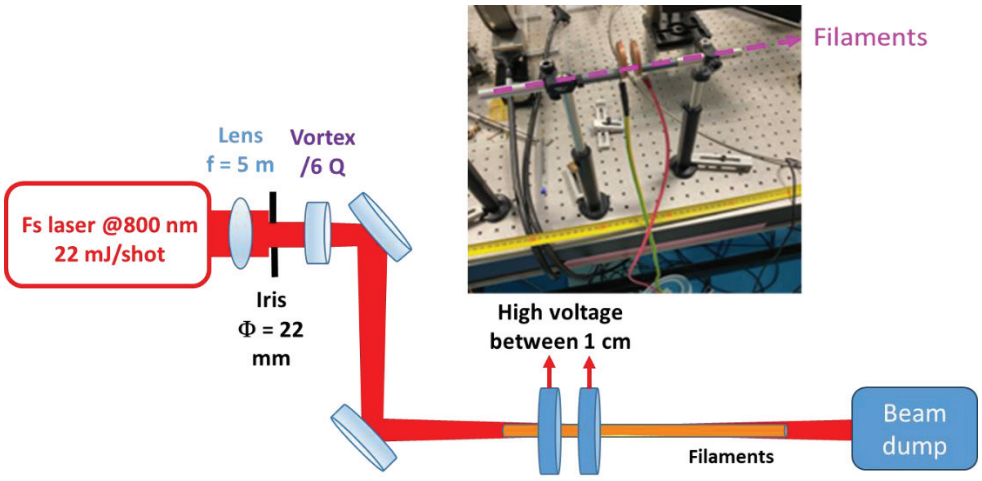

Figure 4.2.4. Setup used to measure the breakdown voltage reduction produced by Laguerre-Gaussian filaments in a spark gap. The inset shows a photograph of the spark gap in operation in the laboratory. The purple dashed lines represent the virtual filaments.

The spark gap was made of two circular disks of copper pierced in the center and separated by 10 mm. The electrodes had a central hole of 3 mm and a diameter of 2 cm. The disks were directly connected to a DC High Voltage power supply (Brandenburg 2807 Alpha Serial II). The breakdown voltage in the presence of the filament has been measured along z by displacing the electrodes along the laser axis. In the absence of laser filament, the breakdown voltage threshold in the gap has been measured to 30 kV. This value of 30 kV/cm corresponds exactly to the natural breakdown field in dry air at 1 bar for a uniform DC electric field [20].

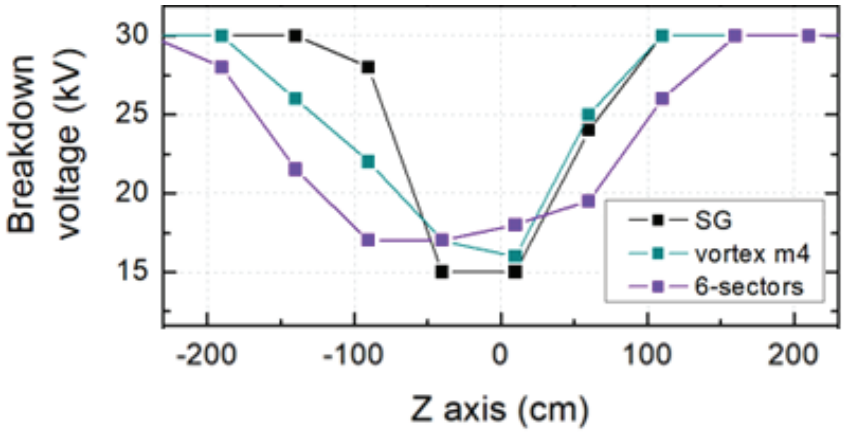

Figure. 4.2.5. Breakdown threshold between two plane electrodes separated by 10 mm measured along propagation axis z for the 3 laser modes.

In the presence of the filament, a decrease of the breakdown electric field up to 50% is observed around the geometrical focus. We note that the shape of the decrease of the breakdown field induced by the three types of filaments presented in Fig. 4.2.5 is very similar to the shape of the acoustic measurement presented in Fig. 4.2.2. The vortex and the 6-sectors

modes produce a longer guiding zone than the SG mode and the longest guiding length is obtained with the 6-sectors beam.

4.2.4 Guiding high-voltage Tesla discharges with Laguerre-Gaussian filaments

Finally, we tested the guiding efficiency of the three beams over decimeter scale discharges with a pulsed Tesla generator delivering voltage pulses of 315 kV. Our setup is illustrated in Figure 4.2.6. The breakdown probability between two pointed electrodes separated by 30 cm and connected to the Tesla generator was measured as function of the position of the electrodes.

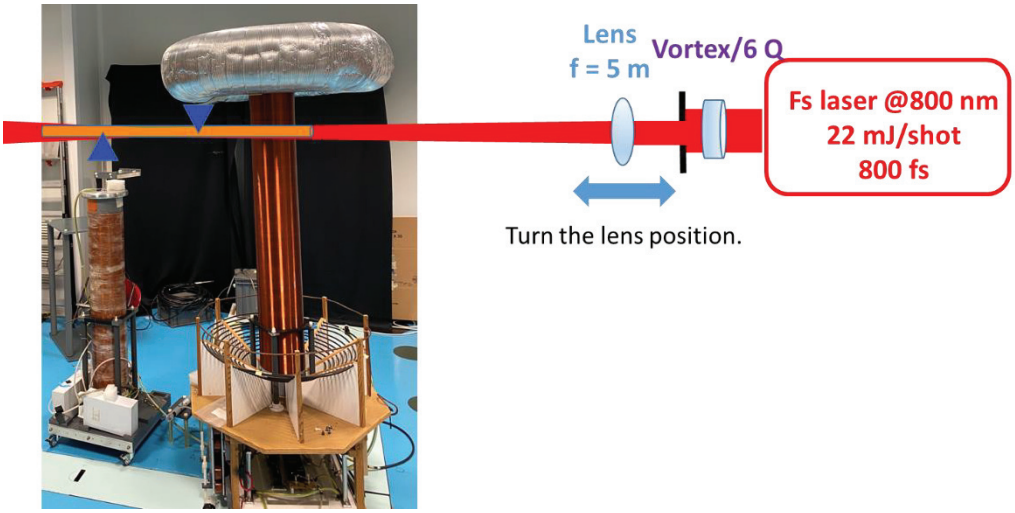

Figure 4.2.6. Experimental setup used to observe the guiding distance of filaments produced by different beams using a Tesla coil.

The result is presented in Fig. 4.2.7, where z corresponds to the position of the first electrode, while the second electrode is 30 cm after (z + 30). In the absence of laser, we observe no discharge between the electrodes (see Fig. 4.2.8 (c)). The breakdown probability is calculated over 10 shots. When the breakdown occurs, we observe either a partial or a full guiding of the discharge (as illustrated in Fig. 4.2.8 (a) and (b)).

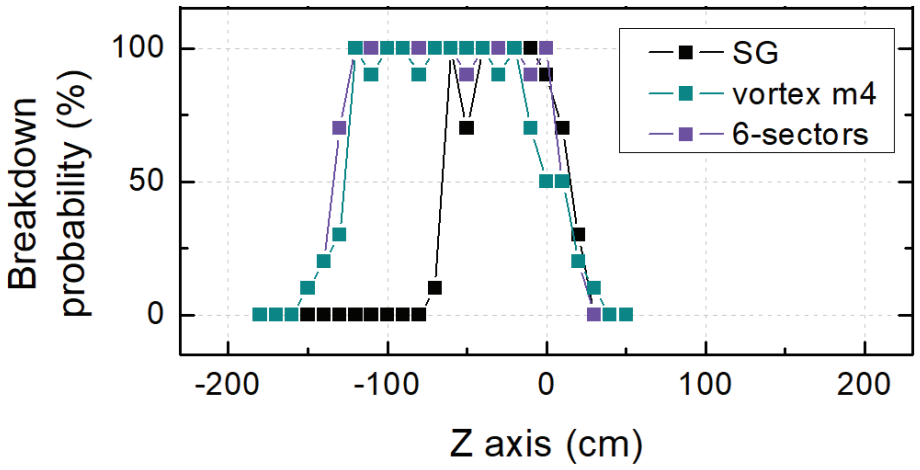

Figure 4.2.7. Breakdown probability between two pointed electrodes separated by 30 cm and connected to the Tesla generator measured as function of the position of the electrodes. Here, z corresponds to the position of the first electrode, while the second electrode is 30 cm after (z + 30).

With the SG beam, a breakdown probability of 100 % is obtained between z = -70 cm and z = 10 cm. This length is twice longer with the LG beams, where it starts at -130 cm. We note that the curves obtained in Figure. 4.2.7 do not match perfectly with the ones in Figure 4.2.3 and 4.2.5. We explain this, first, by the fact that the Tesla gap length is much larger than the sampling resolution of the two other diagnostics used, and second, by the strong non-uniformity of the electric field in the 40 cm gap that produced asymmetric discharge precursors (as seen in Figure. 4.2.8 (c)) and for which the discharge development involves the formation of streamers (as described in section 4.1).

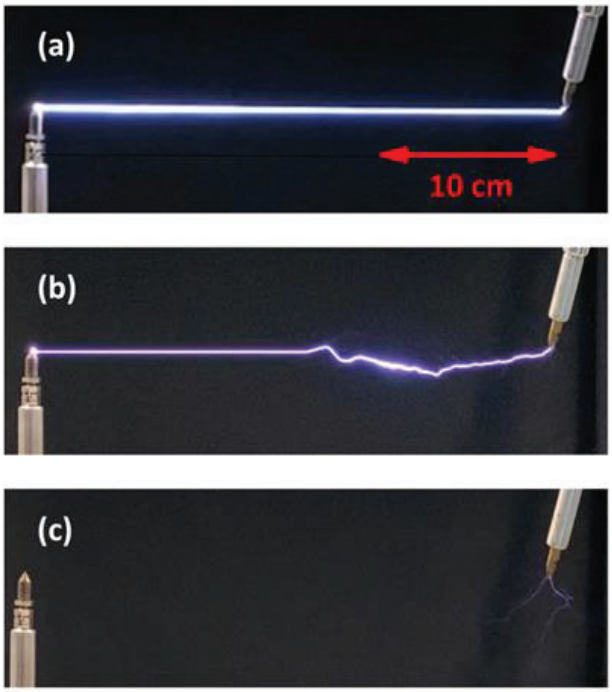

Figure. 4.2.8. Still image of a fully laser guided discharge (a), a partially guided discharge (b) and an event where no spark occurred (c). The distance between the electrodes was 30 cm and the laser energy was 22 mJ.

4.2.5 Limitations of Laguerre-Gaussian beams for discharge guiding

Using different gap distances in the previous experiment, we observed that the advantages of Laguerre-Gaussian (LG) beams for guiding discharges diminish for larger gap distances. To further investigate, we attempted to use LG beams to guide Tesla corona discharges and compared them with super-Gaussian beams. This experiment utilized only one high-voltage electrode without the grounded electrode. By directly observing the plasma columns generated by the high-voltage electrode discharge guided by the filaments, we assessed the guiding length of the filaments.

Figure 4.2.9 shows the corona discharge observed by Wang *et al.* using this method [21]. Figure 4.2.9(a) shows the image of the corona discharge at a voltage of 50 kV in the presence of filaments, and Figure 4.2.9(b) shows the corona discharge at the same 50 kV voltage without laser filaments. Figures 4.2.9(c) and 4.2.9(d) correspond to the streamers and tree-like structures of the corona discharge with and without filaments, respectively.

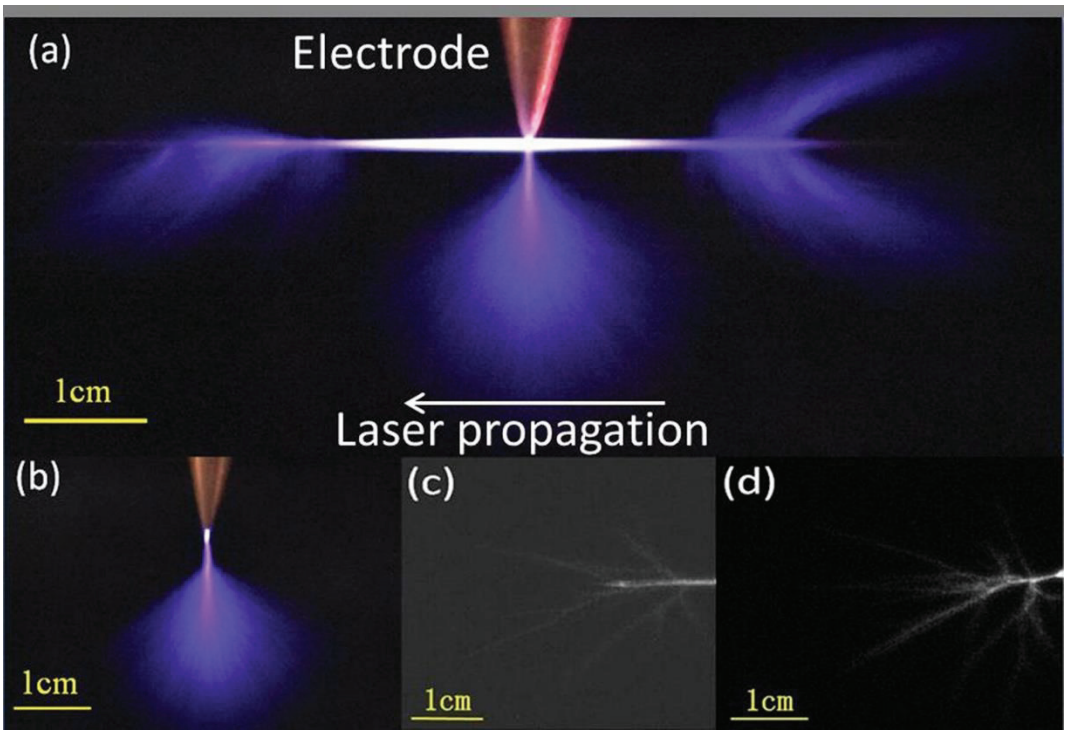

Figure 4.2.9. Illustration of femtosecond laser filaments used to guide corona discharges. (a) Image of corona discharge guided by femtosecond filaments, (b) Corona discharge without filaments, (c, d) Detailed streamer structures in the forward direction of laser propagation for (a) and (b), respectively. The corona discharge voltage and filament pulse energy are 50 kV and 7.5 mJ, respectively. From [21].

When we attempted to observe the advantages of LG beams for filament-guided discharge using this method, we did not observe that they could produce significantly longer guided corona discharges compared to super-Gaussian beams.

We attribute this failure to the absence of continuous superfilaments. LG beams typically generate multiple filaments, which cannot merge due to the presence of OAM. For discharges, the ionization channel often selects one of these multiple filament paths. In our experiments, the plasma density of the multiple filaments produced by LG beams was significantly lower than that of the superfilaments produced by Gaussian beams. This lower density might be insufficient to induce long-distance corona discharge. Additionally, for vortex

filaments, the filamentation process involves rotation [22], which might make corona discharge more challenging. To generate superfilaments using LG beams, very high peak power is required. With current technology, it is difficult to ensure the safety of phase plates at high energy levels. Figure 4.2.10 shows a phase plate that was burned at 100 mJ and 300 fs. Therefore, if we aim to use LG beam-generated filaments to guide longer-distance corona discharges, a feasible solution might be to use higher frequency lasers to enhance the creation of low-density channels. Some studies have reported that these high-repetition lasers can increase the density reduction of such low-density channels by a factor three [23].

Figure 4.2.10. Phase plate damaged by the laser with high peak power. Laser energy was 100 mJ and pulse duration was 300 fs.

4.2.6 Conclusions

We have demonstrated that the use of LG beams with azimuthal phase shift allows the generation of a longer and more uniform bundle of filaments when compared to a laser beam with a flat phase. LG are therefore able to guide electric discharges efficiently over longer distances than gaussian beams.

A current limitation of these Laguerre-Gaussian filaments for the guiding of very long discharges is the damage threshold of the phaseplate that does not allow to exceed a few tens of GW peak power and to produce meter-scale superfilamentation. But the lower plasma density produced by the LG beam could be compensated in future experiments by the use of a kilohertz repetition rate laser for which a permanent low-density channel can be produced.

4.3 Optimizing filamentation and discharges guiding using multifocal phase plates

Using Laguerre-Gaussian beams to generate filaments can effectively extend the discharge guidance distance. However, this method still confines the intense filaments to a range close to the Rayleigh length. If a method can allow to overcome this limitation, it could significantly extend the control range of filament-guided discharges. As discussed in the last part of the previous section, the current technical limitations of the phase plate damage constrain the creation of superfilaments with Laguerre-Gaussian beams. This limitation could become a potential threat in the future when using filamentation to control larger-scale discharges, such as lightning. Is there a way to extend filamentation along the axis while maintaining superfilament intensity?

Concatenated filaments could be used to achieve this goal [24]. In fact, this idea was explored by Polynkin in 2017 [25, 26]. He divided the beam into three parts, each focused separately, and adjusted the lens positions to control the spatial focusing positions of each part of the beam. By using translation stages to control the temporal positions of each part of the beam, he created three cascaded filaments and successfully extended the discharge control range.

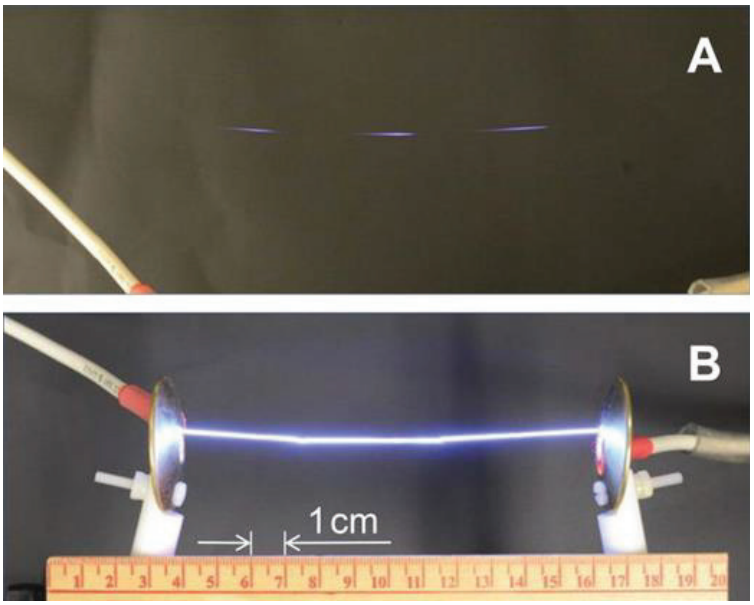

Figure 4.3.1 Polynkin's use of dispersed focusing to generate cascaded filaments (A), successfully extending the controllable discharge range (B) (from [25]).

As discussed in chapter 3.3, using multifocal phase plates can eliminate the need for complex temporal and spatial adjustment systems to generate concatenated filaments.

4.3.1 Generation of cascaded superfilaments using multifocal phase plates

To generate concatenated superfilaments, it is crucial to select an appropriate external focusing and to maximize the incident pulse energy. Limited by the size of the phase plates and the capabilities of ENSTA mobile at the time, we ultimately chose a two-meter external focusing lens and an incident pulse energy of 120 mJ. To protect the phase plates at high energy levels, we opted for an incident pulse duration of 500 fs to generate the cascaded superfilaments.

The results are shown in Figure 4.3.2. We characterized the filaments generated by a standard super Gaussian beam and the filaments generated through the MPM at 120 mJ pulse energy (traditional superfilamentation, and extended superfilamentation), and the filaments generated by a super Gaussian beam at 10 mJ pulse energy (single filament).

We employed two methods to compare these filaments. First, we used a commercial camera (Canon R6) to measure the plasma luminescence of the filaments. A macro lens was used to observe the structure of the filaments, and a zoom lens was used to examine their length. Since plasma luminescence cannot quantitatively measure plasma density, we used a broadband microphone (GRAS Model 46BH 1/4'') to measure the acoustic signals emitted by the filament. The microphone was placed 3 cm below the filaments. As mentioned earlier, this microphone measures the lateral pressure wave generated by the fast laser energy deposition, which is roughly proportional to the density of energy in the plasma.

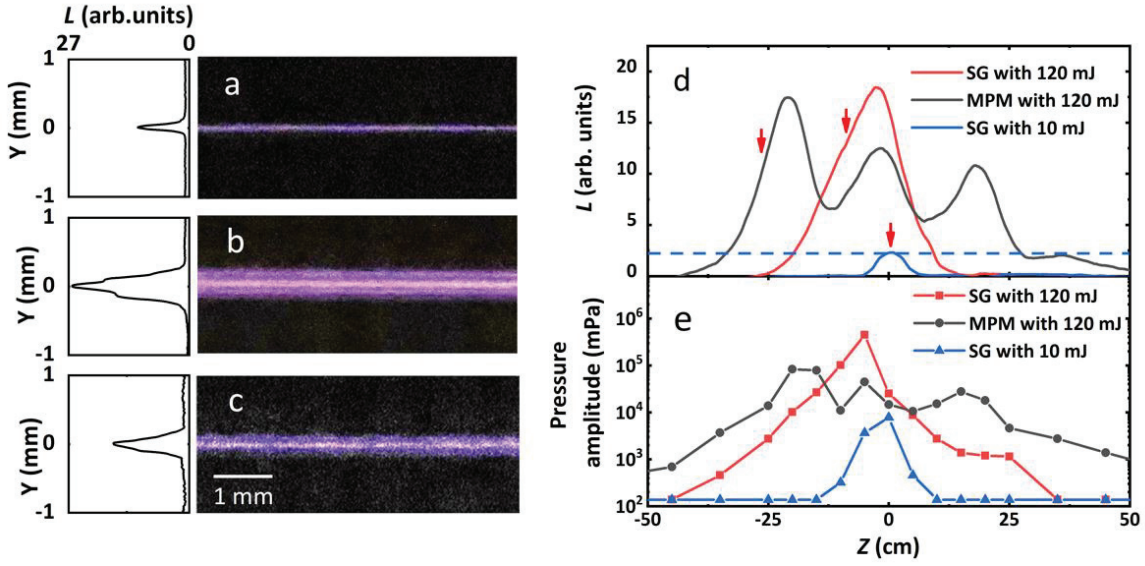

Figure 4.3.2. Comparison between a regular filament, a typical superfilament, and an extended superfilament. a, b, c are plasma luminescence signals measured by a commercial camera with a single laser shot. a: supergaussian (SG) pulse with 10 mJ energy, b: same pulse with 120 mJ, c: same pulse with 120 mJ but with the phase mask. d: axial plasma luminescence *L* integrated over ten laser shots. The red arrows in d correspond to the positions of the measurements in a, b and c. e: amplitude of the radial acoustic wave measured by a microphone positioned 30 mm away from the laser axis for the same cases as in subfigure d as a function of position z

along the laser propagation axis. Position z = 0 corresponds to the geometrical focus of the beam of numerical aperture NA = 0.01. The dotted horizontal line in d gives the magnitude of a clamped plasma.

First, let's focus on the structure of these filaments. Figure 4.3.2(a) corresponds to a standard single filamentation regime. Although the laser power used to generate this filament is still above the critical power, this is the lowest energy for which we can obtain a clear single-shot image of the plasma, and its diameter is still within the range of a single filament. Therefore, we classify this situation as a typical single filament. This single filament corresponds to an electron density of approximately $n \sim 10^{16} e^{-}.cm^{-3}$, with a diameter of less than 100 µm. Subsequently, when the energy was increased to 120 mJ, we observed a very obvious superfilamentation phenomenon. In Figure 4.3.2(b), it can be seen that a very thick filament appeared in the center of the plasma, with a diameter exceeding 200 µm, surrounded by some normal filaments. After adding the multifocal phase plate, as shown in Figure 4.3.2(c), although the intensity of plasma luminescence decreased slightly, the diameter of the filament was still about 200 µm, remaining within the range of a superfilament.

By comparing the length of the plasma luminescence of the filaments, we can draw similar conclusions. In Figure 4.3.2(d), comparing the red curve representing the super-Gaussian beam with the black curve with the multifocal phase plate added, we can see that between z = -15 cm and z = 10 cm, the plasma luminescence signal of the 120 mJ pulse is approximately five times higher than that of the single filament (blue curve). This corresponds to an increase in plasma density, typical of superfilaments. In the presence of the multifocal phase mask, three peaks were observed in the range from z = -25 cm to z = 20 cm, corresponding to the three focal positions. The intensity of the luminescence signal in this range indicates the presence of three merged superfilaments. The acoustic signal measurement presented in Figure 4.3.2.(e) also showed similar results.

4.3.2 Filament-controlled discharge using multifocal phase plates

As mentioned in section 4.2, superfilaments and multifilaments produce very different low-density channels, resulting in different discharge patterns. After confirming the presence of merged superfilaments, we tested the potential of these extended superfilaments to guide corona discharges [21]. Using a setup similar to the one described in section 4.2.4, we employed a pulsed Tesla generator that delivers 315 kV voltage pulses to a sharp electrode. We observed the length of the guided discharge when the tip of the charged electrode came into contact with the filament.

The pointed Tesla electrode was placed at the geometrical focus of the beam. Without laser or with a single filament (10 mJ), we observed only small, erratic streamer discharges of a few centimeters around the electrode, as shown in the figure 4.3.3.

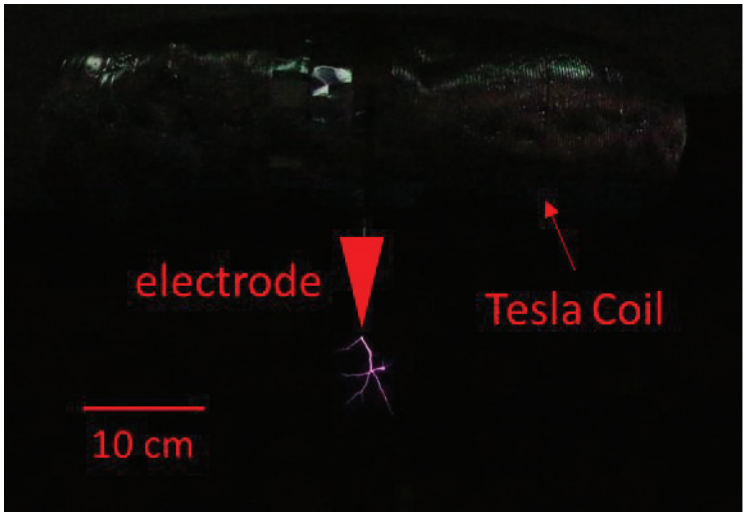

Figure 4.3.3. Corona discharge generated by the Tesla without filaments or with a single filament (10 mJ).

First, Figure 4.3.4 shows the image of the luminescence of the superfilaments (a) and of the extended superfilaments obtained with the multi-focal phase mask (MPM) (b). Images are accumulated over 10 pulses.

In the presence of the high voltage pulse, a guided discharge of approximately 40 cm in length is observed with the superfilament, which is twice the length of the superfilament (Figures 4.3.4 (a) and (c)).

With the phase mask and the high voltage, the extended laser superfilaments produce a guided discharge of 86 cm in length (Figures 4.3.4 (d) and (f)). This confirms the ability of the MPM to extend the discharge guiding length of superfilaments.

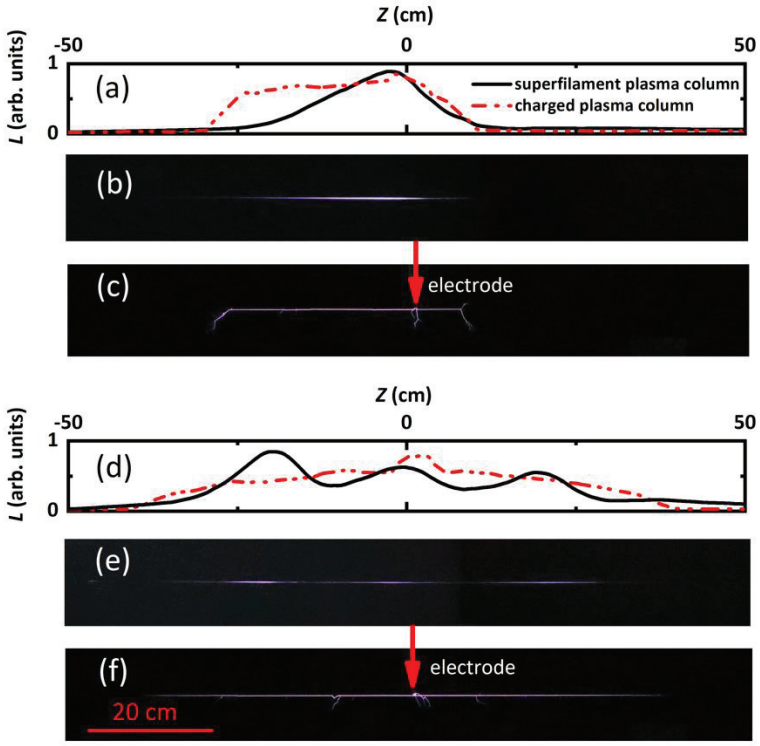

Figure 4.3.4. (a) On axis luminescence signal of the laser superfilament (black curve) and of the guided discharge (red dashed curve) as a function of the propagation distance z recorded over 10 laser shots. (b). Plasma luminescence of a typical superfilament without applied voltage recorded in a single laser shot. (c). Plasma luminescence of a discharge guided by a superfilament recorded in a single laser shot. (d). Same as (a) but with phase mask. (e). Same as (b) but with phase mask. (f). same as c but with phase mask. The laser energy is 120 mJ, and the focusing lens is f = 2000 mm. The pointed electrode is placed at z = 0. The laser is propagating from left to right and the camera is at a distance of 1 m from the plasma.

4.3.3 Conclusions and outlooks

In this section, we successfully extended the length of the superfilamentation by a factor two using a multifocal phase mask, thereby doubling the distance of high-voltage corona discharge guidance in the air. Together with the work discussed in Chapter 3 on air waveguides, we have optimized two atmospheric applications of filaments using this method. We believe that this phase mask method has the potential to be used in atmospheric applications sensitive to the filament plasma length, such as lightning control [1], cloud clearing for optical communications with satellites [27,28], and filament waveguiding over longer distances [29,30].

References

1. A. Houard, P. Walch, T. Produit, V. Moreno, B. Mahieu, A. Sunjerga, C. Herkommer, A. Mostajabi, U. Andral, Y.-B. André, M. Lozano, L. Bizet, M. C. Schroeder, G. Schimmel, M. Moret, M. Stanley, W. A. Rison, O. Maurice, B. Esmiller, K. Michel, W. Haas, T. Metzger, M. Rubinstein, F. Rachidi, and J.-P. Wolf. Laser-guided lightning. Nat. Photonics **17**, 231 (2023).
2. V. A. Rakov and M. A. Uman. Lightning: Physics and Effects. (Cambridge University Press, Cambridge, UK, 2003).
3. R. Fieux, C. Gary, and P. Hubert. Artificially triggered lightning above land. Nature **257**, 212 (1975).
4. D. W. Koopman and T. D. Wilkerson. Channeling of an Ionizing Electrical Streamer by a Laser Beam. Journal of Applied Physics **42**, 1883 (1971).
5. M. Miki, T. Shindo, and Y. Aihara. Mechanisms of guiding ability of CO2 laser-produced plasmas on pulsed discharges. Journal of Physics D **29**, 1984 (1996)
6. M. Rodriguez, R. Bourayou, G. Méjean, J. Kasparian, J. Yu, E. Salmon, A. Scholz, B. Stecklum, J. Eislöffel, U. Laux, A. P. Hatzes, R. Sauerbrey, L. Wöste, and J.-P. Wolf. Kilometer-range nonlinear propagation of femtosecond laser pulses. Phys. Rev. E **69**, 036607 (2004).
7. M. Durand, A. Houard, B. Prade, A. Mysyrowicz, A. Durécu, B. Moreau, D. Fleury, O. Vasseur, H. Borchert, K. Diener, R. Schmitt, F. Théberge, M. Chateauneuf, J.-F. Daigle and J. Dubois, Kilometer range filamentation. Opt. Express **21**, 26836 (2013).
8. B. Forestier, A. Houard, I. Revel, M. Durand, Y.-B. André, B. Prade, A. Jarnac, J. Carbonnel, M. Le Nevé, J. C. de Miscault, B. Esmiller, D. Chapuis, and A. Mysyrowicz. Triggering, guiding and deviation of long air spark discharges with femtosecond laser filament. AIP Advances **2**, 012151 (2012).
9. F. Paschen. Uber die zum Funkenübergang in Luft, Wasserstoff und Kohlensäure bei verschiedenen Drucken erforderliche Potentialdifferenz. Ann. Phys., **273**, 69-96 (1889).
10. L. B. Loeb and J. M. Meek. The Mechanism of Electric Spark (Clarendon Press, Oxford, UK,1941).
11. H. Raether. Electron Avalanches and Breakdown in Gases (Butterworths, London, UK, 1964).
12. S. Nijdam, J. Teunissen, U. Ebert. The physics of streamer discharge phenomena. Plasma Sources Sci. Technol. **29** 103001 (2020).
13. E. M. Bazelyan and Y. P. Raizer. Spark Discharge (CRC Press, Boca Raton, FL, USA, 1998).
14. S. Fu, B. Mahieu, A. Mysyrowicz, A. Houard. Femtosecond filamentation of optical vortices for the generation of optical air waveguides. Opt. Let. **47**, 5228-5231 (2022).
15. T. Wang, S. Bin Ali Reza, F. Buldt, P. Bassène, M. N'Gom. Structured light signal transmission through clouds. J. Appl. Phys. **133**, 043102 (2023)
16. G. Point, Y. Brelet, A. Houard, V. Jukna, C. Milián, J. Carbonnel, Y. Liu, A. Couairon, and A. Mysyrowicz. Superfilamentation in Air. Phys. Rev. Lett. **112**, 223902 (2014).
17. A. Couairon, E. Brambilla, T. Corti, D. Majus, O. de, J. Ramírez-Góngora and M. Kolesik. Practitioner's guide to laser pulse propagation models and simulation. Eur. Phys. J. Spec. Top. **199**, 5–76 (2011).

18. D. Pushkarev, E. Mitina, D. Shipilo, N. Panov, D. Uryupina, A. Ushakov, R. Volkov, A. Karabutov, I. Babushkin, A. Demircan, U. Morgner, O. Kosareva and A. Savel'ev. Transverse structure and energy deposition by a subTW femtosecond laser in air: from single filament to superfilament. New J. Phys. **21** 033027 (2019).
19. G. Point, C. Milián, A. Couairon, A. Mysyrowicz, and A. Houard. Generation of long-lived underdense channels using femtosecond filamentation in air. Journal of Physics B **48**, 094009 (2015).
20. Y. P. Raizer. Gas Discharge Physics (Berlin: Springer) (1991)
21. T.-J. Wang, Y. Wei, Y. Liu, N. Chen, Y. Liu, J. Ju, H. Sun, C. Wang, H. Lu, J. Liu, S. L. Chin, R. Li, and Z. Xu. Direct observation of laser guided corona discharges. Sci. Rep. **5**, 18681 (2015).
22. P. Polynkin, C. Ament, and J. V. Moloney. Self-focusing of ultraintense femtosecond optical vortices in air. Phys. Rev. Lett. **111**, 023901 (2013)
23. P. Walch, B. Mahieu, L. Arantchouk, Y.-B. Andre, A. Mysyrowicz, and A. Houard. Cumulative air density depletion during high repetition rate filamentation of femtosecond laser pulses: Application to electric discharge triggering. Appl. Phys. Lett. **119**, 264101 (2021).
24. S. Tzortzakis, G. Méchain, G. Patalano, M. Franco, B. Prade and A. Mysyrowicz. Concatenation of plasma filaments created in air by femtosecond infrared laser pulses. Appl Phys B **76**, 609–612 (2003).
25. P. Polynkin. Multi-pulse scheme for laser-guided electrical breakdown of air. Appl. Phys. Lett. **111**, 161102 (2017).
26. P. Polynkin, Z. Samsonova, A. Englesbe, A. Lucero, J. Elle, A.Schmitt-Sody. Channeling the dielectric breakdown of air by a sequence of laser-generated plasma filaments. JOSA B **36**-11-3024 (2019).
27. G. Schimmel, T. Produit, D. Mongin, J. Kasparian, and J.-P. Wolf. Free space laser telecommunication through fog. Optica **5**, 1338-1341 (2018).
28. I. Dicaire, V. Jukna, C. Praz, C. Milián, L. Summerer, and A. Couairon. Spaceborne laser filamentation for atmospheric remote sensing. Laser & Photonics Reviews **10**, 481-493 (2016).
29. M. Châteauneuf, S. Payeur, J. Dubois, and J.-C. Kieffer. Microwave guiding in air by a cylindrical filament array waveguide. Appl. Phys. Lett. **92**, 091104 (2008).
30. A. Goffin, I. Larkin, A. Tartaro, A. Schweinsberg, A. Valenzuela, E. W. Rosenthal, and H. M. Milchberg. Optical Guiding in 50-Meter-Scale Air Waveguides. Phys. Rev. X **13**, 011006

Chapter 5

Spatiotemporal control of filamentation ------ Steering Cherenkov terahertz radiation

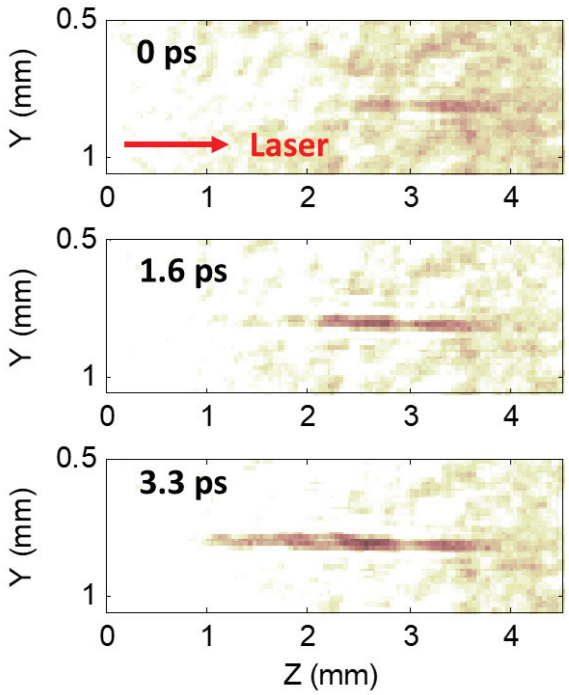

Figure 5.1. Backpropagating plasma generated in air with the flying focus technique.

Several important secondary radiations from femtosecond filament have been observed: terahertz radiation from the plasma, air lasing in the UV and the generation of supercontinuum white light. The generation of terahertz has been widely studied in the perspective of spectroscopy applications due to its capability for remote sensing and to the terahertz characteristics. In this chapter, we discuss our use of a technique called "flying focus" to spatiotemporally control the ionization front of the plasma produced in air, allowing the generation of a pure Cherenkov terahertz radiation with adjustable direction and angle.

5.1 Terahertz radiation generated by laser-Induced plasma in air

Terahertz waves, which refer to electromagnetic waves with frequencies in the range 0.1 THz - 10 THz, have wavelengths on the millimeter scale. As shown in Figure 5.1.1, the terahertz band is situated between the optical and microwave bands, indicating that terahertz research is at the transitional stage between macroscopic electronics and microscopic photonics. For a long time, the research on terahertz waves has been limited due to the constraints of generation and detection technologies, leading to the term "Terahertz Gap." Since the 1980s, with the advancement of electronics, semiconductor technology, and laser technology—especially ultrashort laser pulse technology—the study of terahertz waves has seen significant expansion.

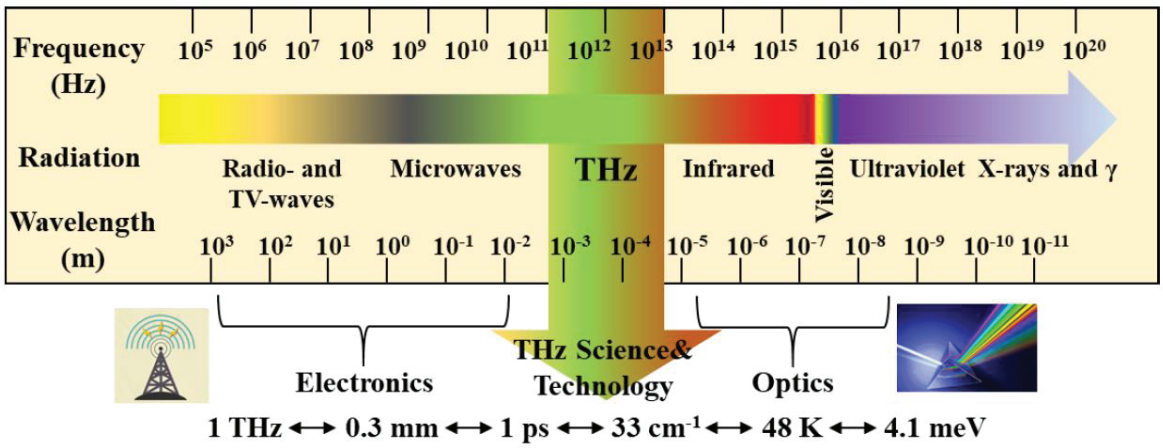

Figure 5.1.1. Frequency and wavelength range of terahertz radiation within the electromagnetic spectrum.

5.1.1 Properties and applications of terahertz radiation

The broad range of terahertz waves [1] goes from 0.1 to 30 THz, with THz as the frequency unit (1 THz = 10^{12} Hz), corresponding to a wavelength range between 0.01 and 3 mm. The electromagnetic radiation angular frequency for 1 THz is 6.28 THz, with an oscillation period of 1 ps, a wavelength of 0.3 mm, and a wavenumber of 33.3 cm^{-1}. The corresponding photon energy is only 4.14 meV, and the blackbody radiation temperature is 48 K.

Due to the unique characteristics of the terahertz band, terahertz radiation exhibits the following optical properties:

1. Firstly, the photon energy of terahertz waves is very low. The photon energy of 1 THz is only 4.14 meV, which is one-millionth of the energy of X-rays. This low energy means that terahertz radiation causes virtually no damage to the biological tissues or the materials inspected, allowing for safe human body scanning. Figure 5.1.2 shows a case where hidden dangerous items are detected with a terahertz body scanner. Additionally, for semiconductors, photons in the meV range do not induce

valence-to-conduction band transitions in the semiconductor electrons. This makes terahertz waves an excellent choice for probing the properties of semiconductors.

Figure. 5.1.2. Image obtained with a terahertz human security scanner for the detection of hidden dangerous goods.

2. Transparency: Many non-polar materials, such as paper, plastic, wood, and textiles are transparent for Terahertz waves. Combined with the previously mentioned characteristic of very low photon energy, this allows for non-destructive testing. Such non-destructive testing has many promising applications in security screening, archaeology, and authentication of ancient artifacts. Figure 5.1.3 shows an example where terahertz imaging is used to authenticate an ancient painting. By analyzing the reflected THz spectrum, information about the painting's canvas and pigments can be obtained, thus helping to verify the painting's authenticity and providing information for any necessary restoration.

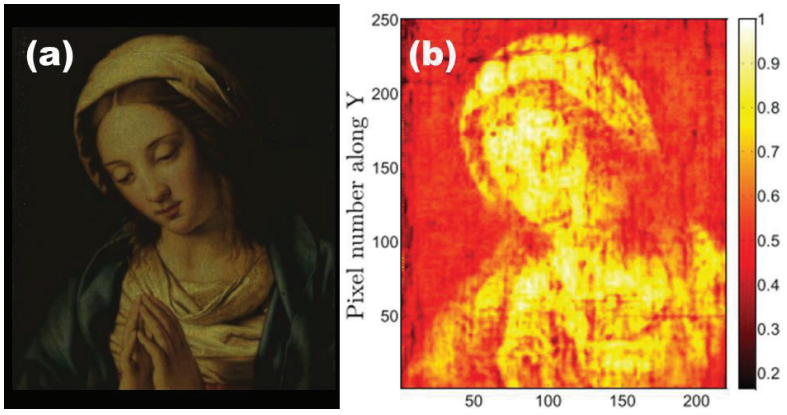

Figure 5.1.3. Analysis of details in an ancient painting using terahertz waves. Taken from [2].

3. The terahertz band coincides with the rotational and vibrational frequencies of many biological macromolecules, making it possible to use terahertz technology to study the properties of these biological macromolecules [3].
4. Resolution: The wavelength of terahertz waves is smaller than that of microwaves, giving terahertz waves higher spatial resolution compared to microwaves. Therefore, terahertz imaging has significant advantages over microwave imaging. Figure 5.1.4 shows a terahertz imaging device developed by Huawei, which provides millimeter-scale imaging of objects inside a sealed paper box [4].

Figure 5.1.4. Terahertz imaging device developed by HUAWEI, achieving millimeter-scale precision imaging of objects inside a sealed paper box. From [4].

5. Terahertz pulses have durations ranging from a few hundred femtoseconds to several picoseconds, and their temporal resolution and ultrafast characteristics may become a valuable complement to ultrafast optics and transient optical research.
6. Large Bandwidth: Typical terahertz radiation bandwidths can range from tens to hundreds of GHz, which is much greater than the carrier bandwidth of microwaves, theoretically providing wireless transmission rates of Tbit/s or higher. This could become a viable method for 6G and the Internet of Things (IoT).

Unfortunately, due to the strong attenuation of terahertz waves by water vapor, many long-distance imaging, detection, and communication applications are limited by the poor transmission of terahertz waves in the atmosphere. Terahertz waves generated locally cannot propagate over long distances in the atmosphere. Therefore, using laser-induced plasma as a terahertz radiation source has become a potential solution, because the plasma can be generated far from the laser source, thus avoiding the absorption of terahertz waves by atmospheric water vapor during transmission.

5.1.2 Terahertz radiation generated by laser-induced plasma in air

In 1993, Hamster *et al.* first demonstrated that laser-induced plasma in gases can generate terahertz radiation [5]. They observed a strong pulsed radiation at THz frequencies produced by a plasma, when laser pulses with an energy of 50 mJ and a duration of 120 fs are tightly focusing in inert gases such as helium or argon at low pressures. They believed that the

cause of the THz wave generation was the acceleration of electrons in the plasma at the focal point by the ponderomotive force at the tail of the laser pulse, resulting in a longitudinal transient current.

Later, Löffer *et al.* demonstrated that applying a static electric field in the plasma region can enhance this THz radiation from plasma by several orders of magnitude [6]. The energy of the THz radiation increased with the external bias electric field. However, this method is limited by the dielectric breakdown threshold of the gas. Subsequently, Cook *et al.* found that the two-color field formed by the collinear transmission of a fundamental field and its second harmonic could drive a transverse photoelectric current to generate stronger THz waves [7]. Kim *et al.* optimized the dispersion between the two-color fields using a dual-wavelength waveplate to make the polarization of the fundamental and second harmonic fields parallel, achieving higher energy THz waves [8]. Later, Koulouklidis *et al.* used mid-infrared two-color field filaments to obtain sub-millijoule level THz pulses, with a conversion efficiency of up to 2.36% and a THz electric field exceeding 100 MV/cm [9].

5.1.3 Transition Cherenkov terahertz radiation

In 2007, D'Amico *et al.* experimentally demonstrated that femtosecond laser filaments emit THz radiation in a narrow cone in the forward direction along the laser propagation axis [10], as shown in Figure 5.1.5. This narrow cone-shaped THz radiation was explained by a theoretical model called transition-Cherenkov radiation. Longitudinal plasma oscillations generated within the filament are the source of the THz radiation, as the oscillation frequency is the plasma frequency. For electron densities typically obtained in filaments, $n_e = 10^{16}\ \mathrm{cm}^{-3}$ to $10^{17}\ \mathrm{cm}^{-3}$ the plasma frequency falls within the THz range.

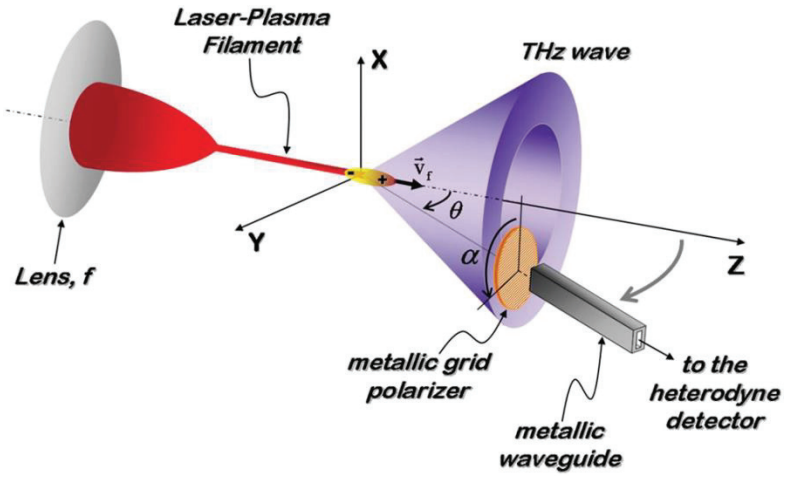

Figure 5.1.5. Terahertz conical emission generated by filaments.

This physical process can be understood by the formation of an electric dipole behind the ionization front of the laser pulse as it propagates in the filament. If the speed of this dipole could exceed the speed of light in the medium, its radiation would correspond to a Cherenkov radiation. However, since the dipole moves at the same speed as the light in air, the emission

efficiency should be zero. Yet, considering the finite plasma length, this does not completely suppress the emission. In this sense, the emission is similar to a transition radiation [11]. Therefore, this THz radiation mechanism generated from filaments has been named transition-Cherenkov radiation [12].

To derive the spectral intensity distribution formula, we follow the theoretical model for transition-Cherenkov radiation as described in [12].

- Spectral current density generated in the plasma

The current density $j_z(\omega)$ in the plasma is the result of the interaction between the laser pulse and the plasma. The current density expressed in the Fourier domain is given by

$$j_z(\omega) = -\frac{e\omega\omega_{pe}^2(\omega+2i\nu_e)}{2m_e c^2\omega_0^2(\omega^2-\omega_{pe}^2+i\nu_e\omega)} I_\omega, \tag{5.1.1}$$

Where e is the electron charge, ω is the angular frequency of the emitted THz radiation, ω_{pe} is the plasma frequency, which depends on the electron density n_e: $\omega_{pe} = \sqrt{\frac{n_e e^2}{\epsilon_0 m_e}}$, ν_e is the electron collision frequency between electrons and neutral particles, m_e is the electron mass, c is the speed of light, ω_0 is the central angular frequency of the laser pulse, I_ω is the Fourier transform of the laser pulse intensity.

- Vector potential and magnetic field

The vector potential A is related to the current density j and describes the electromagnetic field generated by the current. For a current density $j_{\omega,k}$, the vector potential $A_\omega(r)$ at a distance r is

$$A_\omega(r) = \frac{\mu_0 e^{ikr}}{4\pi r} j_{\omega,k}, \tag{5.1.2}$$

where μ_0 is the vacuum permeability, $k = n\omega/c$ is the wave number and n is the refractive index of the medium.

- Electromagnetic emission

For an axial current, the magnetic field B and electric field E are derived from the vector potential A:

$$B_\phi = -ikA_z \sin\theta, \tag{5.1.3}$$

$$E \propto \frac{1}{r}\left(\frac{\mathrm{d}}{\mathrm{d}t} A_z\right). \tag{5.1.4}$$

Here, B_ϕ is the azimuthal component of the magnetic field, A_z is the z-component of the vector potential. θ is the angle with respect to the propagation axis z. E is the electric field, proportional to the time derivative of the vector potential.

- Energy spectral density

The energy spectral density $\frac{\mathrm{d}^2W}{\mathrm{d}\omega\mathrm{d}\Omega}$ represents the energy radiated per unit frequency per unit solid angle. It is given by

$$\frac{\mathrm{d}^2W}{\mathrm{d}\omega\mathrm{d}\Omega} = \frac{cr^2}{\pi\mu_0}|B_\omega|^2 = \frac{|j_z(\omega)|^2}{4\pi\varepsilon_0 c}\frac{\rho_0^4\sin^2\theta}{(1-\cos\theta)^2}\sin^2\left(\frac{L\omega}{2c}(1-\cos\theta)\right). \quad (5.1.5)$$

Here $\frac{\mathrm{d}^2W}{\mathrm{d}\omega\mathrm{d}\Omega}$ is the spectral density distribution, r is the distance between the source and the point of observation, B_ω is the magnetic field strength at frequency ω, $j_z(\omega)$ is the Fourier-transformed current density, ε_0 is the vacuum permittivity, ρ_0 is the radius of the plasma column, θ is the angle with respect to the propagation axis, L is the plasma length.

The formula describes how the energy radiated at a specific frequency and angle is influenced by various factors such as the current density, the geometry of the plasma, and the properties of the laser pulse. The sine functions account for the periodic nature of the radiation and the finite length of the emission zone, while the factors involving ρ_0 and θ describe the spatial distribution of the emitted radiation.

Note that this transition-Cherenkov radiation, compared to a pure Cherenkov radiation, reduces the emission efficiency and makes the radiation more divergent. However, considering the finite length of the source, this does not completely suppress the radiation.

5.2 Spatio-temporal modulation of laser plasma in air using "flying focus"

To produce pure Cherenkov radiation, it is necessary to generate a superluminal charge dipole. How can we generate such superluminal ionization front? In my thesis, we chose the flying focus scheme. A flying focus refers to a beam whose focal position changes over time. In 2018, Froula *et al.* designed a lens system in which different frequencies of light are focused at different positions [13]. When the incident pulse is frequency chirped, the speed and direction of the focus displacement can be controlled, as illustrated in the figure 5.2.1. Note that using an axiparabola [14] or space-time light sheets [15] one can produce similar effects.

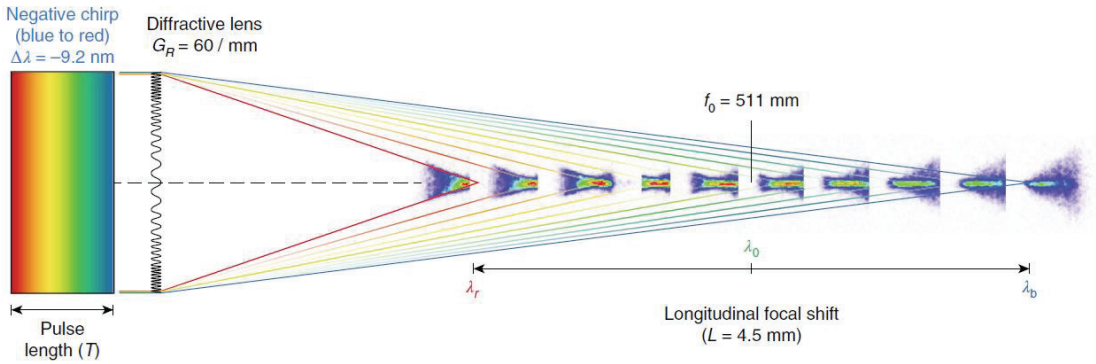

Figure 5.2.1. Schematic diagram of generating a flying focus using a chirped pulse, cited from [13].

5.2.1 Theoretical model of flying focus

Below, we introduce the method for constructing a flying focus. Assume a lens that can produce a dispersed focusing with a focal length of f_0. The focal positions for the longest wavelength λ_r and the shortest wavelength λ_b differ by L_0, given by:

$$L_0 = \frac{f_0 \Delta\lambda}{\lambda_0} = \frac{f_0(\lambda_r - \lambda_b)}{\lambda_0}. \tag{5.2.1}$$

By introducing a laser pulse with a temporally varying wavelength, the focus will move at a speed $v(z) = \frac{dz}{dt}$, where dz is the distance between the focal points of two wavelength separated by $\delta\lambda$, $dt = d\tau + \frac{\mathrm{dz}}{\mathrm{c}}$ is the time it takes for the two wavelength to reach their respective foci, $d\tau$ is the time interval between the two colors within the chirped laser pulse, and c is the speed of light.

By changing the chirp of the laser beam, the time at which the different colors reach the focus can be varied, thereby controlling the focal speed. In this case, the focal speed is given by the following formula

$$v(z)/c = \left[1 + \left(\frac{\mathrm{d}\lambda}{\mathrm{d}\tau}\right)^{-1}\left(\frac{\mathrm{dz}}{\mathrm{d}\lambda}\right)^{-1} c\right]^{-1}. \tag{5.2.2}$$

Using this formula, we can calculate the speed of the flying focus generated by a lens with a fixed chromatic dispersion. In Figure 5.2.2 we present the speed of the flying focus produced by a custom diffractive lens, as calculated by Froula D.H. *et al.* [13]. It can be seen that they generated superluminal flying focus in both the forward and backward directions relative to the laser propagation. If the flying focus can control the ionization front of plasma in air, we have the opportunity to produce superluminal ionization with controllable direction and speed, thereby generating pure Cherenkov radiation of terahertz with controllable emission angles.

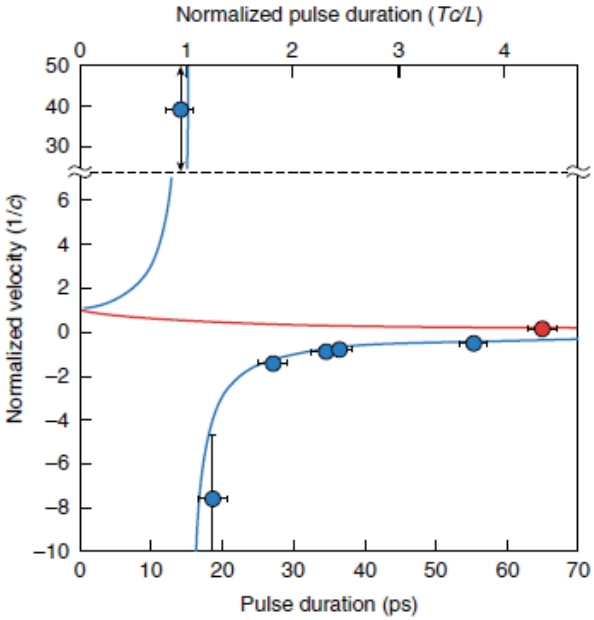

Figure 5.2.2. Speed of the flying focus generated by a custom diffractive lens, as calculated by Froula D.H. *et al.,* for different incident pulse durations. The red line represents the speed for a positive chirp, and the blue lines represent the speed for a negative chirp. From ref. [13].

Note that this type of flying focus has already been proven to be beneficial in laser wakefield acceleration [16], producing beam focuses that match the accelerating electrons. It has also been used to generate photon acceleration [17] or to improve phase-matching in x-ray lasers [18].

5.2.2 Custom diffractive lens and plan convex refractive lens to generate flying focus

First, we measured the spectrum of the output pulse from the ENSTA mobile laser system. As shown in Figure 5.2.3, the pulse has a central wavelength of 790 nm and a full width at half maximum (FWHM) of 18 nm.

In our experiment, we used two focusing optical elements to generate the flying focus. One is a custom diffractive lens from Holo/or with a focal length $f_0 = 30\,\mathrm{cm}$. The other is a plan convex refractive lens (NL) with a focal length of $f = 30$ cm. Both lenses have a calibrated chromatic aberration. The diffractive lens was designed to produce chromatic aberration with

a focus at 30.1 cm for the 780 nm component and 29.9 cm for the 800 nm component of the spectrum. With the normal lens, the 780 nm and 800 nm components were focused at 30.06 cm and 29.94 cm respectively.

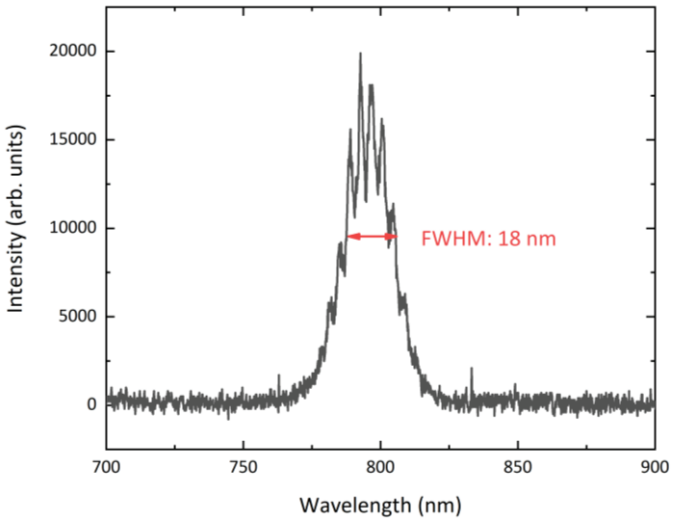

Figure 5.2.3. Spectrum of the output beam of the Enstamobile laser.

Using the above data, we can calculate the flying focus speeds generated by these two lenses, as shown in Figure 5.2.4. Figure (a) shows the calculated flying focus speed for the plan convex refractive lens (NL) as a function of the laser pulse duration T, while Figure (b) shows the calculated flying focus speed for the diffractive lens (DL). In both figures, the red lines represent the speed curves for a positive chirp, and the black lines represent the speed curves for a negative chirp. It can be observed that for both lenses, the flying focus speed decreases as the pulse width increases when the chirp is positive, while for a negative chirp the velocity curve diverges rapidly and change sign .

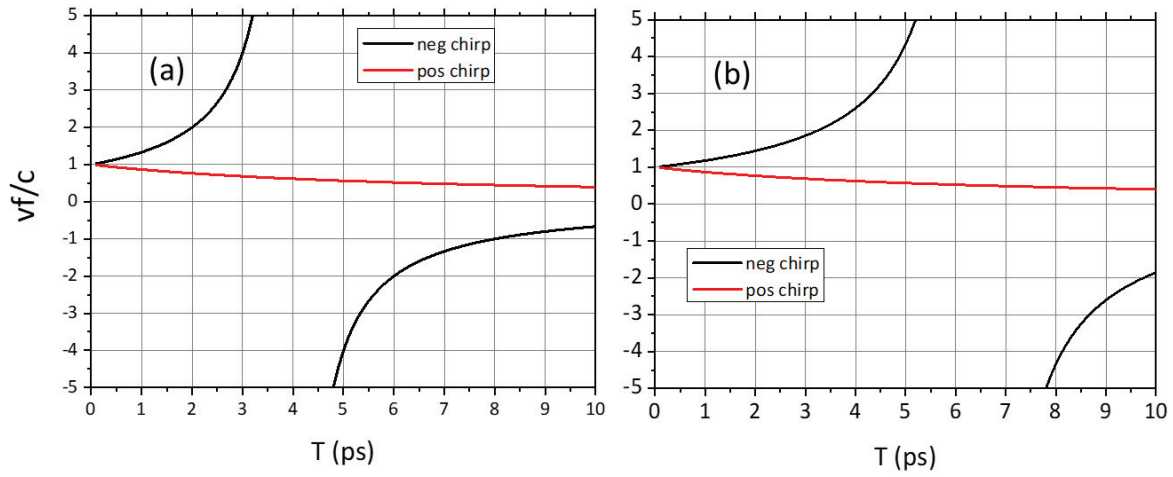

Figure 5.2.4. Calculated flying focus speeds for the normal refractive lens (a) and for the diffractive lens (b). The red lines represent the speed curves for positive chirp, and the black lines represent the speed curves for negative chirp.

5.2.3 Controlling the plasma ionization front using flying focus

This section is taken from my article [ArXiv 2407.18579]. After calculating the velocity of the flying focus, we attempted to control the ionization front of the plasma using the flying focus. The setup used to measure the plasma generation process is shown in Figure 5.2.5. We used an input energy of 11 mJ to generate the plasma in air with input pulse durations ranging from 50 fs to 8 ps. To monitor the velocity of the ionization front of the plasma string, a probe beam was sent perpendicularly to the plasma (see figure 5.2.5). This probe beam was a sample of the amplified beam extracted after the last amplifier and sent to an external compressor. It had a fixed pulse duration of 50 fs and an energy of a few nJ. The probe passed through the plasma and was imaged on a CMOS camera or a wavefront sensor to perform time-resolved diffractometry or interferometric imaging of the plasma channel.

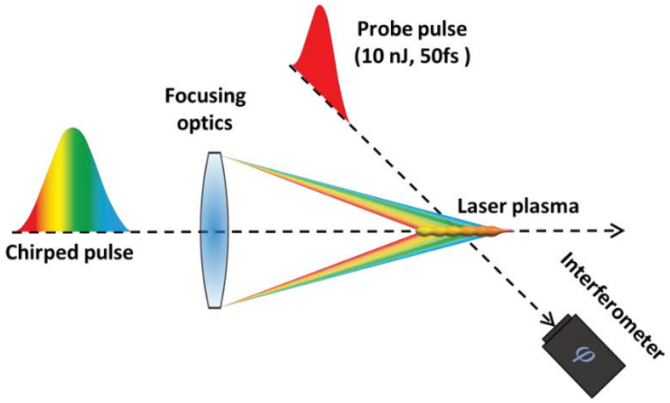

Figure 5.2.5. Experimental setup for time-resolved plasma imaging.

We characterized the displacement of the laser-induced ionization front with transverse diffractometry. An example of diffraction images obtained with the normal lens at delays of 0, 1.6 and 3.3 ps is shown in FIG. 5.2.6. One can see that the plasma is developing toward negative *z*, corresponding to a backward propagation.

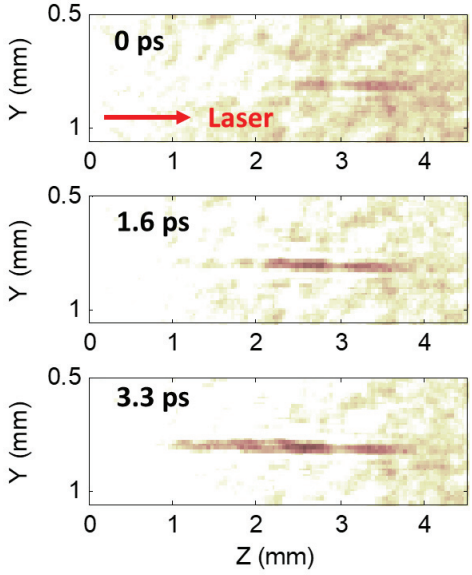

Figure 5.2.6. Shadowgraphy images of the plasma for 3 delays for a negatively chirped pulse of 6.4 ps duration.

By analyzing the time-resolved plasma images obtained for different pulse durations with positive and negative chirps, we can determine the trajectory of the plasma ionization front, as shown in Figure 5.2.7. We observed a negative velocity for pulse durations τ_{las} = -8 and -6.4 ps (the sign of τ_{las} accounts for the sign of the laser chirp C), a velocity $v = c$ for the 50 fs pulse, and a superluminal velocity for τ_{las} = -2.6 ps. For the diffraction lens, we observed that at τ_{las}= -8.7ps and -8ps, the velocities are negative and superluminal.

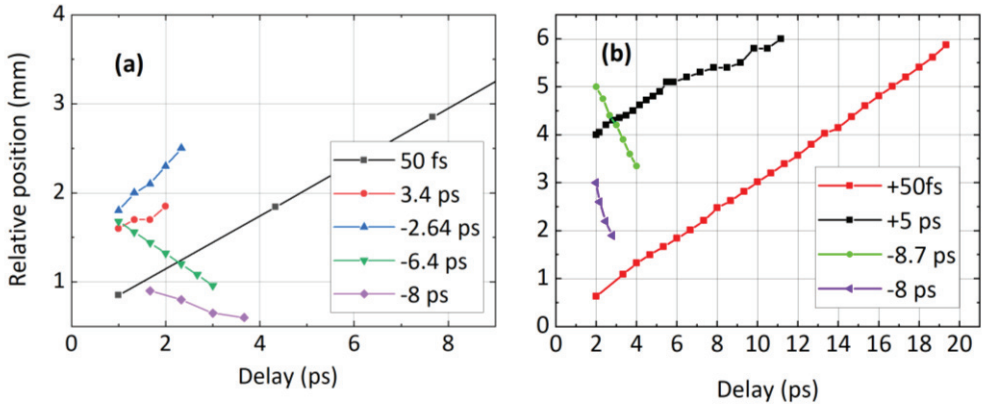

Figure 5.2.7. Measured position of the ionization front as a function of the delay Δt for different pulse durations using the normal lens (a) and the diffractive lens (b).

We can now compare the measured speeds of the ionization front with the theoretical speed of the flying focus as shown in Figure 5.2.8. The points represent the measured ionization front speeds derived from Figure 5.2.7. It can be observed that the ionization front velocities are in very good agreement with the flying focus speeds.

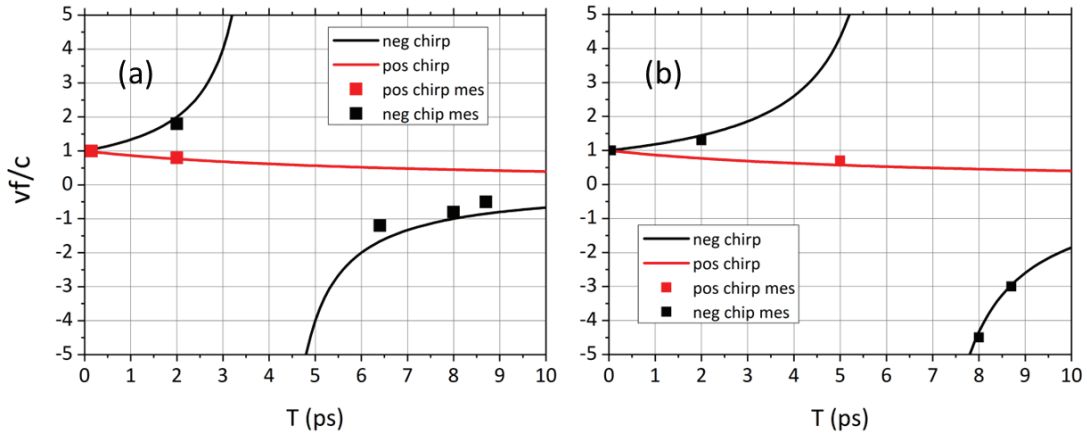

Figure 5.2.8. Ionization front velocities obtained from Figure 5.2.7 for the different pulse durations with the normal lens (a) and the diffractive lens (b). The continuous line shows the theoretical value of *v* based on the flying focus model. Black color corresponds to negative chirp *C* and red color to positive chirp *C*.

5.3 Steering laser-produced THz radiation in air with superluminal ionization fronts

After we determined that the ionization front of a plasma in the air could be controlled by a flying focus, we attempted to measure the terahertz radiation produced by this plasma. To characterize the THz emission pattern a terahertz heterodyne detector at 0.1 THz with 40 mm aperture was mounted on a rotating stage 50 cm away from the plasma, as shown in figure 5.3.1.

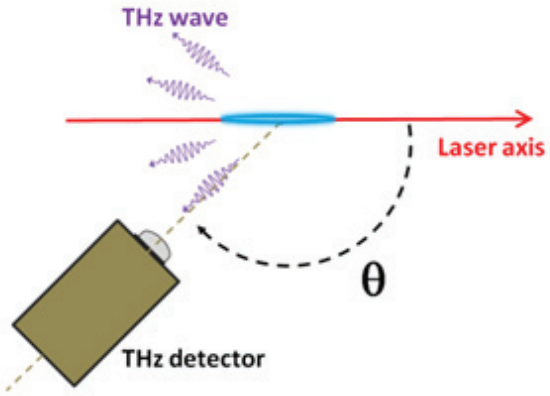

Figure 5.3.1. The radiation from the plasma string at 0.1 THz is measured as a function of angle θ using a heterodyne detector.

5.3.1 Terahertz angular distribution produced by different ionization front velocities

Figure 5.3.2 shows the measured radiation pattern at 0.1 THz from the plasma string for the different pulse durations considered previously, corresponding to subluminal, luminal, and superluminal velocities of the ionization front v. The input energy of the laser was fixed to 11 mJ, and we measured an average plasma length of ~1 mm for the normal lens and 3 mm for the diffractive lens, except for the Fourier transform limited pulse that was two times longer. The results are presented in Figure 5.3.2.(a) and (b) for the normal and the diffractive lens, respectively. In every case, we measured conical emission. For $v = c$, the maximum emission is close to 30°, while for high velocities, the angle of the emission is close to 90°. We also note that for negative velocities, the maximum THz emission is in the backward direction.

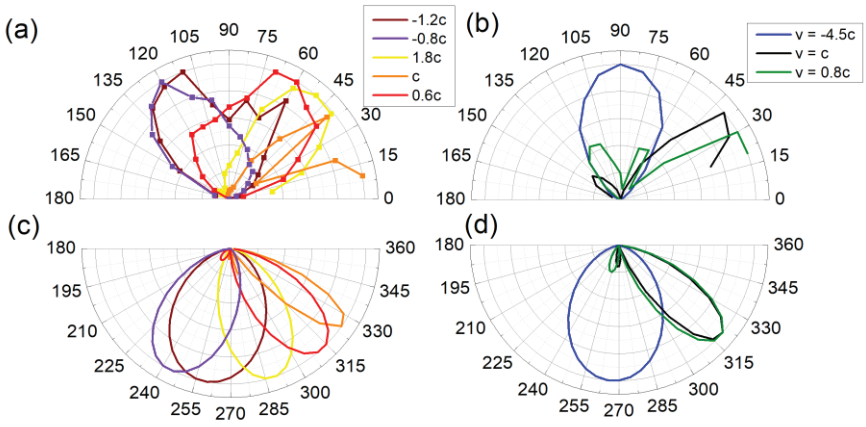

Figure. 5.3.2. Measured THz angular distribution for different ionization front velocities *v* with the normal lens (a) and the diffractive lens (b). Corresponding calculated angular distributions are presented in (c) and (d). All diagrams are normalized and θ = 0 corresponds to the laser propagation direction.

The theoretical model of THz emission from a short laser pulse propagating in a plasma filament was developed from equation (5.1.5). It includes two main elements: the evaluation of the amplitude and the temporal shape of the charge density distribution left behind the laser pulse and the evaluation of the electromagnetic emission from that moving charge propagating at the speed of light *c*. Since the plasma is neutral, the total electric charge in the wakefield is zero, but because of the different mobility of electrons and ions, there is a charge separation, which can be considered a flying dipole. In the equation (5.1.5), *v* = c and the true Cherenkov emission is forbidden, but electromagnetic emission is still produced because of the finite length of the plasma filament. The theoretical approach can be generalized to a superluminal light velocity if the light velocity c is replaced by the ionization front velocity v given by equation (5.2.2). Consequently, equation (5.1.5) for the spectral intensity of electromagnetic emission in a solid angle $d\Omega$ should then be rewritten as follows:

$$\frac{d^2W}{do\, d\Omega} = \frac{q_{\mathrm{las}}^2\omega^2L^2}{4\varepsilon_0c^3}\exp\left(-\frac{\omega^2\tau_{\mathrm{las}}^2}{2}\right)\frac{\omega^2(\omega^2+4\nu_e^2)}{\left(\omega^2-\omega_{\mathrm{pe}}^2\right)^2+\nu_e^2\omega^2}\,\mathrm{sinc}^2\left(\frac{\omega L}{2c}(\cos\theta - c/v)\right)\sin^2\theta. \qquad (5.3.1)$$

Here $q_{\mathrm{las}} = er_{\mathrm{ch}}^2\omega_{\mathrm{pe}}^2\tau_{\mathrm{las}}I_{\mathrm{las}}/4m_ev^2\omega_{\mathrm{las}}^2$ is the effective dipole charge created by a laser pulse with intensity I_{las}, frequency ω_{las}, and duration τ_{las}; ω_{pe} is the electron plasma frequency in the laser-created channel of radius r_{ch} and length L; m_e and e are the electron mass and charge, ν_e is the electron collision frequency, θ is the emission angle with respect to the laser propagation direction, and ε_0 is the vacuum dielectric permittivity. The spectral distribution of the emission is controlled by two factors in this expression: the exponential factor represents the spectral distribution of laser pulse intensity, which is assumed to have a Gaussian temporal profile, and the Lorentzian term containing the plasma frequency and collision frequency, which describes the plasma response with a maximum of emission at the plasma frequency. Finally, the *sinc* function describes the Cherenkov effect with the cone emission angle defined by the resonance condition, $\cos\theta = c/v$. For $v \sim c$, we retrieve the transition-Cerenkov radiation observed in the equation (5.1.5). In this case, the maximum angle of emission is given by $\theta = (\lambda/L)^{1/2}$.

Using equation (5.3.1), we calculated the theoretical angular THz distributions for each measured cases in Figure 5.3.2 The plasma diameter, length, and density were measured using transverse interferometry [19,20]. We found r_{ch} = 50 µm, a plasma density ρ varying from 3×10^{17} cm^{-3} to 10^{18} cm^{-3}, and a plasma length L varying from 0.8 mm to 6 mm depending on the pulse duration. We considered a laser intensity in the filament of 5×10^{13} W/cm^2 [21] and a collision frequency of 6×10^{12} s^{-1} [22]. The results presented in FIG. 5.3.2(c) and (d) are in good agreement with the measurements.

5.3.2 Terahertz Spectroscopy

Since our detector can only detect signals at 0.1 THz, it cannot give a terahertz spectrum. Therefore, using this model, we also calculated the THz spectrum and the influence of the plasma electronic density ρ on this spectrum. As shown in Figue 5.3.3, the THz spectrum is very broad, covering several terahertz. The maximum corresponds to the plasma frequency, and in the case of a laser pulse duration of 100 fs, we observe a maximum THz emission for a plasma density of 10^{17} cm^{-3} because the plasma oscillations period matches the laser pulse duration.

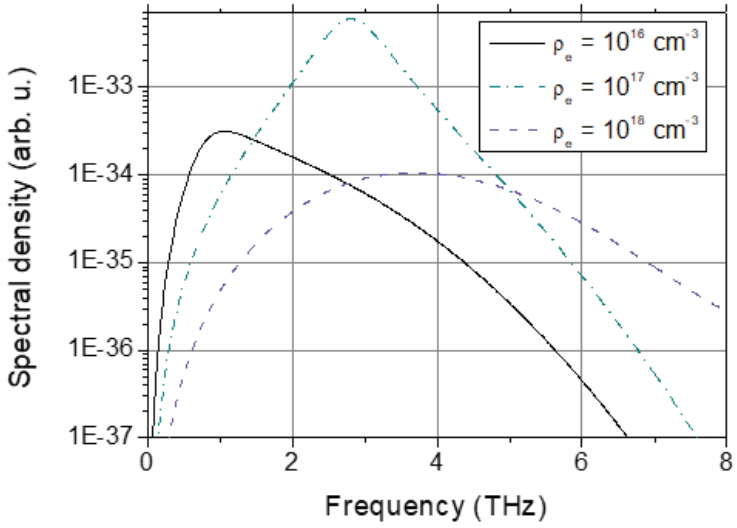

Figure 5.3.3. Calculated THz spectrum for three different plasma densities ρ considering a laser pulse duration τ_{las} = 100 fs.

5.3.3 Pure Cherenkov radiation produced by superluminal ionization

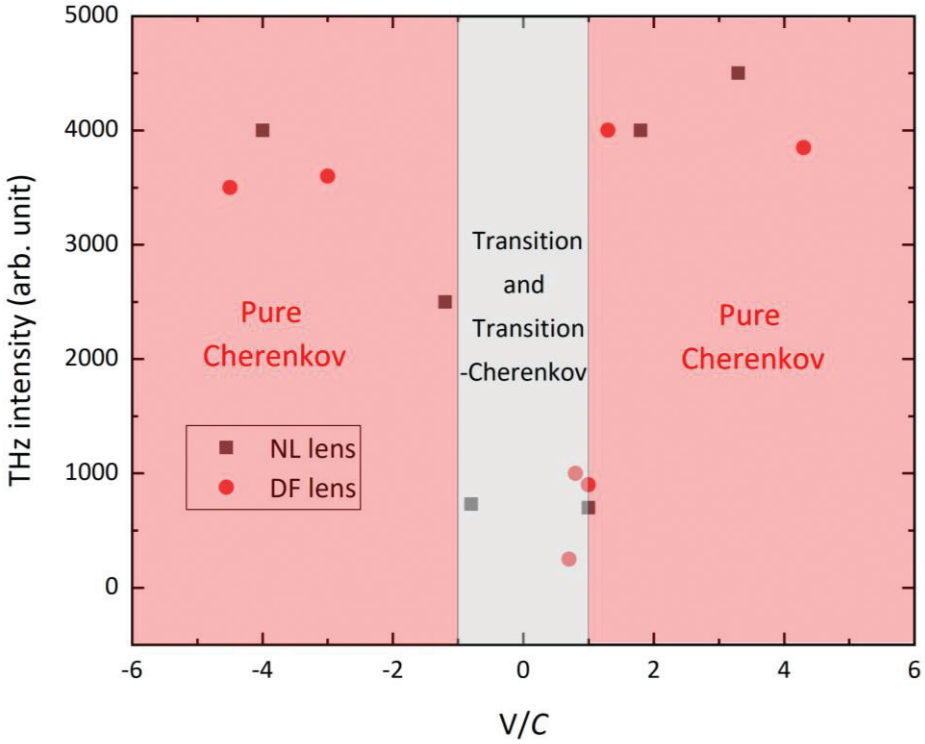

Figure 5.3.4. Comparison of terahertz signal intensity measured at 0.1 THz for different ionization front velocities *v*. The black points are from the normal lens (NL). The red dots come from the diffractive lens (DF).

We studied the terahertz signal intensity generated by different ionization front velocities, as shown in Figure 5.3.4. The grey area corresponds to transition and transition-Cherenkov radiation. The red area corresponds to Pure-Cherenkov radiation($V > C$). It can be seen that pure Cherenkov radiation produces a stronger terahertz signal. This signal is approximately ten times stronger than the transition-Cherenkov signal.

We also studied this effect using the theoretical model. Using equation (5.3.1), we calculated the angle for maximum THz emission as a function of v/c (black curve in Figure 5.3.5(a)) in the range [-8; +8]. Figure 5.3.5(b) also presents the total THz energy radiated by the plasma. For $v = c$, we retrieve the transition-Cerenkov radiation observed in [10]. In this case, the maximum angle of emission is given by $\theta = (\lambda/L)^{1/2}$. When we decrease the velocity of the front below c, the angle of emission converges to 90°, and the radiated energy decreases. It corresponds then to a coherent transition radiation [23]. On the contrary, when $v > c$, the angle of emission progressively increases as the radiated energy. For $v > 1.5c$, the curve perfectly matches the theoretical angle for Cherenkov emission given by $\theta = \arccos\left(\frac{c}{v}\right)$ and plotted as a blue continuous line in Figure 5.3.5(a). Typical angular THz distribution for subluminal, luminal, and superluminal velocities are plotted in Figure 5.3.5(c). We can see that for $v = 1.8c$, all THz frequencies are emitted in a very narrow cone. It is instructive to compare these simulation results with those obtained with a flying focus in a

two-color laser scheme. In that latter case, the THz radiation is maximized along the propagation axis [24].

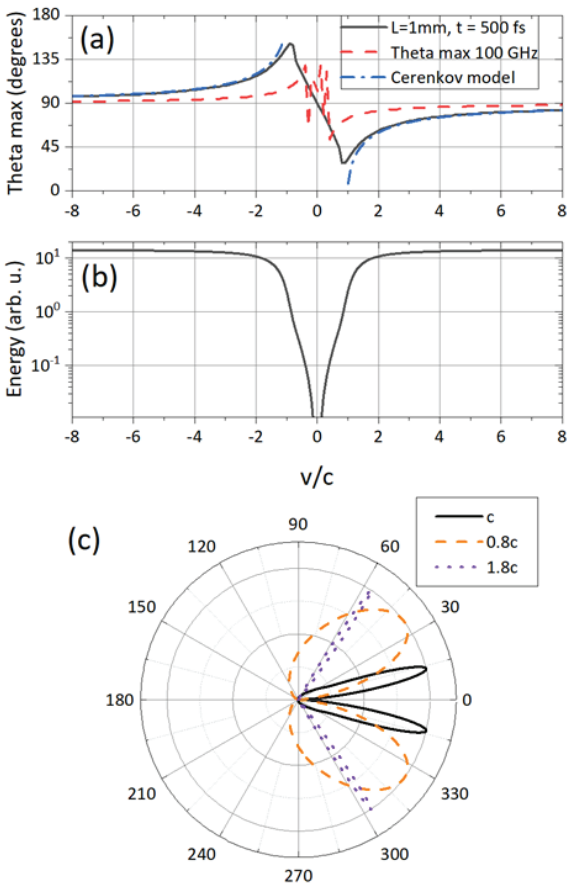

Figure. 5.3.5. (a) Calculated angle for maximum THz emission for the full spectrum (black curve), for the 100 GHz component (red curve) and for a Cerenkov radiation (blue curve) as a function of the ionization front velocity $\frac{v}{c}$. (b) Calculated THz energy as a function of the ionization front velocity. (c) Calculated angular distribution for three different values of v for the full THz spectrum.

5.4 Conclusion and outlook

5.4.1 Conclusion

We have demonstrated that THz radiation emitted by a short filament in air can be tuned to any direction. It requires a simple experimental set-up consisting of a focused short laser pulse from a chirp-controlled laser system with either a normal or a diffractive lens. Forward and backward superluminal ionization fronts velocities v of the generated plasma string can be achieved. With superluminal ionization velocities $v > c$, the THz energy is increased by an order of magnitude compared to the transition-Cherenkov radiation obtained with $v = c$, and all frequencies are emitted along a narrow cone at a large angle.

5.4.2 Outlook

We believe that the ability of this THz source to emit backward or around 90° could be very useful for remote detection [25], or THz imaging [26], since the THz radiation is well separated from the intense laser pulse.

We are currently trying to use this terahertz source to remotely measure an electric field, since the electrostatic field can enhance the THz yield [6,27]. Our experimental setup is shown in Figure 5.4.1. We generate a plasma with a controllable ionization front between two high-voltage electrodes as shown in the upper right corner of Figure 5.4.1. We then measure the terahertz yield at different angles and for different applied voltages.

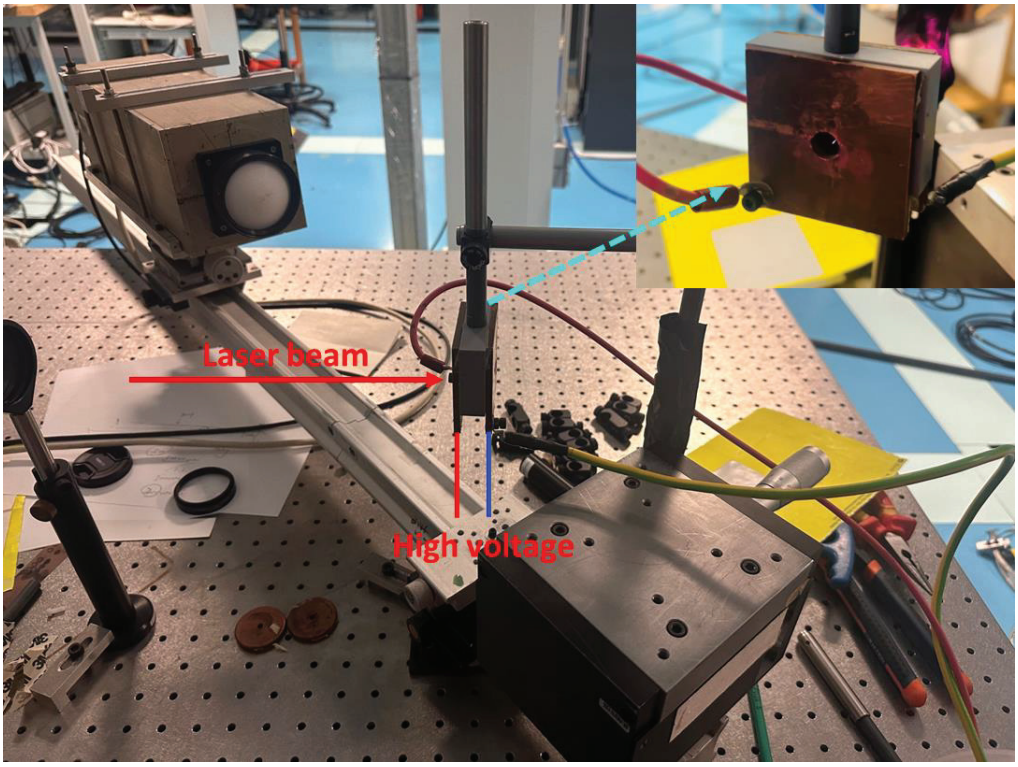

Figure 5.4.1. Experiment setup for detecting remote electric fields through 90° THz source.

Our preliminary experimental results are shown in Figure 5.4.2. As can be seen from Figure 5.4.2, increasing the external electric field leads to a strong increase of the terahertz signal yields. This means we can remotely detect external electric fields using this terahertz signal. In the future, we will try to optimize this experiment.

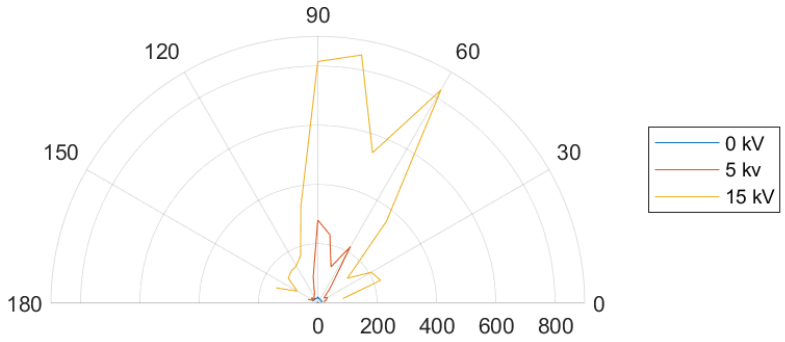

Figure 5.4.2. Terahertz signals generated by different external electric fields. We used a diffractive lens to generate a plasma with a pulse duration of 8 ps, negative chirp, and pulse energy of 11 mJ.

In addition, this method could be employed in combination with a coherent combination of multiple filaments [28]. Such THz emission could also be obtained in the laboratory at longer or shorter wavelengths with the same flying focus technique by changing the plasma density using different gases.

References

1. Y.S. Lee. Principles of terahertz science and technology. Springer, 2009.
2. J. Dong, A. Locquet, M. Melis, D.S. Citrin. Global mapping of stratigraphy of an old-master painting using sparsity-based terahertz reflectometry. Scientific Reports **7** 15098 (2017).
3. F. Wang, M. Cai, Y. Liu. Application of THz time-domain spectroscopy in DNA identification. Infrared Technology **38** 342-347 (2016).
4. O. Li, J. He, K. Zeng, Z. Yu, X. Du, Y. Liang, G. Wang, Y. Chen, P. Zhu, W. Tong, D. Lister, and L. Ibbotson. Integrated Sensing and Communication in 6 G A Prototype of High Resolution THz Sensing on Portable Device. in Joint European Conference on Networks and Communications & 6 G Summit (EuCNC/6 G Summit) pp. 544–549 (2021).
5. H. Hamster, A. Sullivan, S. Gordon, W. White, R. W. Falcone. Subpicosecond, electromagnetic pulses from intense laser-plasma interaction. Physical Review Letters **71** 2725-2728 (1997).
6. T. Löffler, F. Jacob, and H. G. Roskos. Generation of Terhertz pulses by photoionization of electrically biased air. Appl. Phys. Lett. **77**, 453 (2000).
7. D. J. Cook and R. M. Hochstrasser. Intense terahertz pulses by four-wave rectification in air. Opt. Lett. **25**, 1210-1212, (2000).
8. K. Y. Kim, A. J. Taylor, J. H. Glownia, G. Rodriguez. Coherent control of terahertz supercontinuum generation in ultrafast laser–gas interactions. Nat. Photon. **2** 605-609 (2008).
9. A. D. Koulouklidis, C. Gollner, V. Shumakova, V. Y. Fedorov, A. Pugžlys, A. Baltuška, and S. Tzortzakis. Observation of extremely efficient terahertz generation from mid-infrared two-color laser filaments. Nat. Commun **11**, 292 (2020).
10. C. D'Amico, A. Houard, M. Franco, B. Prade, A. Mysyrowicz, A. Couairon, and V. T. Tikhonchuk. Conical Forward THz Emission from Femtosecond-Laser-Beam Filamentation in Air. Phys. Rev. Lett. **98**, 235002 (2007)
11. T. Takahashi, Y. Shibata, K. Ishi, M. Ikezawa, M. Oyamada and Y. Kondo. Observation of coherent Cerenkov radiation from a solid dielectric with short bunches of electrons. Phys. Rev. E **62**, 8606 (2000)
12. C. D'Amico, A. Houard, S. Akturk, Y. Liu, J. Le Bloas, M. Franco, B. Prade, A. Couairon, V.T. Tikhonchuk, and A. Mysyrowicz. Forward THz radiation emission by femtosecond filamentation in gases: theory and experiment. New Journal of Physics **10**, 013015 (2008).
13. D. H. Froula, D. Turnbull, A. S. Davies, T. J. Kessler, D. Haberberger, J. P. Palastro, S. W. Bahk, I. A. Begishev, R. Boni, S. Bucht, J. Katz and J. L. Shaw. Spatiotemporal control of laser intensity. Nat. Photon. **12**, 262–265 (2018).
14. K. Oubrerie, A. Leblanc, O. Kononenko, R. Lahaye, I. A. Andriyash, J. Gautier, J-P Goddet, L. Martelli, A. Tafzi, K. T. Phuoc, S. Smartsev and C. Thaury. Controlled acceleration of GeV electron beams in an all-optical plasma waveguide. Light. Sci. Appl **11**, 180 (2022).

15. H. E. Kondakci and A. F. Abouraddy. Diffraction-free space–time light sheets. Nat. Photon. **11** 733-740 (2017).
16. S. Steinke, J. V. Tilborg, C. Benedetti, C. G. R. Geddes, C. B. Schroeder, J. Daniels, K. K. Swanson, A. J. Gonsalves, K. Nakamura, N. H. Matlis, B. H. Shaw, E. Esarey and W. P. Leemans. Multistage coupling of independent laser-plasma accelerators. Nature **530** 190-193 (2016).
17. A. J. Howard, D. Turnbull, A. S. Davies, P. Franke, D. H. Froula, and J. P. Palastro, Photon Acceleration in a Flying Focus, Phys. Rev. Lett. **123**, 124801 (2019).
18. A. Kabacinski, E. Oliva, F. Tissandier, J. Gautier, M. Kozlová, J-P. Goddet, I. A. Andriyash, C. Thaury, P. Zeitoun and S. Sebban. Spatio-temporal couplings for controlling group velocity in longitudinally pumped seeded soft X-ray lasers. Nat. Photon. **17**, 354–359 (2023).
19. P. Walch, B. Mahieu, L. Arantchouk, Y.-B. André, A. Mysyrowicz, A. Houard. Impact of gravitational force on high repetition rate filamentation of femtosecond laser pulses in the atmosphere. Appl. Phys. Lett. **124**, 151101 (2024).
20. S. Fu, B. Mahieu, A. Mysyrowicz, A. Houard. Femtosecond filamentation of optical vortices for the generation of optical air waveguides. Optics Letters **47**, 5228 (2022).
21. A. Couairon, A. Mysyrowicz. Femtosecond filamentation in transparent media. Phys.Rep. **441**, 47 (2007).
22. A. Houard, Y. Liu, A. Mysyrowicz and B. Leriche. Calorimetric detection of conical THz radiation from femtosecond laser filaments in air. Appl. Phys. Lett. **91**, 241105 (2007).
23. Z.-M. Sheng, H.-C. Wu, K. Li, and J. Zhang. Terahertz radiation from the vacuum-plasma interface driven by ultrashort intense laser pulses. Phys. Rev. E **69**, 025401(R) (2004).
24. T. T. Simpson J. J. Pigeon, M. V. Ambat, K. G. Miller, D. Ramsey, K. Weichman, D. H. Froula, and J. P. Palastro. Spatiotemporal control of two-color terahertz generation, Phys. Rev. Research **6**, 013041 (2024).
25. A. Talbi, B. Zhou, P. U. Jepsen, S. Skupin, A. Courjaud and L. Bergé. Remote terahertz spectroscopy from extended two-color plasma filaments: The ALTESSE 2 project. EPL **143** 10001 (2023).
26. J. Zhao, W. Chu, L. Guo, Z. Wang, J. Yang, W. Liu, Y. Cheng and Z. Xu. Terahertz imaging with sub-wavelength resolution by femtosecond laser filament in air. Sci Rep **4**, 3880 (2014).
27. A. Houard, Y. Liu, B. Prade, V.T. Tikhonchuk and A. Mysyrowicz. Strong enhancement of Terahertz radiation from laser filaments in air by a static electric field. Phys. Rev. Lett. **100**, 255006 (2008).
28. S. I Mitryukovskiy, Y. Liu, B. Prade, A. Houard and A. Mysyrowicz. Coherent interaction between the THz radiation emitted by filaments in air. Laser Physics **24**, 094009 (2014).

General conclusion and outlook for future work

My thesis was dedicated to the development of optical methods to manipulate spatially and temporally the generation of femtosecond laser filaments in air, thereby optimizing various atmospheric applications.

I conducted detailed studies of the characteristics of filaments generated by Laguerre-Gaussian (LG) beams, including the critical power for self-focusing, the deposited energy, and the number and quality of filaments. We found that although filaments generated by LG beams have a lower plasma density and deposited energy compared to the ones produced by Gaussian or super-Gaussian beams, the energy deposition of LG beams is more uniform.

Using these results, I successfully demonstrated that the hydrodynamic effects caused by vortex filaments can be used to create optical air waveguides. Compared to the previous technique of generating air waveguides using four filaments, the use of vortex beams significantly improves the convenience and operability of the setup. Using a high repetition rate and high energy laser I successfully utilized the hydrodynamic cumulative effect of filaments to produce a decametric permanent air waveguide using a collimated Laguerre-Gaussian beam. I also observed that if a focused Gaussian beam is used to create the kHz low-density channel, a permanent Axicon-like structure can be formed in air, resulting in the formation of a quasi-Bessel beam. taking advantage of the ability of LG beam filaments to generate longer and more uniform energy deposition, we demonstrated that such filaments can guide discharges over longer distances than gaussian beams. This technique can extend the guiding range of laser filaments for applications such as lightning control and other remote atmospheric experiments involving filaments.

Additionally, to overcome the limitation of the Rayleigh length for the generation of focused superfilaments, we demonstrated a new scheme, where the focusing of a TW laser beam is dispersed in the air using a multi-focal phase plate. Compared to regular Gaussian beams, optimized superfilaments exhibit higher energy deposition, with a plasma length extended by at least a factor 2. These extended superfilaments are also able to guide electric discharges over a much longer distance. Combined with vortex beams, the multi-focal phase plate can also double the length of the air waveguide. We believe this technology has the potential to be useful in many atmospheric applications of filaments sensitive to the filament plasma length, such as lightning control, optical communication through fog and cloud layers, satellite communication, and optical or terahertz waveguides in air.

Finally, we used a technique called "flying focus" to produce a plasma string in air, whose ionization front velocity and direction can be tunable. We show that this controllable plasma wave can generate directionally adjustable terahertz radiation. In addition, we found that with superluminal ionization velocities $v > c$, the radiated THz energy can be increased by an order of magnitude with respect to the transition-Cherenkov radiation obtained with $v = c$, and all frequencies are emitted in a narrow cone at a large angle.

The technological advancements we have achieved are expected to lead to some interesting industrial and research applications in the future. For example, laser filaments generated by vortex beams naturally form hollow plasma structures, which might be used to guide terahertz or microwave beams. Additionally, the air waveguide and "quasi-Axicon" suggest that the hydrodynamics effects created by the filaments, especially those generated by high repetition rate lasers, could potentially be used to manipulate laser beams through the formation of diffractive, dispersive, or focusing elements made of gas. To extend the length of guided discharges, the use of LG beam and multifocus phase plate method are expected to optimize laser-guided lightning control. The extended filament length also seems promising to improve many atmospheric applications. The backward terahertz could be employed in combination with a static electric field to enhance the THz yield, together with a coherent combination of organized multiple filaments.

List of publications and of attended conferences

Personal publications in peer-reviewed journals

[1]. S. Fu, B. Groussin, Y. Liu, A. Mysyrowicz, V. Tikhonchuk, A. Houard, Steering laser-produced THz radiation in air with superluminal ionization fronts, Phys. Rev. Lett. (Accepted).

[2]. S. Fu, A. Mysyrowicz, L. Arantchouk, M. Lozano, A. Houard, Extending femtosecond laser superfilamentation in air with a multifocal phase mask, Appl. Phys. Lett. **125** (1) (2024).

[3]. S. Fu, L. Arantchouk, M. Lozano, A. Mysyrowics, A. Couairon, A. Houard, Laguerre Gaussian laser filamentation for the control of electric discharges in air, Opt. Lett. **49** (13), 3540-3543 (2024).

[4]. S. Fu, B. Mahieu, A. Mysyrowics, A. Houard, Femtosecond filamentation of optical vortices for the generation of optical air waveguides, Opt. Lett. **47**, (19), 5228-5231 (2022).

Attended peer-reviewed international conferences

[1]. S. Fu, B. Mahieu, A. Mysyrowics, A. Houard, Filamentation of Vortex beam in air for the generation of tubular plasma, International Conference on Laser Filamentation (COFIL 2022), July 2022, Crete. Poster.

[2]. S. Fu, B. Mahieu, A. Mysyrowics, A. Houard, Optical waveguide generated in air though femtosecond filamentation of optical vortices, Conference on Lasers and Electro-Optics (CLEO 2023), May 2023, San Jose. Oral contribution.

[3]. S. Fu, B. Mahieu, A. Mysyrowics, A. Houard, Femtosecond filaments and air waveguides generated by TW vortex beam, Conference on Lasers and Electro-Optics (CLEO Europe 2023), June 2023, Munich. Poster.

[4]. S. Fu, A. Mysyrowicz, L. Arantchouk, M. Lozano, A. Houard, Extending femtosecond laser superfilamentation in air with a phase mask, Conference on Lasers and Electro-Optics Pacific Rim (CLEO PR 2024), August 2024, Incheon. Oral contribution.

[5]. S. Fu, A. Mysyrowicz, L. Arantchouk, M. Lozano, A. Houard, Laguerre Gaussian laser filamentation for the control of electric discharges in air, Conference on Lasers and Electro-Optics Pacific Rim (CLEO PR 2024), August 2024, Incheon. Oral contribution.

[6]. S. Fu, B. Mahieu, M. Lozano, L. Bizet, F. Alahyane, A. Mysyrowicz, A. Houard, 20 m-long permanent air waveguide produced by filamentation of a collimated Laguerre-Gauss beam at 1030 nm, Conference on Lasers and Electro-Optics Pacific Rim (CLEO PR 2024), August 2024, Incheon. Oral contribution.

[7]. S. Fu, B. Groussin, Y. Liu, A. Mysyrowicz, V. Tikhonchuk, A. Houard, Steering laser-produced THz radiation in air with superluminal ionization fronts, International Conference on Laser Filamentation (COFIL 2024), August 2024, Tianjin. Oral contribution.

[8]. S. Fu, A. Mysyrowicz, L. Arantchouk, M. Lozano, A. Houard, Extending femtosecond laser superfilamentation for guided discharge and air waveguide, International Conference on Laser Filamentation (COFIL 2024), August 2024, Tianjin. Poster.

[9]. S. Fu, B. Mahieu, M. Lozano, L. Bizet, F. Alahyane, A. Mysyrowicz, A. Houard, 20 m-long permanent air waveguide produced by filamentation of a collimated Laguerre-Gauss beam at 1030 nm, International Conference on Laser Filamentation (COFIL 2024), August 2024, Tianjin. Poster.

[10]. S. Fu, A. Mysyrowicz, L. Arantchouk, M. Lozano, A. Houard, Generation and applications of Laguerre Gaussian laser filamentation, International Conference on Laser Filamentation (COFIL 2024), August 2024, Tianjin. Poster.

[11]. S. Fu, B. Mahieu, M. Lozano, L. Bizet, F. Alahyane, A. Mysyrowicz, A. Houard, 20 m-long permanent air waveguide produced by filamentation of a kHz collimated Laguerre-Gauss beam, International Symposium on Laser Interaction with Matter (LIMIS 2024), November 2024, Shenzhen. Oral contribution.

ECOLE DOCTORALE

Titre : Optimisation de filaments laser femtoseconde dans l'atmosphère

Mots clés : Filamentation, plasma, THz.

Résumé : Ce travail de thèse porte sur la mise en forme spatiale et temporelle de filaments femtoseconde dans l'air, et sur leur optimisation pour des applications atmosphériques.
Après avoir introduit le phénomène de filamentation laser et ses applications, nous présentons une étude de la génération de filaments laser avec des modes de Laguerre-Gauss. Le chapitre suivant montre que ces modes permettent d'organiser des faisceaux de filaments en anneau et de produire ainsi des guides d'ondes optiques dans l'air. Nous démontrons ensuite que combiner les faisceaux de Laguerre-Gauss avec des lames de phase multifocales permet de prolonger la longueur du guide d'ondes atmosphérique. Enfin, en utilisant l'effet de chauffage cumulatif créé par des filaments à haute cadence, nous démontrons la génération de guides d'ondes permanents de plusieurs dizaines de mètres de long.
Dans le chapitre suivant, nous discutons de l'organisation de filaments le long de l'axe de propagation du faisceau. Ainsi, utiliser des faisceaux Laguerre-Gauss prolonge la longueur du filament par rapport à un faisceau gaussien et permet d'augmenter la longueur des décharge électriques guidées par laser. En utilisant des lames de phase multifocales, nous générons également des superfilaments étendus, doublant la distance de décharge guidée.
Enfin, dans la cinquième partie, nous discutons de la génération de filaments de plasma à l'aide d'une technique de « flying focus », permettant de contrôler la vitesse et la direction du front d'ionisation. Un front superluminal permet ainsi la génération d'un rayonnement térahertz de type Cherenkov, augmentant ainsi d'un ordre de grandeur le rayonnement térahertz produit par des filaments de lumière monochromatique dans l'air.

Title: Tailoring femtosecond laser filamentation in the atmosphere

Keywords: Filamentation, plasma, THz.

Abstract: This thesis deals with the spatio-temporal tailoring of femtosecond laser filaments in air, and their optimization for atmospheric applications. We present a detailed study on the generation of filaments with Laguerre-Gaussian beams, including measurements of the critical power for self-focusing and of the deposited energy in filaments under different conditions. Then we discuss the organization of filaments along the transverse section of the beam, using vortex and other Laguerre-Gaussian beams for the realization of optical air waveguides. We first demonstrate that vortex beams are a simple method to create air waveguides. Then, by combining vortex beams with multifocal phase plates, we significantly extend the length of these air waveguides. Finally, utilizing the cumulative effect produced by the filaments at a kHz repetition rate, we generate a permanent air waveguide up to several tens of meters long.
For guiding discharge in air, we discuss the organization and extension of filaments along the propagation axis of the beam. Using Laguerre-Gaussian beams, we significantly extend the filament length and successfully increase the length of guided discharge compared to a classical gaussian beam. Additionally, by using multifocal phase plates to generates three foci along the laser axis, we produce extended superfilaments, doubling the length of laser guided discharges.
Finally, we discuss the generation of spatio-temporally controlled light filaments, using a flying focus technique. We demonstrate the formation of an ionization front with adjustable speed and direction. The later can generate a pure Cherenkov terahertz radiation when the ionization front velocity is superluminal, thus increasing by one order of magnitude the terahertz radiation produced by monochromatic light filaments in air.

Institut Polytechnique de Paris
91120 Palaiseau, France